Thermal Properties and Nanoelectromechanical System Based on Carbon Nanotubes

Thesis by
Hsin-Ying Chiu

In Partial Fulfillment of the Requirements for the
Degree of
Doctor of Philosophy

California Institute of Technology
Pasadena, California
2009
(Defended February 17, 2009)

Acknowledgments

I would like to express my gratitude to my thesis advisor, Professor Marc Bockrath, whose expertise, understanding, and patience added considerably to my Ph.D. study at Caltech. Marc not only has taught me valuable skills for doing research but has also influenced me with invaluable attitudes to become a scholar. His advices have been inspiring and motivating, and his words of encouragement have always been a strong support especially in difficult moments. During my graduate years, he provided me with direction, technical support, and became more of a mentor and a friend than an advisor. I feel truly grateful and fortunate to be one of his students.

I would also like to thank the members of my defense and candidacy examining committees for their interest: Professor Nai-Chang Yeh, Professor Keith Schwab, Professor Gil Refael, Professor Kerry Vahala, and Prof James Eisenstein. I would also like to thank Professor Sandra Troian and Professor Chin-Lin Guo at Caltech, Professor Jeanie Lau at UC Riverside, and Professor Chung-Yu Mou at Taiwan who provided me helpful guidance along my graduate study at Caltech.

I recognized that this research would not have been possible without the technical assistance from Ali Ghaffari, Guy DeRose, Bophan Chhim and Michael Gerfen. I would also like to thank our administrative assistant, Rosalie Rowe, who takes cares of our lab very well.

I would like to thank my labmates, Hareem Maune, Peter Hung, Jinseong Heo, Brian Standley, Henk Postma, Joyce Wang, Bertrand Bourlon, Sinchul Yeom, Keisuke Shimizu and Anthony Mendez, for their friendship and for sharing their experiences and research during my stay in the Nanoscale Lab.

I especially thank Hareem Maune and Cameron Hughes with whom I shared most of my happiness and sadness, and to whom I am grateful for constant thoughtful support. Appreciation also goes out to those who provided me with experimental advice at times of critical need; Philip Feng, Jiansong Guo and Yan Chen. I would also like to thank my

friends, particularly Hsiang-Ku Lin, Wei Peng, Deqi Wang, James Wu, Yi-Huei Chiang, Wenzhong Bao, Ching-Tzu Chen, Hui-Chun Chien, Fang Li, Slobodan Mitrovic, Mortada Mehyar, Wei-Ting Chen, Eh Tan. Especially, thanks to my roommates and good friends, Fu-Ling Yang, Min Tao and Jie Yang, for exchanging knowledge, skills, and even frustration during my graduate program which helped enrich the experience. Thank also goes out to the friends I made in my last year at Caltech, Carson Chen, Yuan-Chuan Lien, Icy Ma, Amy Chang, May Lin, Tiffany Chang, Tsui-Fen Chou, Yi-Chun Chen, Yu-Nung Lin and Yu Wang. They gave me a lot support to finish my last step of graduate study and provided me with many good memories.

Finally, I would like to thank my family for their everlasting support and care through my entire life. In particular, I must acknowledge my best friend, Shih-Jung Huang, as without her love, encouragement, and editing assistance I would not have finished this thesis. My endless thanks to their unconditional love!

Abstract

In Chapter I, the fundamental electronic properties of two-dimensional (2D) graphene and one-dimensional (1D) carbon nanotubes are discussed, along with the carbon nanotube single-electron transistors (SETs). In addition to nanotubes' extraordinary electronic properties, the phenomena of phonon transport in carbon nanotubes are also notable. In Chapter II, we discuss our experiments probing the thermal properties of multi-walled carbon nanotubes. We exploit the specific breakdown temperature under a large current, which provides an effective thermometer, in conjunction with the known power input to measure the thermal conductivity of the nanotubes. Our results reveal the exceptional micron-scale phonon mean free path at temperatures approaching 900K, and we demonstrate the first evidence for ballistic phonon propagation in nanotubes, reaching a regime where the thermal conductance of nanotubes is limited only by fundamental quantum mechanical limits imposed by their 1D nature.

Moreover, the combination of remarkable electrical and mechanical properties makes carbon nanotubes a highly promising candidate for nanoelectromechanical systems (NEMS). In Chapter III, we investigate using doubly clamped suspended single-walled carbon nanotubes as nanomechanical resonators at cryogenic temperatures. Their intrinsic single-electron transistor behavior provides a mixing mechanism to self-detect their motion based on their capacitance to a nearby gate electrode. We exploit our devices to attain an ultrasensitive mass sensor, realizing atomic-scale mass sensing. Finally, in Chapter IV, nanoelectromechanical switches based on using multi-walled carbon nanotubes as nanoscale linear bearings are discussed. First we demonstrate the preparation of the initial OFF state by using electrical breakdown to create gaps in a free-standing MWNT device, while subsequently the ON state is actuated with electrical forces and undergoes linear bearing motion that telescopes the inner shells to bridge the gaps. The switching cycle can be performed in double-walled nanotube devices by restoring the insulating OFF state with a controllable gate voltage. These tubular switches can potentially serve as nonvolatile memory or logic gate elements.

TABLE OF CONTENTS

LIST OF FIGURES

Chapter I

Chapter II

Chapter III

Chapter IV

LIST OF TABLES

Chapter I

Introduction to Carbon Nanotubes

Single-walled carbon nanotubes (SWNTs) are one-dimensional conductors, acting as quantum wires [1]; the intrinsic conductance of high-quality samples has been observed to be close to the quantum conductance $4e^2/h$. The remarkable electrical properties of carbon nanotubes are directly inherited from graphene, an unusual planar semimetal; its charge carriers propagate in the reduced dimension with effectively zero mass and constant velocity. Nearly defect-free nanotubes are perfect candidates to study electronic systems in one dimension, where the strong electron-electron interactions lead to Luttinger liquid behavior [2], and the formation of a 1D Wigner crystal phenomena emerges in a dilute electron system [3]. Furthermore, a recent study shows the electrons in nominally metallic nanotubes comprise a 1D Mott insulator, indicating that carbon nanotubes are never truly metallic. Therefore, in this chapter, a review of the fundamental electrical properties of SWNTs will be discussed, from graphene structure and energy dispersion relations to carbon nanotubes. In additional, carbon nanotube single-electron transistor phenomena will be introduced, which is background material for Chapter III.

I-1 Structure of Graphene

Graphene is a single layer of graphite which is an array of carbon atoms arranged in a honeycomb lattice, as shown in Figure I-1 (a). The blue-dashed rhombus, constructed by the primitive vectors $\vec{a}_1$ and $\vec{a}_2$, is the unit cell of graphene enclosing two atoms, indicated by red and blue colors. The gray-shaded hexagon can be viewed as the Wigner-Seitz cell of extended rhombus lattice, which through translation can readily be seen to enclose two atoms per unit cell. Here, the real-space primitive vectors $\vec{a}_1$ and $\vec{a}_2$ are

$$\vec{a}_1 = \left(\frac{\sqrt{3}}{2} a, \frac{1}{2} a \right), \quad \vec{a}_2 = \left(\frac{\sqrt{3}}{2} a, -\frac{1}{2} a \right)$$

and have the lengths of the lattice spacing $a = |\vec{a}_1| = |\vec{a}_1| = a_{C-C} \times \sqrt{3} = 2.46$ Å, where a_{C-C} is the nearest-neighbor C–C distance. Correspondingly, the reciprocal lattice of graphene is shown in Figure I-1(b). The dashed rhombus is the primitive unit cell defined by the reciprocal lattice vectors $\vec{b}_1$ and $\vec{b}_2$, which are expressed by

$$\vec{b}_1 = \left(\frac{2\pi}{\sqrt{3}a}, \frac{2\pi}{a}\right), \quad \vec{b}_2 = \left(\frac{2\pi}{\sqrt{3}a}, -\frac{2\pi}{a}\right).$$

There two lattice vectors that correspond to a lattice constant $4\pi/\sqrt{3}\,a$ in reciprocal space and satisfy the standard definition $\vec{a}_i \cdot \vec{b}_j = 2\pi\delta_{ij}$ in 2D system, where δ_{ij} is the Kroneker delta.

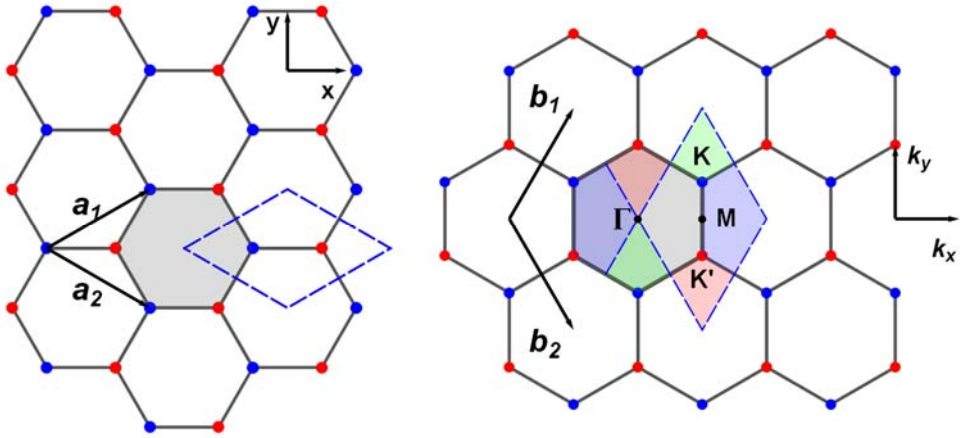

Figure I-1. Graphene lattice. (a) Real space of graphene lattice. (b) Graphene reciprocal lattice. High symmetry points, Γ, K, and M are all shown in the figure.

The shaded hexagon shown in Figure I-1(b) is Brillouin zone of graphene, which is depicted in several shades of color (red, green and blue) to identify zones related by reciprocal lattice vectors to corresponding zones of the primitive unit cell. There are two of the high-symmetry inequivalent K points (under translational symmetry) at the corners of the hexagonal Brillouin zone labeled as K and K', and these, as well as equivalent points in the lattice, are shown as blue and red dots, respectively.

I-2 Dispersion Relation of Graphene Structure

The electronic properties of single-walled carbon nanotubes, at first order, can be deduced from that of graphene by mapping the band structure of 2D hexagonal lattice onto a cylinder. Thus, before we start discussing the nanotube electronic band structure, it is appropriate to consider the energy dispersion relation of graphene first.

In graphene's hexagonal structure, each carbon atom has three nearest neighbors and four valence electrons. Three of these valence electrons (i.e., $2s$, $2p_x$ and $2p_y$) are hybridized to form the sp^2 σ bonds with adjacent carbon atoms constructing the skeleton of the local structure; while the fourth electron (i.e., $2p_z$) contributes to the π band, which is orientated perpendicular to the plane of the sheet with each carbon atom contributing one spin-degenerate orbital centered on that atom. Because the nodal plane of these π orbitals is coincident with the plane of the graphene sheet, the π bonds of graphene are separated by symmetry from the σ bonds, which leads to two distinguishing π electrons in the valence band and π^* electrons in the conducting band. Only the π electrons near the Fermi level contribute to the electronic properties of graphene.

Figure I-2 shows the energy dispersion relation of graphene, which is calculated according to a tight-bonding model. The diagram shows 3 pairs of σ and σ^* bands, and one pair of π and π^* bands.

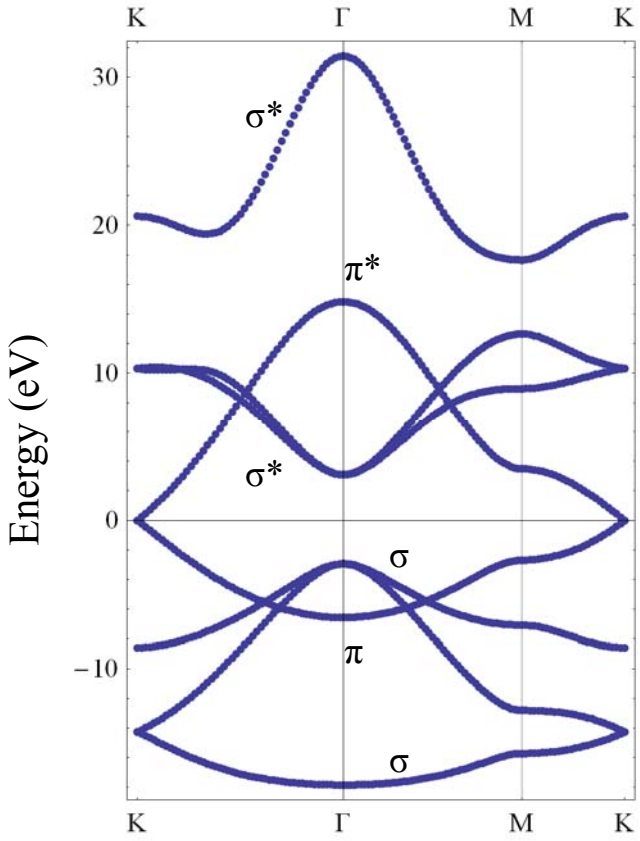

Figure I-2. The energy dispersion relations for σ and π bands of graphene, simulated based on the tight binding method with parameters from ref. [4].

H	Value (eV)	**S**	Value
$\mathbf{H_{ss}}$	-6.769	$\mathbf{S_{ss}}$	0.212
$\mathbf{H_{sp}}$	-5.580	$\mathbf{S_{sp}}$	0.102
$\mathbf{H_{\sigma}}$	-5.037	$\mathbf{S_{\sigma}}$	0.146
$\mathbf{H_{\pi}} \equiv t$	-3.033	$\mathbf{S_{\pi}} = s$	0.129
$\mathbf{E_{2s}}$	-8.868		

Table I-1. The coupling parameters of carbon atoms in the Hamiltonian for π and σ bands in 2D graphene from ref. [4]. Note that the value for ε_{2s} is given relative to $\varepsilon_{2p} = 0$.

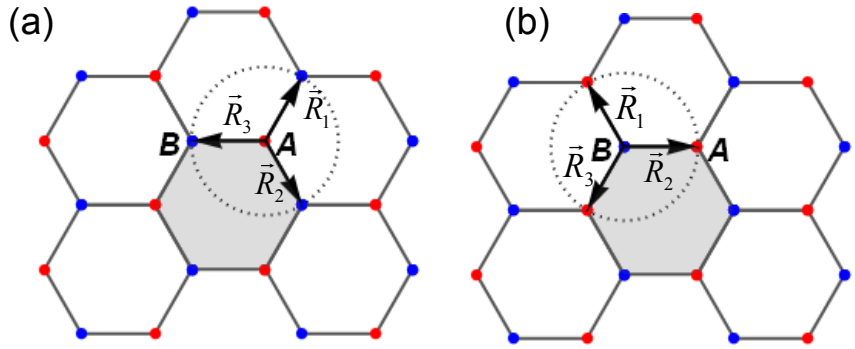

Figure I-3. Graphene lattice with two-atom basis in real space. (a) Three nearest-neighbor B atoms relative to an A atom denoted by the vectors $\vec{R}_1, \vec{R}_2$, and $\vec{R}_3$. (b) Three nearest-neighbor A atoms relative to a B atom denoted by the vectors $\vec{R}_1, \vec{R}_2$, and $\vec{R}_3$

Hence, we only need to consider the π bands, which can be simply analyzed by a tight binding method. Since every unit cell of the graphene has two inequivalent carbon atoms as a basis, there is a 2×2 linear equation to solve. We can write down the Hamiltonian element H_{AB} according to the geometry shown in Figure I-3 (a) and consider the only nearest-neighbor interactions.

$$\begin{aligned} H_{AB} &= t(e^{i\vec{k}\cdot\vec{R}_1} + e^{i\vec{k}\cdot\vec{R}_2} + e^{i\vec{k}\cdot\vec{R}_3}) \\ &= t\, f(k) \end{aligned}$$

where $f(k)$ is a function the sum of the phase factors of $e^{i\vec{k}\cdot\vec{R}_i}$ and

$$f(k) = e^{ik_x a/\sqrt{3}} + 2e^{-ik_x a/2\sqrt{3}} \cos\left(k_y a/2\right).$$

$f(k)$ is a complex function, and $H_{AB} = H_{BA}^{*}$.

Solving the secular equation $\det(\mathbf{H} - E\mathbf{S}) = 0$

$$E_{g,2D}^{\pm} = \frac{\varepsilon_{2p} \pm t\omega(\vec{k})}{1 \pm s\omega(\vec{k})}, \begin{cases} +\,sign, & \pi \\ -\,sign, & \pi^{*} \end{cases} \qquad \text{(I-1)}$$

where ε_{2p} is the electron site energy, t is the transfer integral with the nearest neighbor defined as $t = \langle \varphi_A(r-R) | H | \varphi_B(r-R \pm a/2) \rangle$, and the s is the tight binding overlap integral. When $t > 0$, E^+ and E^- are corresponding to the bonding π and π^* energy bands, respectively. The function $\omega(\vec{k})$ is given by

$$\omega(\vec{k}) = \sqrt{|f(\vec{k})^2|}$$
$$= \sqrt{1 + 4\cos\left(\frac{\sqrt{3}k_x a}{2}\right)\cos\left(\frac{\sqrt{3}k_y a}{2}\right) + 4\cos^2\left(\frac{k_x a}{2}\right)}.$$

Figure I-4 is the 3D plot of the energy dispersion relation of graphene with a hexagonal Brillouin zone of six gapless Dirac points, which corresponds to two inequivalent K points.

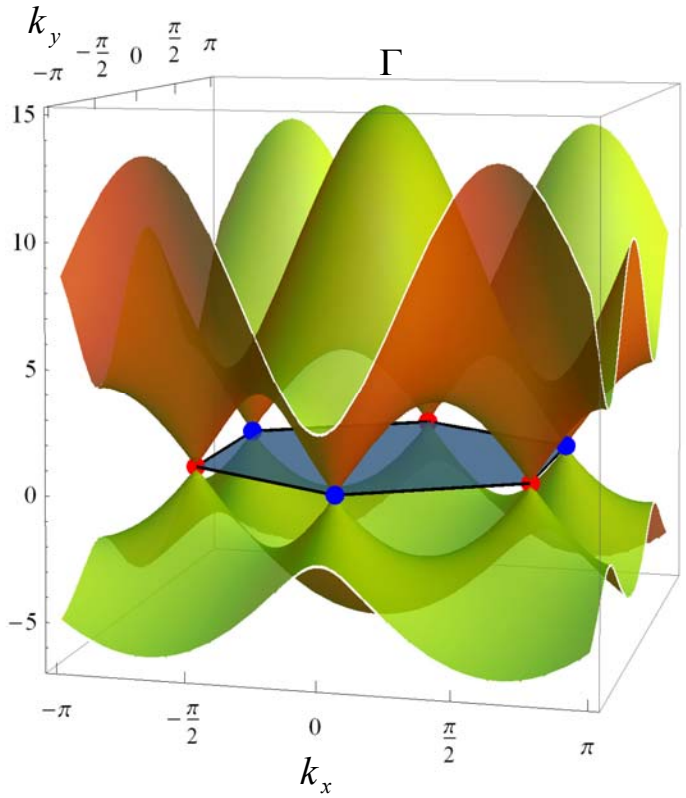

Figure I-4. The energy dispersion relations of graphene with the hexagonal Brillouin zone. The blue and red circles indicate the high-symmetry points K and K', respectively. The parameters $\varepsilon_{2p} = 0$, t = -3.033 eV, and s = 0.129.

I-2-1 Low-Energy Approximation

Furthermore, because there is only one electron per spin degenerate orbital, the Fermi level for a neutral graphene sheet is at the K points. For energies near the Fermi energy, the dispersion near the six K points can be linearized, yielding a dispersion corresponding to relativistic massless Dirac Fermions. After Taylor expansion in terms of $\Delta k = \left|\vec{k} - \vec{k}_F\right|$, we get

$$\begin{aligned} E^{\pm}_{k_F} &= \varepsilon_F \pm \frac{\sqrt{3}}{2} ta \left|\vec{k} - \vec{k}_F\right| \\ &= \varepsilon_F \mp \hbar v_F \left|\vec{k} - \vec{k}_F\right| \quad . \end{aligned} \tag{I-2}$$

The energy dispersion relation $E^{\pm}_{g,2D}(\vec{k})$ given by eq. (I-1) and the Fermi velocity is $v_F = \frac{\sqrt{3}}{2\hbar} ta$; using known values for *t* and *a*, we obtain $v_F \approx 8.7\times10^5$ m/s.

I-3 Structure of Single-Walled Carbon Nanotubes

A single-wall carbon nanotube (SWNT) can be visualized by rolling up a graphene sheet along the chiral vector $\vec{C}_h = n\,\vec{a}_1 + m\,\vec{a}_2$ to construct a (n, m) nanotube with diameter $d_t = \left|\vec{C}_h\right| / \pi$. In Figure I-1, the shaded quadrilateral area $OBB'A$ is the unit cell of a $(4, 2)$ nanotube in terms of the primitive cell of the graphene hexagonal lattice.

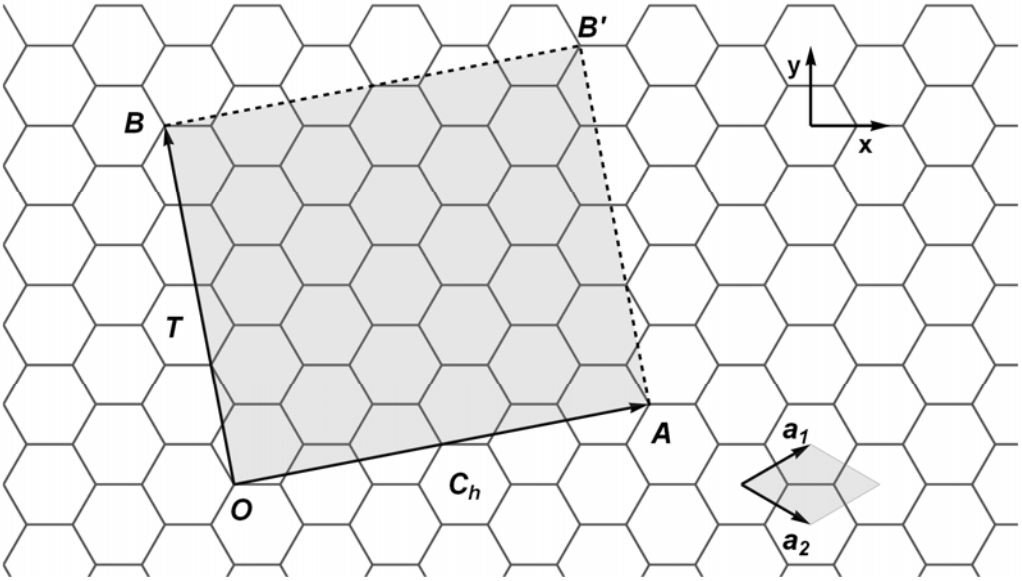

Figure I-5. Making a nanotube and its structure. The background is graphene hexagonal lattice defined by the primitive lattice vectors $\vec{a}_1$ and $\vec{a}_2$ in real space. A gray-shaded rhombus is the primitive cell of graphene with a basis of two carbon atoms. The gray-shaded quadrilateral $OAB'B$ is the unrolled hexagonal lattice of a nanotube unit cell. $\overrightarrow{OA}$ and $\overrightarrow{OB}$ define the chiral vector $\vec{C}_h$ and the translational vector $\vec{T}$, respectively. The figure corresponds to $\vec{C}_h = (4, 2)$, $\vec{T} = (4, -5)$, $N = 28$ and the $d = d_R = 2$.

The electronic properties of single-walled carbon nanotubes can be specified by one single parameter, the chiral vector. Therefore, there are three categories of nanotubes: an armchair nanotube corresponds to the case of $n = m$, that is $\vec{C}_h = (n, n)$, which represents metallic nanotube, a 1D quantum conductor; a zigzag nanotube corresponds to the case of $m = 0$ or $\vec{C}_h = (n, 0)$, which is generally semiconducting and only metal when n is an integer multiple of three; all other (n, m) chiral vectors correspond to chiral nanotubes. However, if the curvature effect [5] is considered, in the chiral case when $n - m$ is a multiple of 3 then the nanotube is semiconducting with a very small band gap; these nanotubes were supposed to be metallic, but the gap is open due to the curvature — in other words, this is caused by the hybridization of sp^3 and sp^2 orbitals [6].

More recent results [7] show that carbon nanotubes are never metallic due to the Mott insulating state, which is a manifestation of strong electron interactions in nominally metallic systems, and this gap has a magnitude of ~ 10 to 100 milli-electron volts and a nanotube radius (r) dependence of ~1/r.

Although there are many intrinsic and extrinsic factors that can alter the nanotube electronic band structures from the first-order approximation, it still gives us a general idea of carbon nanotube electronic properties based on the graphene honeycomb structure. In the later section, one armchair nanotube with $\vec{C}_h = (5,5)$, one zigzag nanotube with $\vec{C}_h = (8,0)$, and a chiral nanotube with $\vec{C}_h = (4,2)$ will be discussed in detail.

After a chiral vector is chosen, the translational vector $\vec{T}$ is also defined to be perpendicular to the chiral vector and parallel to the nanotube axis. The translational vector $\vec{T}$ in Figure I-4 is represented by $\overrightarrow{OB}$, which corresponds to the first lattice point of the 2D graphene sheet. It can be written as $\vec{T} = t_1\,\vec{a}_1 + t_2\,\vec{a}_2 = (t_1, t_2)$, where the coefficient t_1 and t_2 are $t_1 = (2m+n)/d_R$ and $t_2 = -(2n+m)/d_R$ and d_R is the greatest common divisor of $2m+n$ and $2n+m$. In other words, t_1 and t_2 have no common divisor except unity.

The magnitude of the translation vector is $\left|\vec{T}\right| = \sqrt{3}L/d_R$. Therefore, the number of hexagons, N, contained within the 1D unit cell of a nanotube is determined by the division of nanotube unit cell area by graphene unit cell area

$$N = \frac{\left|\vec{C}_h \times \vec{T}\right|}{\left|\vec{a}_1 \times \vec{a}_2\right|} = \frac{2(m^2 + n^2 + nm)}{d_R}.$$

For the (4, 2) nanotube in Figure I-5, we obtain $\vec{T} = (4, -5)$ and N = 28, so that the unit cell of the (4, 2) nanotube encloses 28 hexagons, or 2 × 28 = 56 carbon atoms. Every

atom in a nanotube unit cell can contribute one electron, which would generate N pairs of bonding π and anti-bonding π^* electronic energy bands.

I-4 Electrical Properties of Carbon Nanotubes

Applying the following definition in 2D system enables us to construct the reciprocal lattice vectors of a nanotube with the chiral vector $\vec{C}_h$ and translational vector $\vec{T}$:

$$\begin{aligned} \vec{C}_h \cdot \vec{K}_1 &= 2\pi, \qquad \vec{T} \cdot \vec{K}_1 = 0 \\ \vec{C}_h \cdot \vec{K}_2 &= 0, \qquad \vec{T} \cdot \vec{K}_2 = 2\pi \end{aligned} \quad . \tag{I-3}$$

As a result of the spatial confinement of the nanotube in the circumferential direction, the vector $\vec{C}_h$ does not act as a translation vector, but as a generator of pure rotations. In this sense, the relation $\vec{C}_h \cdot \vec{K}_1 = 2\pi$ can only be satisfied for $\vec{K}_1$ being integer multiples of $2/d_t$, where d_t is the diameter of the nanotube. In other words, the electron wavefunctions have to be the same when $\vec{r}$ goes around the circumference, thus the factor $e^{-\vec{C}_h \cdot \vec{K}_1} = 1 = e^{i(2\pi)n}$, where n is the integer. After some straightforward algebraic manipulations to equation (I.3), we obtain

$$K_1 = \frac{1}{N}(-t_2\vec{b}_1 + t_1\vec{b}_2), \quad K_2 = \frac{1}{N}(m\vec{b}_1 - n\vec{b}_2).$$

The reciprocal lattice vector $\vec{K}_2$ is along the nanotube axis and $\vec{K}_1$ gives discrete k values in the circumference direction. The first Brillouin of this 1D structure is the line segment passing through the Γ point shown in Figure I-6.

Because the nanotube unit cell is much larger than graphene hexagonal unit cell, the reciprocal lattice vectors $\vec{K}_1$ and $\vec{K}_2$ are much smaller. Thus in the later section we adopt the zone boundary folding method to map out the whole nanotube Brillouin zone. Thus, the Brillouin zone folding model is applied to obtain the electronic band structure of SWNT.

$$E_{\mu}(k) = E_{g2D}\left(k\frac{\vec{K}_2}{\left|\vec{K}_2\right|} + \mu\vec{K}_1 \right),\ (\mu = 0, \cdots, N-1, \text{and} -\frac{\pi}{\left|\vec{T}\right|} < k < \frac{\pi}{\left|\vec{T}\right|})$$

Where T is the length of the translation vector $\vec{T}$ and μ is defined by the number of hexagonal unit cells in the carbon nanotube unit cell.

The following is a simple geometry calculation, which can assist in determining whether, for a given chiral vector, the nanotube is metallic or a small band gap semiconducting nanotube in the first-order approximation.

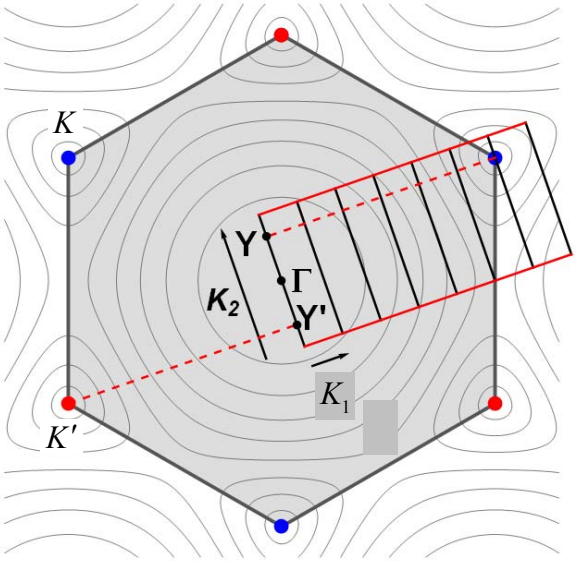

Figure I-6. The condition for metallic energy bands. Graphene hexagonal Brillouin with nanotube line segments Brillouin

From the previous discussion, if there is any nanotube Brillouin zone cutting through either K or K' points, then nanotube would show the metallic behavior. In other words, the distance $\overline{YK}$ or $\overline{Y'K'}$ in Figure I-6 are multiples of the length of $\vec{K}_1$, where $\overline{YK}$ or $\overline{Y'K'}$ are perpendicular to the reciprocal lattice vectors $\vec{K}_2$ and parallel to $\vec{K}_1$. In Figure I-6, the parallel line segments are allowed vectors (1D Brillouin zone), which are quantized along the direction $\vec{K}_1$ and equally spaced by $\left|\vec{K}_1\right|$. In addition, $Y(Y')$ point is drawn by

perpendicularly intersecting the $\vec{K}_2$ vector (through Γ point) from $K(K')$ point. Then, $\overrightarrow{YK}$ vector is given by

$$\overrightarrow{YK} = \frac{\left(\overrightarrow{\Gamma K} \cdot \vec{K}_1\right)}{\left|\vec{K}_1\right|^2} \vec{K}_1$$

where $\overrightarrow{\Gamma K} = \overrightarrow{\Gamma M} + \overrightarrow{MK} = \frac{\vec{b}_1 + \vec{b}_2}{2} + \frac{\vec{b}_1 - \vec{b}_2}{6} = \frac{2}{3}\vec{b}_1 + \frac{1}{3}\vec{b}_2$. Calculating the vector product and simplifying the expression, we get

$$\overrightarrow{YK} = \frac{2n+m}{3} \vec{K}_1.$$

Similarly,

$$\overrightarrow{Y'K'} = -\frac{2n+m}{3} \vec{K}_1.$$

Therefore, the condition for metallic nanotubes is that (*2n*+*m*) or (*n*–*m*) is a multiple of 3. Armchair nanotubes denoted by (n, n) are always metallic, and the zigzag nanotubes (*n*, *0*) are only metallic when *n* is a multiple of 3. For any other chiral nanotubes satisfying the above condition, they would show small band gap semiconducting behavior. Again, we emphasize that the most recent study shows that carbon nanotubes are never metallic due to the formation of a Mott insulating state [7].

In the following, three different types of nanotube are introduced, a chiral semiconducting nanotube with $C_h = (4, 2)$, an armchair metallic with $C_h = (5, 5)$ and a zigzag semiconducting nanotube with $C_h = (8, 0)$.

- A chiral semiconducting nanotube with the chiral vector $(n, m) = (4, 2)$

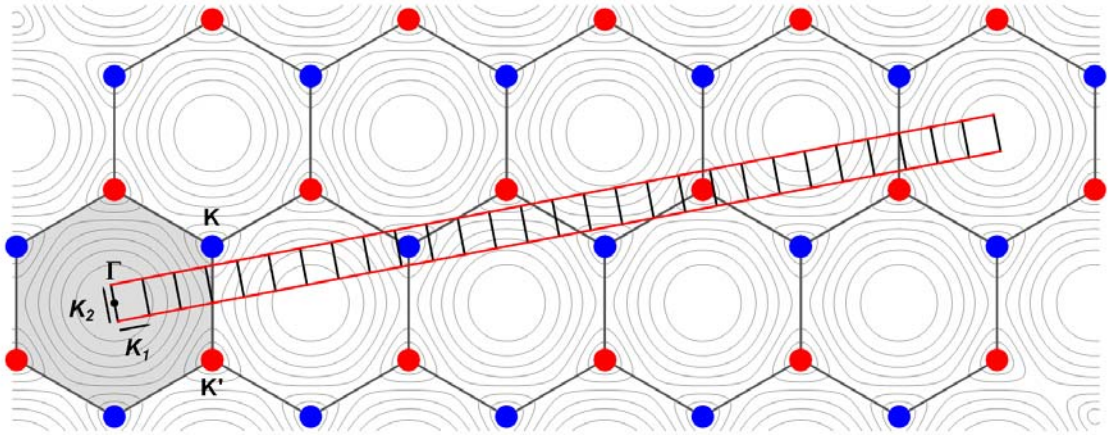

Figure I-7. A chiral semiconducting nanotube with the chiral vector $(n, m) = (4, 2)$. The Brillouin zone of a carbon nanotube is represented by the segment line which passes through the highest symmetry point Γ. The vectors $\vec{K}_1$ and $\vec{K}_2$ are reciprocal lattice vectors corresponding to C_h and T, respectively. $C_h = (4, 2)$, $T = (4, -5)$, $K_1 = (5b_1 + 4b_2) / 28$, $K_2 = (2b_1 - 4 b_2) / 28$ and $N = 28$.

- An armchair metallic carbon nanotube with the chiral vector $(n, m) = (5, 5)$

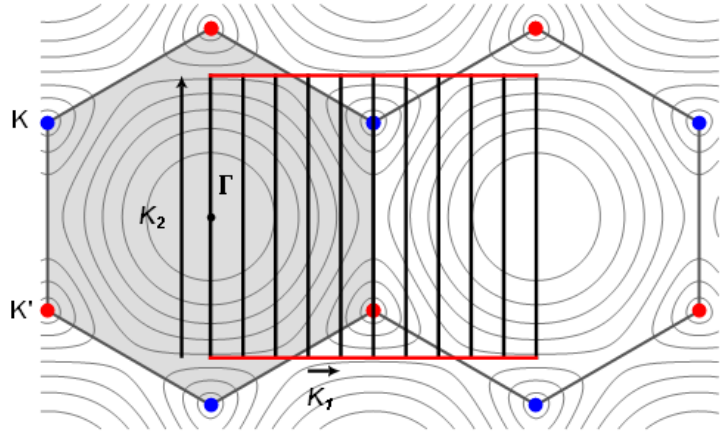

Figure I-8. An armchair metallic carbon nanotube with the chiral vector $(n, m) = (5, 5)$ The Brillouin zone of a carbon nanotube is represented by the segment line which passes through the highest symmetry point Γ. The vectors K_1 and K_2 are reciprocal lattice vectors corresponding to C_h and T, respectively. $C_h = (5, 5)$, $T = (1, -1)$, $K_1 = (b_1 + b_2) / 10$, $K_2 = (b_1 - b_2) / 2$ and $N = 10$.

- A zigzag semiconducting carbon nanotube with the chiral vector $(n, m) = (8, 0)$

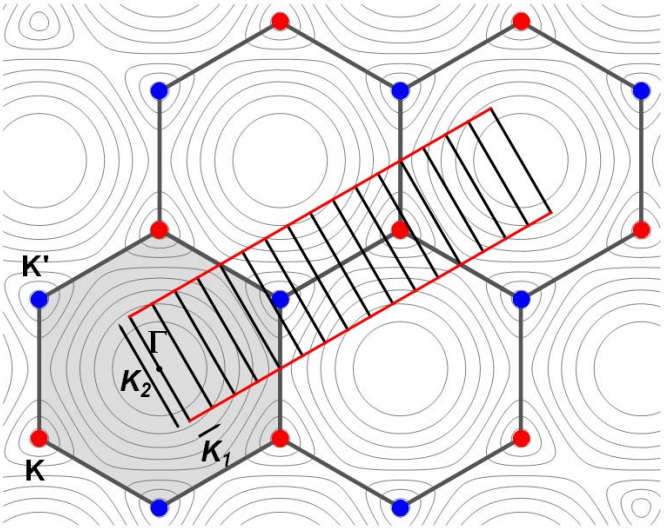

Figure I-9. A zigzag semiconducting carbon nanotube with the chiral vector $(n, m) = (8, 0)$. The Brillouin zone of a carbon nanotube is represented by the segment line which passes through the highest symmetry point Γ. The vector K_1 and K_2 are reciprocal lattice vectors corresponding to C_h and T, respectively. $C_h = (8, 0)$, $T = (1, -2)$, $K_1 = (2b_1 + b_2)/16$, $K_2 = -b_2/2$, and $N = 16$.

The energy dispersion relations of these three types of nanotubes are shown in Figure I-10.

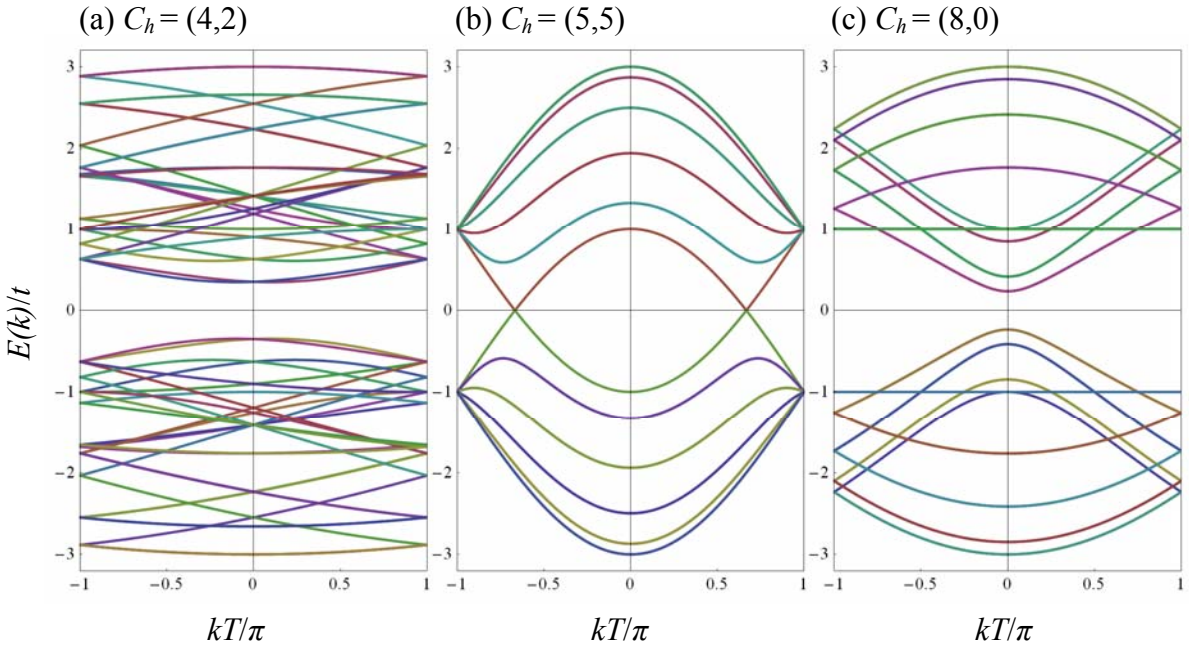

Figure I-10. One-dimensional energy dispersion relations (a) for an semiconducting nanotube (n, m) = (4, 2) for values of the energy between $-t$ and t, in dimensionless units $E(k)/t$. The Fermi level is at $E = 0$. (b) For an armchair metallic nanotube we take (n, m) = (5, 5); (c) for a zigzag semiconducting nanotube, (n, m) = (8, 0). Note that the numbers of subbands are $2N$ and some of them are degenerate.

I-5 Single-Electron Transistor (SET)

Having discussed the basic electronic properties of carbon nanotubes, we now discuss their low-temperature transport properties. One of the important phenomena observed is when the nanotube behaves as an island for charge and exhibits so-called SET behavior. A SET generally consists of a small size of metallic island sandwiched between two tunnel junctions, which is connected to source and drain electrodes, and a third electrode called the gate electrode which can tune the electrical potential of the island capacitively. It can also be regarded as a field-effect transistor in which the channel is replaced by two tunnel junctions forming a metallic island. Generally speaking, an SET demonstrates a few essential features, phenomena, and regimes of operation which will be discussed in the following sections.

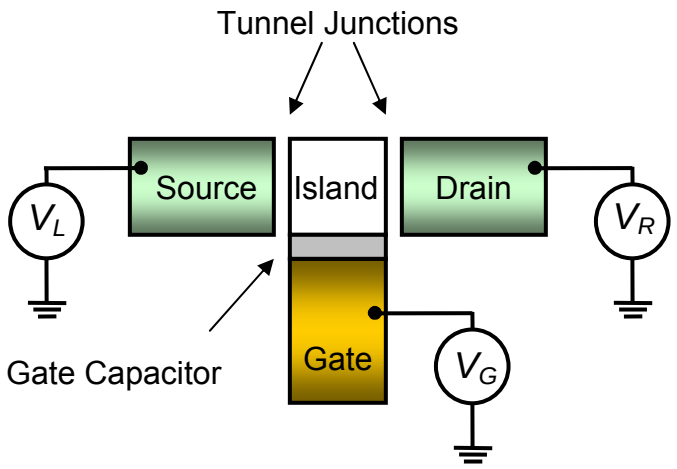

Figure I-11. A schematic diagram of single-electron transistor

I-5-1 Quantum Dots

A quantum dot is a small size of metallic island; electrons are strongly restricted by the spatial confinement in each dimension, which causes the energy in this island to be quantized as an artificial atom, analogous to the electron in the hydrogen atom. In order to study the intrinsic properties of a quantum dot, two tunnel junctions are made to connect to source and drain electrodes (see Figure I-11); both act as electron reservoirs. In addition, the electrical potential of the island can be tuned by a gate electrode capacitively coupled to the island. In our case, the carbon nanotube in our system actually acts as a quantum dot usually at low temperature as electrons are confined in a length direction, producing discrete energy levels.

I-5-2 Tunnel Junctions

Tunnel junctions play a critical role in Coulomb blockade phenomena. A tunnel junction can be modeled by a parallel resistor-capacitor circuit shown in Figure I-12. The tunneling resistance R_T is a phenomenological quantity which is defined when the bias voltage V is applied to the electrodes on either side of the tunnel barriers. Electron transport through the junction occurs, even though from a classical point of view their energy would not be enough to overcome the potential barrier within the junction. Thus,

transport in the Coulomb blockade regime is a quantum mechanical phenomenon. Moreover, the capacitance in the tunnel junctions has to be very small, in order to produce a Coulomb charging energy $E_C = e^2/2C$ for a single electron that is larger than the available thermal energy.

I-5-3 Electrostatic Energy of SETs

Consider a metallic island connected to any number of voltage sources V_i, the electrostatic energy of a symmetric generalized circuit in Figure I-12, and those tunnel junctions viewed as capacitor C_i and tunneling resistance R_i. Note the system has to be considered with respect to the same reference point, though it can be arbitrary. When there are n number of electrons added to the island from an initially neutral condition, we start with charge neutrality and obtain

$$-ne = \sum C_i (V_i - \varphi) .$$

Then the potential $\phi = \dfrac{\sum C_i V_i + ne}{C_\Sigma}$, where $C_\Sigma = \sum C_i$ the total capacitance.

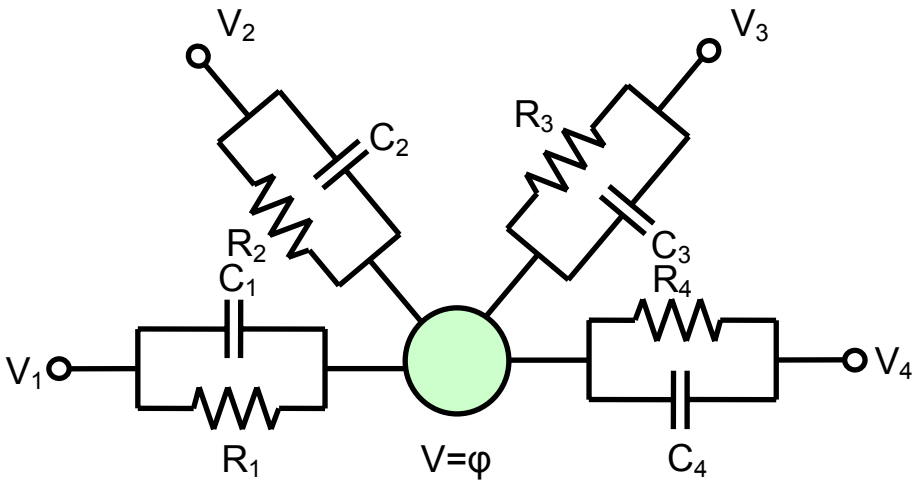

Figure I-12. Schematic diagram of a generalized single-island circuit, with a number of linkages to voltage sources. R_i is a tunneling resistance.

Thus, the total internal energy is

$$U = \frac{1}{2}\sum C_i (V_i - \varphi)^2$$
$$= \frac{1}{2C_\Sigma}\sum_i \sum_{j>i} C_i C_j (V_i - V_j)^2 + \frac{(ne)^2}{2C_\Sigma} \ .$$

The above equation states the Coulomb energy of n number of electrons and all applied voltage sources V_i. The work due to tunneling of an electron in or out of the island has to be considered in the total energy. When an electron is added to the island, the potential φ of the island will shift by e/C_Σ, while the fraction of the change is eC_i/C_Σ for each capacitor. The work done by each voltage source is $-eV_iC_i/C_\Sigma$, except at the injecting junction j, where it is $\left(1 - C_j/C_\Sigma\right)eV_j$. The total work done in the system is

$$W_j = e\sum_i (V_j - V_i)\frac{C_i}{C_\Sigma} \ .$$

Thus the total energy E is

$$E = \frac{1}{2C_\Sigma}\sum_i \sum_{j>i} C_i C_j (V_i - V_j)^2 + \frac{(ne)^2}{2C_\Sigma} + W_j \ .$$

In one of the carbon nanotube resonator projects in Chapter III, Figure III-19, we assume there are n number of electrons injecting from drain electrode,

$$W_R = ne(V_R - V_L)\frac{C_L}{C_\Sigma} + ne(V_R - V_G)\frac{C_G}{C_\Sigma} \ .$$

So total Enthalpy E is

$$E = \frac{1}{2C_\Sigma}\sum_i \sum_{j>i} C_i C_j (V_i - V_j)^2 + \frac{(ne)^2}{2C_\Sigma} + ne(V_R - V_L)\frac{C_L}{C_\Sigma} + ne(V_R - V_G)\frac{C_G}{C_\Sigma}$$
$$= \frac{(ne)^2}{2C_\Sigma} + \frac{1}{2C_\Sigma}\left[C_G C_L (V_G - V_L)^2 + C_G C_R (V_G - V_R)^2 + C_L C_R (V_L - V_R)^2\right] \qquad \text{(I-4)}$$
$$+ ne(V_R - V_L)\frac{C_L}{C_\Sigma} + ne(V_R - V_G)\frac{C_G}{C_\Sigma} \ .$$

This is the electrostatic energy of the carbon nanotube quantum dot system in Chapter III. The details of discussion can be found in Section 7.4, Introduction to superconductivity, 2nd edition by Michael Tinkham.

I-5-4 Coulomb Blockade Oscillations

The typical total charge and transport curves yielded by Coulomb blockade are shown in Figure I-13 (a) and (b), demonstrating both a staircase in charge and separate peaks successively in conductance. In the Coulomb blockade regime, as each Coulomb oscillation corresponds to the addition of one electron entering the island, the number of charges added to an island can be precisely counted.

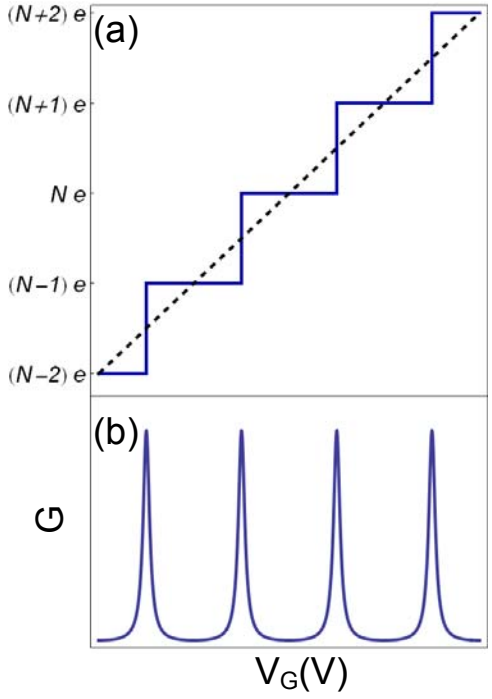

Figure I-13. Coulomb blockade phenomena. (a) The staircase function of charge versus gate voltage V_G. (b) The coulomb oscillations in conductance; the maximum is achieved when the ideal number of charges is a half integer.

Here, Coulomb blockade in single-electron transistor scheme will be discussed from the energy point of view. We start with *n* number of electron charges giving a total charge *ne* on an island, and here we assume there is zero bias between source and drain voltages (V_L and V_R, respectively), with the drain contact grounded, yielding $V_L = V_R = 0$. The total equilibrium electrostatic energy is

$$\begin{aligned} E &= \frac{1}{2C_\Sigma}\left[(ne)^2 + 2neC_G V_G + C_G(C_R + C_L)V_G^2\right] \\ &= \frac{1}{2C_\Sigma}(C_G V_G + ne)^2 + \frac{1}{2}C_G(1 - 2C_G/C_\Sigma)V_G^2 \,. \end{aligned} \tag{I-5}$$

Minimizing the energy with respect to *n*, we obtain $n = -C_G V_G / e$, corresponding to an induced charge $Q_0 = -C_G V_G$. Note that the charge Q_0 on the tunnel junction capacitor is a continuous variable since it describes the whole displacement of electron density in the electrode with respect to the positive ionic background. Thus, Q_0 can be an arbitrary small fraction of the charge quantum *e*.

However, since *n* must be an integer, the minimum energy for given Q_0 is obtained if *n* is the closest integer to Q_0/e. That is, the *n* giving the lowest energy in eq. (I-5) must lie in the range

$$\frac{Q_0}{e} - \frac{1}{2} \le n \le \frac{Q_0}{e} + \frac{1}{2} \tag{I-6}$$

More generally, eq. (I-5) generates a family of parabolic curves shown in Figure I-14 (here we neglect a constant contribution to the energy).

Thus, when the gate voltage V_G is swept down, one electron tunnels out of the metallic island at each crossing point, changing the number of extra electrons on the island from *n* to *n-1*. When an infinitesimal bias voltage is applied, the electron can go in or out of the island at the crossing points without having to overcome any energy barrier even at $T = 0$,

thus there will be a steady current response to the bias whenever V_G is swept through the values of Q_0/e as a half-integer of *e*, giving rise to a series of current peaks. This phenomenon yields the Coulomb blockade oscillations shown in Figure I-13(b).

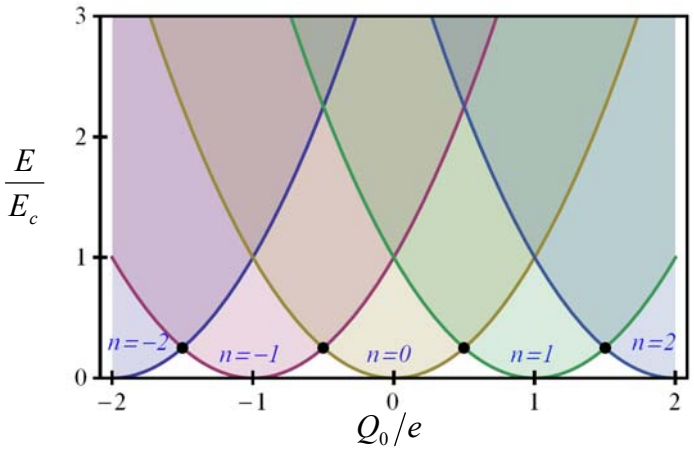

Figure I-14. The *n*-dependent part of the circuit energy *E* as a function of the gate charge Q_0 at $T = 0$. The black crossing points indicate where the *n* and *n*+1 (*n*−1) charge states are degenerate.

Finally, in order to observe the Coulomb blockade clearly, two conditions must be satisfied. (1) The charging energy must be larger than the thermal energy ($E_C > k_B T$) to avoid thermal fluctuations washing out the features. (2) the tunneling resistance must exceed the quantum resistance $R_Q = h/2e^2 \cong 12.9\,\mathrm{k}\Omega$, since the charge energy $e^2/2C$ needs to in exceed the quantum energy uncertainty $\Delta E \;\; \hbar/\Delta t \approx \hbar/RC$ associated with the finite lifetime of the charge on the island. Thus we obtain $R \geq 2\hbar/e^2 \approx R_Q$, which can be seen as the boundary of "open" and "closed" quantum dots.

In a carbon nanotube quantum dot system, we observe Coulomb blockade oscillations as long as the tunneling resistance is not too low to be an open quantum dot, in which case quantum fluctuations of the charge smear out the Coulomb blockade, which has been shown to yield a regime of Fabry-Perot type interference in a nanotube electron waveguide [8].

Chapter II

Ballistic Phonon Thermal Transport in Multiwalled Carbon Nanotubes[9]

II-1 Abstract

We report electrical transport experiments, using the phenomenon of electrical breakdown to perform thermometry, that probe the thermal properties of individual multiwalled carbon nanotubes. Our results show that nanotubes can readily conduct heat by ballistic phonon propagation. We determine the thermal conductance quantum, the ultimate limit to thermal conductance for a single phonon channel, and find good agreement with theoretical calculations. Moreover, our results suggest a breakdown mechanism of thermally activated C-C bond breaking coupled with the electrical stress of carrying $\sim 10^{12}$ A/m^2. We also demonstrate a current-driven self-heating technique to improve the conductance of nanotube devices dramatically.

II-2 Introduction

The ultimate thermal conductance attainable by any conductor below its Debye temperature is determined by the thermal conductance quantum [10, 11]. In practice, phonon scattering reduces the thermal conductivity, making it difficult to observe quantum thermal phenomena except at ultralow temperatures [12]. Carbon nanotubes have remarkable thermal properties [13-16], including conductivity as high as 3000 W/m·K [17]. Here we report the observation of ballistic phonon motion and quantum thermal transport in micron-scale individual carbon nanotube devices, demonstrating the universal limit to thermal transport. In this qualitatively different regime, quantum mechanics limits the entropy flow, giving a maximum thermal conductance and an absolute physical limit to the information bandwidth that a nanotube can transport per unit power [10, 11]. From our data, we obtain a measurement of the thermal conductance quantum that is in good agreement with theory.

Very recently the thermal conductance of a carbon nanotube attached to an atomic force microscope (AFM) tip has been observed to be independent of the AFM retraction length, and the result was interpreted in terms of ballistic phonon propagation[18]. However, the phonon scattering length and thermal conductance quantum were not determined.

In our experiments, we heat multiwalled nanotubes (MWNTs) with an electrical current and monitor temperature by the electrical breakdown phenomenon [19, 20]. Our data yield an experimental measurement of the thermal conductance quantum, which agrees with theoretical predictions [10, 11, 21] as well as thermal transport results on cryogenically cooled Si_3N_4 nanobridges [12]. This demonstrates that fundamental knowledge about thermal transport in nanotubes can be obtained from an electrical transport experiment. This knowledge, which is challenging to obtain by other means, also contributes toward understanding thermal management issues relevant to the rational design of nanotube interconnects and logic devices.

II-3 Sample Fabrication

Our multi-walled carbon nanotubes (MWNTs) were provided in powder form by the Forró group in Ecole Polytechnique Fédérale de Lausanne (EPFL), Switzerland. A small amount of the MWNTs powder is dispersed into 1,2-dichloroethane by overnight sonication; meanwhile, an array of Au/Cr alignment markers are patterned on a heavily doped Boron (p++) silicon wafer with 1 micron thermally grown silicon oxide (see process (a)–(d) in Figure II-1). This patterning process is called electron-beam lithography (EBL); we perform this process by using the Nanometer Pattern Generation System (NPGS) integrated in a Scanning Electron Microscope (Model S-4100 Field Emission Hitachi SEM).

One drop of well-dispersed MWNT solution is placed on the pre-patterned alignment markers substrate and rinsed by using isopropanol alcohol (IPA) followed by a nitrogen blow drying (see process (e)–(f) in Figure II-1).

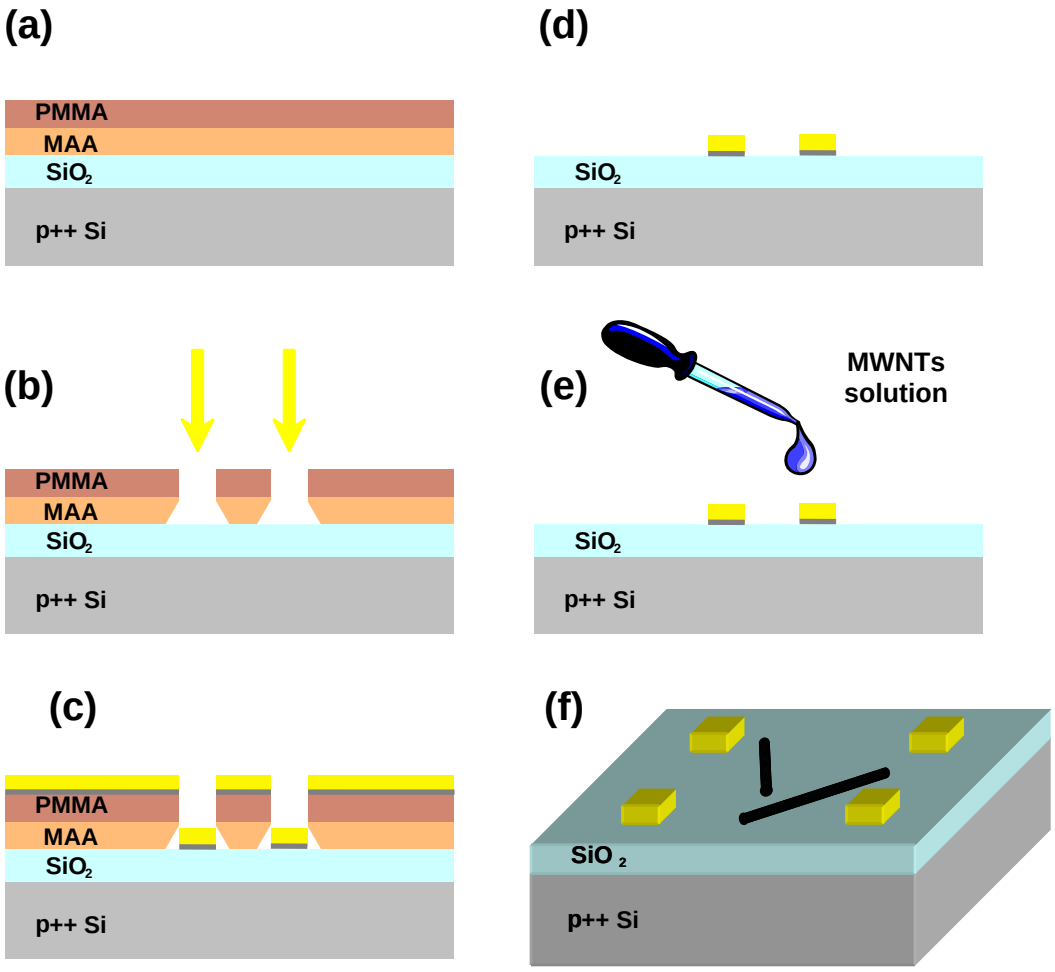

Figure II-1. Electron beam lithography for alignment markers and MWNTs deposition. (a) PMMA/MAA bi-layer of positive resist is spun on the substrate. (b) An electron beam exposes the defined area and the sample is developed to create a window. (The undercut of MAA layer will help make the lift-off process (d) easier.) (c) Au/Cr metals are thermally evaporated onto the surface of substrate through the windows. (d) Lift-off of the remaining resists in acetone; alignment markers are revealed. (e) MWNT solution deposition. (f) Randomly scattered nanotubes with alignment markers

After the MWNT deposition process is done, the samples are placed inside a 1 inch quartz tube furnace, and heated up to 350ºC for 30 minutes with moderate oxygen flow rate. This hot oxygen cleaning process removes soot, amorphous carbon, and any organic detergent residue, which are byproducts of the nanotube production and purification.

After the nanotubes are successfully deposited on substrate, we use an atomic force microscopic (AFM) to locate nanotube positions relative to the defined alignment markers (see Figure II-2(a) and (b)). Note that the van der Waals force is strong enough to anchor the nanotubes to substrate very well [22, 23]; therefore nanotube positions remain the same even under multiple rinsings, chemical processings and AFM imagings, (although partial movement can occur at very high power sonication or manipulation by AFM tips).

A computer-aided design (CAD) layout is made for electrodes which bridge two ends of nanotubes and extend to the extensive bonding pads. A second EBL is performed to create the contact electrodes (see Figure II-2 (c)).

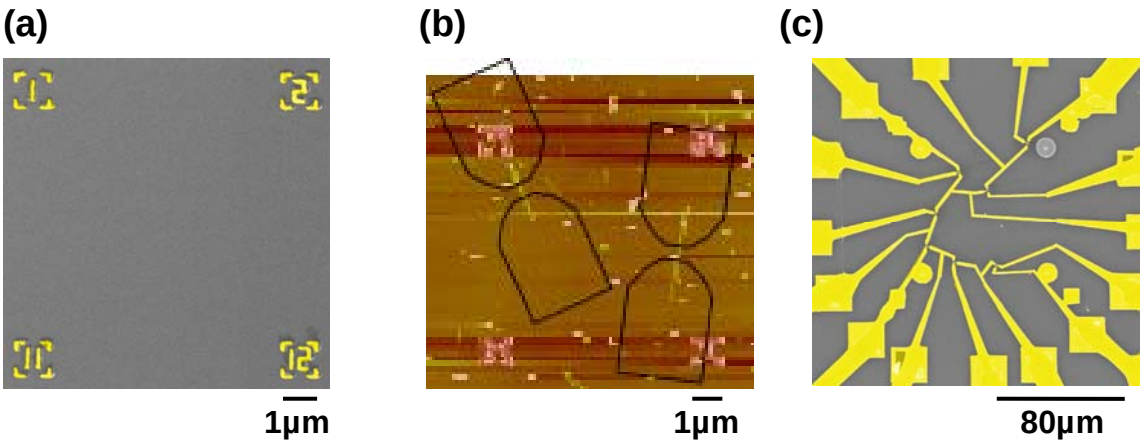

Figure II-2. Image of alignment markers and nanotube devices. (a) SEM image of the alignment markers; total area covers 10×10 markers, run from 01 to 100. (b) AFM image with pattern drawings. (c) SEM image of a zoom-in complete device layout, the bonding pads are not shown.

In our experiment, we have two different device configurations shown in Figure II-3; one is substrate-supported MWNTs and the other one is doubly clamped freestanding MWNTs, shown in Figure II-3 (a) and (b), respectively. The suspended nanotube devices go through an extra step of oxide etching, which usually is performed in buffered oxide etch (BOE, aqueous NH_4-HF etchant solutions) with gentle agitation followed by a sequence rinse. We often chose isopropyl alcohol (IPA) or methanol as the final rinse solution since these solvents have much less surface tension than water (72.8 mN/m at

25°C). For a two-electrode geometry, we can usually use the metal electrodes as etch masks, thus the distances between source and drain electrodes can be easily brought down to 100 nm.

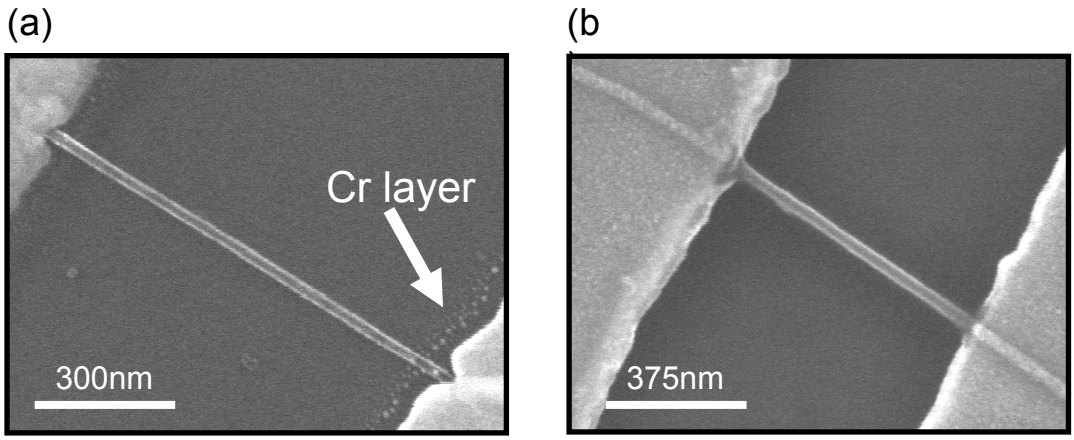

Figure II-3. SEM images of two device configurations. (a) A substrate-supported MWNT with visible diffused Cr skirt due to MMA undercut (b) A doubly clamped freestanding MWNT

If the suspended length is designed to be less than 500 nm for SWNTs, or the aspect ratio is small for MWNTs, there are two options to suspend nanotubes. In the first option, samples can be taken out directly from isopropyl alcohol (IPA), and baked on a preheated hotplate (~ 55°C), letting it dry. In the second option, we heat up methanol with the sample immersed and take the sample out from the beaker while the methanol is boiling. However, the yield from the first option is typically acceptable. We have also developed a more sophisticated process to suspend SWNTs in a different device configuration, which is detailed in Chapter III. Note that we didn't find any noticeable quality loss in the nanotube characteristics by the BOE etch.

Figure II-4. Schematic diagram of metal electrodes as the etch mask. Undercut structures are always present after etching.

II-4 Experimental Approach

In this research, we adopt electric breakdown as our main experimental indicator to probe the thermal properties of MWNTs. There are two major factors that lead us to this approach. One is that the shell-by-shell breakdown occurs in a series of abrupt processes in which we can monitor the onset of each one; the other factor is that breakdown temperature T_B can be taken to be a constant, intrinsically determined by the carbon-carbon binding energy. Thus the electrical breakdown of a nanotube acts as a nanoscale thermometer.

The observation of electrical breakdown in a MWNT system [19] was inspired by the early study of metallic SWNTs in which their current carrying capacities exceed 10 $\mu A/nm^2$ [24], while most the metal wires can only reach up to 10 nA/nm^2, limited by the electromigration. The exceptionally high current capacity of carbon nanotubes is attributed to their strong carbon-carbon bonds. Instead of electromigration (a nonthermal current-assisted diffusion process) to metal wires, MWNTs fail via a series of sharp current drops in abrupt events separated by ~ 1 sec (see Figure II-5), due to the ablation of individual nanotube shells in sufficiently high electrical power dissipation in conjunction with the electrical stress of carrying a large current. This behavior was recently imaged by transmission electron microscopy (TEM) [25]. It was carefully argued that the breakdown temperature T_B was ~ 900K [19]. Nevertheless, Joule heating alone is not likely to account entirely for the shell breakdown [26].

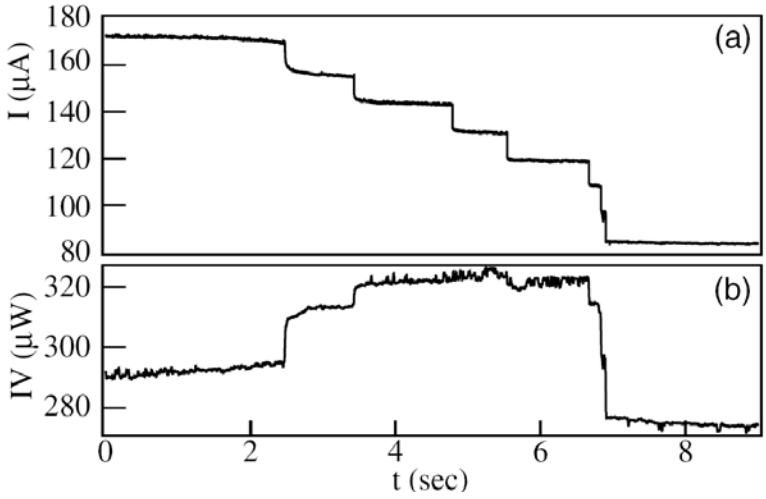

Figure II-5. Time trace of the current *I*(t) and dissipated power *P*(t) during a MWNT breakdown from ref. [19] (a) The current exhibits a staircase of stable currents separated by 12 μA steps. (b) Power *P*(t) during the electrical breakdown

In our experiments, the electrical breakdown is performed in an argon ambient environment by applying a high bias voltage between source and drain (see in Figure II-7); simultaneously monitoring the breakdown current. One of our typical device I-V curves is shown in Figure II-6 and the sudden current drop that occurs indicates the breaking of the outermost shell.

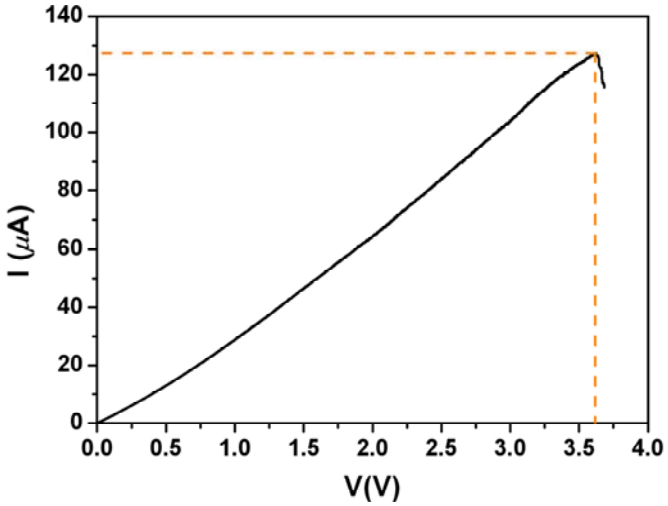

Figure II-6. *I-V* curve of a MWNT during the outermost shell breakdown. The breakdown power is about 460 μW for this device.

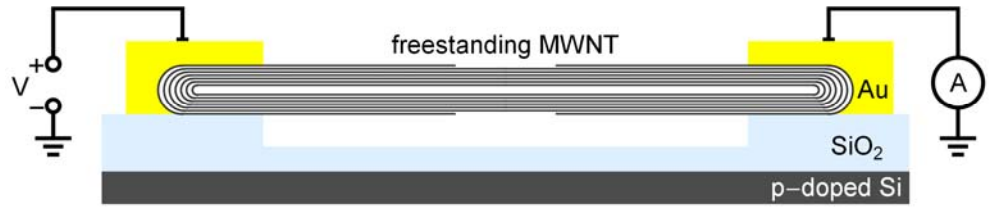

Figure II-7. The schematic diagram of a doubly clamped freestanding MWNT with the ablation of the outermost shell breakdown

II-5 Thermal Transport

According to the previous section, the breakdown temperature is assumed to be ~ 900K [19]. In order to address the role of breakdown temperature in nanotube breakdown, we start with the heat transfer mechanism in two different device configurations: freestanding and substrate supported. In the later one, the substrate yields an additional cooling pathway. In the IV curve from Figure II-6, the breakdown power is measured at ~ 460 μW; this implies it must have sufficient amount of electrical power dissipating in the MWNTs before the breakdown occurs and Joule heating is likely a significant factor in the breakdown process. In order to understand the temperature profile, models of heat transfer in both systems are required; three types of heat dissipation mechanisms: conduction, convection, and radiation, will be introduced and examined in our system.

II-5-1 Convention

First, we can eliminate the cause of heat dissipation from a convection mechanism; as mentioned before, we typically performed our measurement in an argon ambient environment to prevent any oxygen from initiating the breakdown at a lower power [19]. The devices were enclosed in a small chamber during the measurement while a slight argon overpressure prevented air flow inwards. However, we found similar breakdown power thresholds in Ar as were found in previous measurements in vacuum [19], which rules out convection as a significant cooling mechanism.

II-5-2 Radiation

Radiation can also dissipate heat from a hot source as long as a temperature difference exists. According to Stefan-Boltzmann law, the emissive power (total energy radiated per unit area per unit time) is $E_b = \varepsilon\sigma T_s^4$, where $\sigma = 5.67\times10^{-8}\, W/m^2\cdot K^4$ is the Stefan-Boltzmann constant, ε, emissivity and T_s surface temperature. Since the breakdown temperature is assumed to be $T_B \sim 900K$, we can estimate the radiation-heat transfer rate q_R for a 2 μm length and 30nm diameter half surface exposure MWNT, based on the assumption that the emissivity is unity and all the surface is at breakdown temperature.

$$\begin{aligned} q_R &= \sigma A_s \varepsilon (T_s^4 - T_R^4) \\ &= 5.67\times10^{-8}\cdot(\pi DL/2)\cdot 1\cdot(900^4 - 300^4)\, W \\ &\sim 3.5\, nW \end{aligned}$$

Based on the above the estimate (~ 3.5 nW) and the experimental breakdown power (~ 460 μW), we can simply ignore heat dissipation through radiation.

II-5-3 Conduction

Conduction is the heat transfer through a solid or a stationary fluid. Considering all metal electrodes, substrate, and argon ambient environment, however, the thermal conductivity of argon is four orders of magnitude smaller than the gold and two orders of magnitude smaller than silicon oxide, so it is practical to ignore the heat dissipation through the argon. Thus, we will focus on the conduction through the silicon oxide and metal.

II-5-4 Free-Standing Carbon Nanotube

From Fourier's law

$$q_x'' = -\kappa\frac{dT}{dx}, \qquad \text{(II-1)}$$

heat flux $q_x''\left(W/m^2\right)$ is the heat transfer rate in the x direction per unit area perpendicular to the direction of transfer, and κ is the thermal conductivity $\left(W/m\cdot K\right)$. Here we define the heat transfer q with unit in power (W). Consider an infinitesimal volume $dV = dx\,dy\,dz$, if there are temperature gradients, conduction heat transfer will occur across each of the volume surfaces—for example in x direction, the inflow q_x is not necessarily equal to the outflow q_{x+dx}, where we can use the Taylor series expansion, $q_{x+dx} = q_x + \frac{\partial q_x}{\partial x}dx$ while neglecting higher-order terms. Similar expressions are obtained for the y and z direction. On a rate basis, the general form of conservation energy requirement is

$$\dot{E}_{in} - \dot{E}_{out} + \dot{E}_g = \dot{E}_{st} \tag{II-2}$$

where $\dot{E}_{in}$, $\dot{E}_{out}$ are denoted as the energy inflow and outflow; $\dot{E}_g = \dot{q}\,dx\,dy\,dz$ is the energy generated in the volume, and energy storage term $\dot{E}_{st} = \rho c_p \frac{\partial T}{\partial t}dx\,dy\,dz$, where

$\rho c_p \frac{\partial T}{\partial t}$ is the time rate of change of the internal energy of the medium per unit volume.

After considering inflow and outflow of the control element, we get

$$-\frac{\partial q_x}{\partial x}dx - \frac{\partial q_y}{\partial y}dy - \frac{\partial q_z}{\partial z}dz + \dot{q}\,dx\,dy\,dz = \rho c_p \frac{\partial T}{\partial t}dx\,dy\,dz\,. \tag{II-3}$$

Dividing by the control volume from eq. (II-3) we can simplify the expression to the following

$$-\frac{\partial q_x''}{\partial x} - \frac{\partial q_y''}{\partial y} - \frac{\partial q_z''}{\partial z} + \dot{q} = \rho c_p \frac{\partial T}{\partial t}\text{.h} \tag{II-4}$$

Substituting from eq. (II-1), one can get the heat diffusion equation in Cartesian coordinates

$$-\frac{\partial}{\partial x}\left(\kappa\frac{dT}{dx}\right)-\frac{\partial}{\partial y}\left(\kappa\frac{dT}{dy}\right)-\frac{\partial}{\partial z}\left(\kappa\frac{dT}{dz}\right)+\dot{q}=\rho c_p\frac{\partial T}{\partial t}.$$

Thus, the one-dimensional heat diffusion equation in steady state is $\frac{\partial}{\partial x}\left(\kappa\frac{dT}{dx}\right)+\dot{q}=0$. Here we denote the electrical power $\dot{q}$ generated inside the nanotube as P. The general solution to this equation, assuming a constant κ, is $T=-\frac{P}{2\kappa}x^2+C_1x+C_2$. In the free-standing MWNTs case, the only channel for the heat to dissipate into the environment is through the electrodes. Since the thermal conductivity of the Au electrodes is good enough to provide a thermal anchor at room temperature, the boundary condition is a constant temperature at the nanotube ends $T(0,t)=T(L,t)=T_{room}$. The solution for $T(x)=\frac{P}{2\kappa}(L-x)x+T_{room}$ is a parabolic distribution in which the maximum temperature exists at the midpoint. The breakdown power is then

$$P=\frac{8\pi R^2\kappa}{L}(T_B-T_{room})=\frac{8\pi R^2\kappa}{L}\Delta T.$$

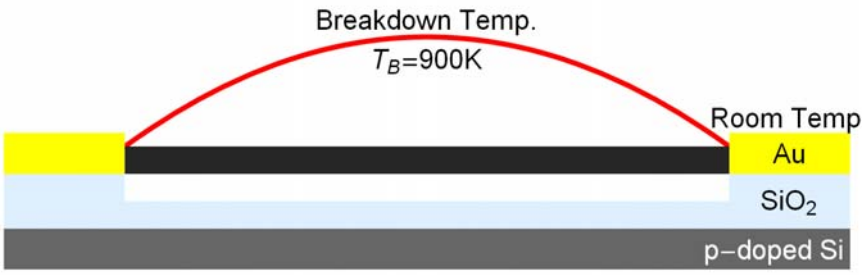

Figure II-8. Temperature distribution along nanotube for freestanding case in heat diffusion regime

II-5-5 Substrate-Supported Carbon Nanotube

For the substrate-supported nanotube, we can simply model the nanotube as immersed in the silicon oxide, with the heat mainly is spreading out through the substrate. We can write down the heat equation in cylindrical coordinates, only considering the radial part by symmetry.

We consider the situation right before breakdown. The tube accumulates the heat and reaches the breakdown temperature, in that moment, the nanotube temperature is in steady state. Consider the energy conservation in the cylindrical geometry for the steady-state conditions seen in Figure II-9. R is the nanotube actual radius, R_0 is the estimated radius for silicon oxide where room temperature conditions prevail.

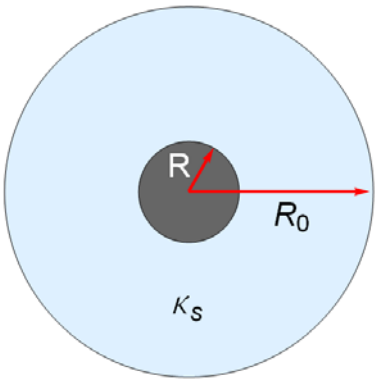

Figure II-9. The radial part of R is the nanotube radius and R_0 is an imaginary cutoff radius.

With heat generation from carbon nanotube and dissipating through silicon oxide, we consider the Fourier's law, eq. (II-1), in radial direction. Therefore,

$$P = q_r = -\kappa_s A \frac{dT}{dr} = -\kappa_s (2\pi r L) \frac{dT}{dr}.$$

Thus, we can find the relationship between the power and length of nanotube is

$$P = \frac{2\pi L \kappa_s \Delta T}{\ln(R_0 / R)}.$$

The following is the summary for these two types of device configurations.

Freestanding nanotube: $P = \frac{8\pi R^2 \kappa}{L} \Delta T$, $P \propto 1/L$

Substrate-supported: $P = \frac{2\pi L \kappa_s \Delta T}{\ln(R_0 / R)}$, $P \propto L$

Note the different scaling for the two situations with the nanotube length.

II-6 Breakdown Temperature Investigation

To examine the dissipated power versus the nanotube length, we selected a few nanotubes with similar diameters. Figure II-10 (a) shows current-voltage (*I-V*) data from three freestanding nanotube devices with radius R = 10 nm, determined by SEM imaging. Note that we carefully calibrated the SEM radius measurements by comparing SEM images to AFM images on the same nanotube for a selected subset of the nanotubes. We also note that the typical diameter of the nanotubes used in this study is 15–25 nm, which exceeds our SEM's typical resolution of < 3 nm. Figure II-10 (b) shows similar data for supported nanotubes, with R = 8 nm, 9 nm, and 14 nm. At breakdown, the resistance is directly proportional to the nanotube length, indicating negligible contact resistance. From our IV data, we deduce the breakdown power *P* for each first shell.

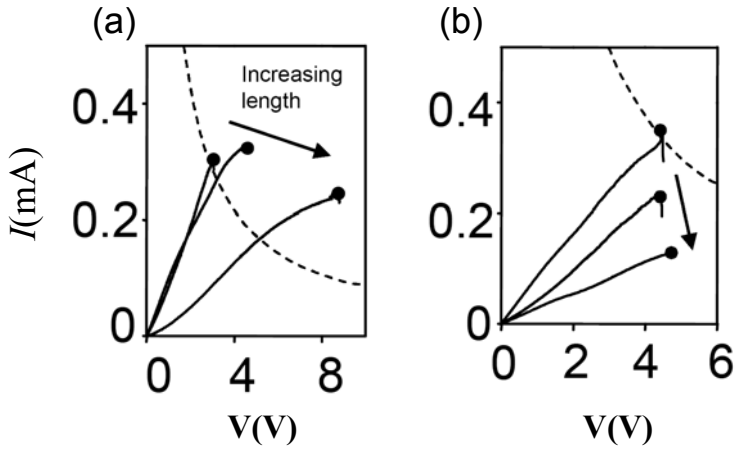

Figure II-10 *I-V* curves for two device configurations. (a) *I-V* characteristic from freestanding nanotube devices with R = 10 nm. The arrow indicates increasing lengths (0.50, 0.64, and 1.58 μm). Dotted line: isopower curve. (b) *I-V* characteristic of substrate-supported devices with R = 8, 9, and 14 nm increasing in length (0.74, 1.26, and 1.66 μm) following the arrow. Dotted line: isopower curve

Figure II-11 shows a log-log plot of P versus L. Freestanding tubes approximately follow $P \propto L^{-1}$ behavior, while the supported tubes exhibit $P \propto L$ behavior. This behavior can be understood using a diffusive thermal transport model. For freestanding tubes, the power P to increase the temperature at the tube center by ΔT is $P = 8\pi R^2 \kappa \, \Delta T / L$, where κ is the characteristic nanotube thermal conductivity. With T_B ~ 900 K, a linear fit to our data with $\Delta T \sim 600$ K (dashed line in Figure II-11) yields a thermal conductivity of $\kappa \approx 600 W/m \cdot K$, consistent with previous thermal conductivity measurements on individual MWNTs in the diffusive regime [17].

For supported nanotubes, the relation $P \propto L$ indicates that the cooling occurs mainly by heat conduction into the substrate. We estimate heat transport in this geometry as between concentric cylinders. This yields $P = 2\pi L \kappa_s \Delta T / \ln(R_0/R)$, with R_0 the outer cylinder radius at which T drops to the ambient value, and κ_s the substrate thermal conductivity. Taking R_0 = 50 nm and R = 10 nm, the fit shown by the dotted line in Figure II-9 yields $\kappa_s \sim 0.5 W/m \cdot K$, in agreement with the bulk thermal conductivity of

SiO_2 $\kappa_s \sim 1.5 W/m \cdot K$. Considering the two cases together, our data and analysis indicate that the shell ablation occurs at a well-defined temperature T_B.

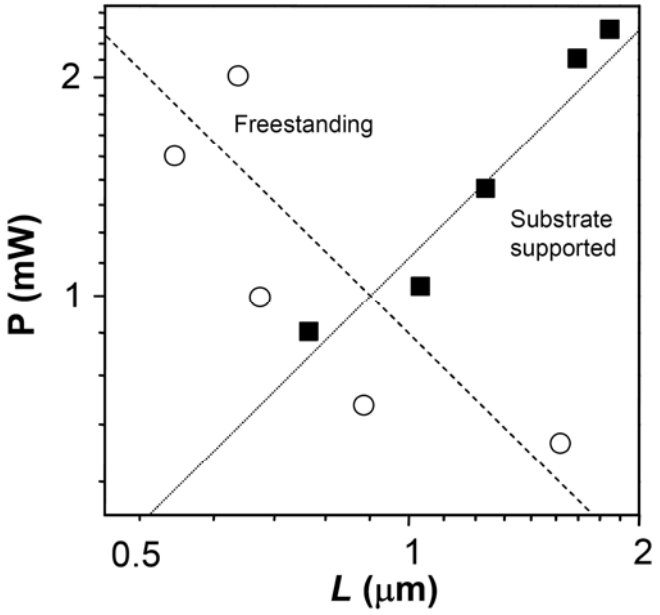

Figure II-11. P versus L on a log-log scale for freestanding tubes (open circles) and substrate-supported nanotubes (filled squares). Dotted line: $P \propto L$, dashed line: $P \propto L^{-1}$

II-7 Short Free-Standing MWNTs

We now focus on freestanding devices, representing a broad range of L and R values. Figure II-12 shows $P_N = P/8\pi R^2$ versus L^{-1} for ~ 30 samples. Based on diffusive heat transport, we expect plotting the normalized power $P_N = P/8\pi R^2$ versus L^{-1} should yield a straight line with a slope of $T_B \kappa$. Remarkably, although the initial trend for the longer tubes appears linear, for nanotubes with $L^{-1} \geq (0.5\,\mu\text{m})^{-1}$ (filled squares) P_N saturates and becomes L independent. We note that this cannot be explained by electrical contact resistance. Power dissipation at the contacts should be less effective in heating the nanotube than power dissipation in its bulk, because the contacts provide the most direct thermal anchoring to ambient temperature conditions. This would increase the breakdown power for shorter tubes, contradicting the saturation behavior we observe.

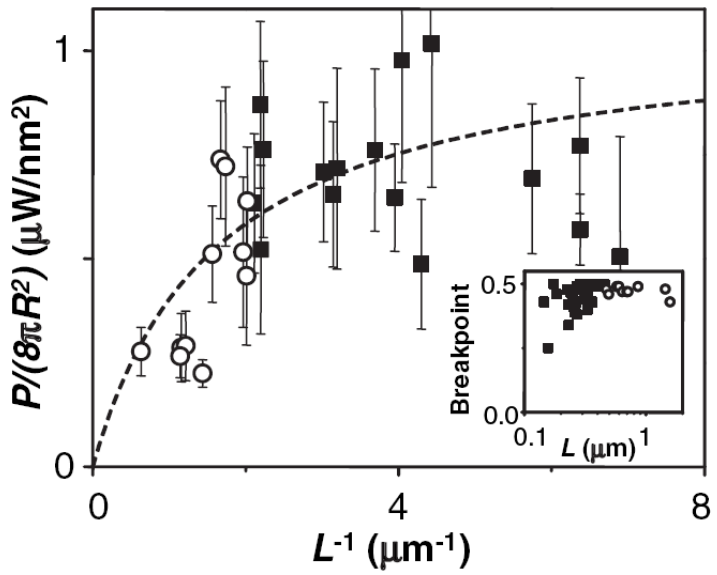

Figure II-12. The plot of normalized power $P/(8\pi R^2)$ *vs* L^{-1}. Open circles: longer tubes. Filled squares: shorter tubes. Dashed line: fit to data for an interpolation formula described in text. Inset: breakpoint position normalized to L versus L on log scale.

This shows that heat flow from the nanotube occurs at an L-independent rate, depending only on R. The rest of the shells are then broken, producing a gap in the

nanotube. The Figure II-12 inset shows the gap position, normalized to the suspended tube length. This breakpoint is near the center for tubes longer than ~ 0.5 μm, but for L in the saturation regime the scatter in the breakpoint values increases. As the statistical distribution of breakpoints reflects the temperature distribution along the nanotube, this suggests the nanotube temperature becomes more spatially uniform as they become shorter than 0.5 μm.

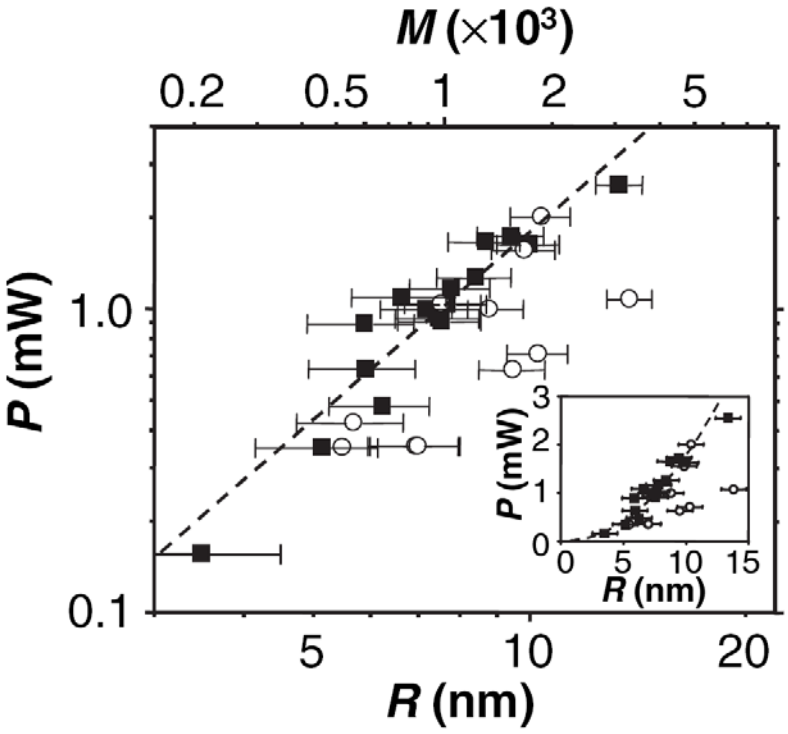

Figure II-13. Log-log plot of P versus R (lower scale) and M (upper scale). Open circles: longer tubes. Filled squares: shorter tubes. Dashed line: power-law fit to short nanotube P versus R and M data. Inset: Linear plot of P versus R and fit.

Figure II-13 shows P versus R on a log-log scale. Data from short tube samples follow the power-law fit, showing that $P \propto R^{\alpha}$, with $\alpha = 2.1$. Some data from longer samples fall near the line, but for the longest nanotubes, the data points fall below the line. The curve followed by the short nanotube data represents an upper limit to P; modulo experimental scatter, data for each nanotube falls on or below the curve and

achieves the maximum only for nanotubes with $L \leq 0.5\,\mu m$. The Figure II-13 inset shows the same data and fit on a linear scale.

II-8 Explanations

We now consider interpretations for this behavior. One possibility is that a dominant metal-nanotube thermal contact resistance κ_C produces the saturation seen in Figure II-12. This is unlikely, however, as κ_C was determined to be negligible in ref. [17], which also used metal contacts as thermal reservoirs, as well as in ref. [18] which used graphite contacts as a thermal reservoir. Finally, based on the supported tubes' behavior, we would expect κ_C, and hence *P*, to be approximately independent of *R*. The observed systematic relationship $P \propto R^2$ differs sharply from this expectation.

Another possibility is that because of ballistic electron transport [27], the electrical current primarily heats the electrodes. In this case, the required power to reach T_B may be relatively *L* insensitive. However, both experiments and theory [24, 28] indicate the electronic mean free path due to phonon emission at the high biases applied to our samples is ~ 10 nm. Since each optical or zone boundary phonon emission is associated with an energy ~ 180 meV [24], we expect even for our shortest nanotube studied (~ 150 nm) that most of the energy eV provided by the electric field to each electron is converted into phonons within the nanotube.

II-9 Ballistic Transport in MWNTs

We now discuss the possibility of ballistic phonon transport within the nanotube. In this picture, a diffusive heat transport regime with umklapp interphonon scattering as the dominant scattering mechanism [17] makes a transition to a ballistic center-of-mass motion regime for sample lengths *L* ~ 0.5 μm. This suggests the temperature distribution along the tube should broaden as *L* decreases, consistent with the data in the Figure II-12 inset. Furthermore, because the characteristic distance the phonons travel before escaping the tube is ~ *L*/2, we would infer a characteristic umklapp scattering mean-free path l_U ~

0.2μm. We note that this situation, where the electron mean-free path is shorter than l_U, is reminiscent of the conditions prevailing in silicon-based transistors [29]. This must be accounted for to understand thermal management in Si transistors. Similar issues may therefore occur in nanotube transistor devices.

In the ballistic regime, the heat flux carried by the phonons P is given by [21, 30]

$$P_{ph} = \sum_n \int_{\omega_{n,\min}}^{\omega_{n,\max}} \frac{d\omega}{2\pi} \hbar\omega_n [\eta_{ne}(\omega_n) - \eta(\omega_n, T_0)] \xi(\omega_n) \qquad \text{(II.5)}$$

where the integration is over each of the nth photon modes' bandwidths. $\omega_{n,\max}$, $\omega_{n,\min}$ are the n^{th} phonon branch cutoff frequencies, and $\eta_{ne}(\omega_n)$ is the nonequilibrium phonon distribution for n^{th} phonon branch; $\eta(\omega_n, T_0)$ is the Bose-Einstein distribution coefficient for phonons escaping into the electrodes.

We now make several assumptions to simplify eq. (II-5). Although the geometry dependence of $\xi(\omega_n)$ for various situations was calculated by Rego and Kirczenow [31], our geometry of an extended lateral contact was not addressed. However, considering the negligibility of κ_C as discussed above, as well as the relatively large characteristic thermal phonon wave vector ~ 10^{10} m^{-1} compared to that studied in ref. [31], we take $\xi(\omega_n) \approx 1$. Moreover, since $T_B >> T_0$ we neglect $\eta(\omega_n, T_0)$ relative to $\eta_{ne}(\omega_n)$. Since breakdown depends on *P*, rather than *V* or *I* separately, the hot phonons emitted by the electrons likely achieve thermodynamic equilibrium over a thermalization length $l_{th} << L$ after a few *L*-independent characteristic number of collisions.

Additionally, we expect that the typical phonon-phonon scattering mean-free path $l_{p\text{-}p}$ should be smaller than the umklapp scattering length by $l_{p-p} \sim l_U \exp(-\Theta_D / T_B) \sim$ 10–20 nm. Given the relatively few collisions (independent of *L*) required for thermalization, we expect on these grounds also that $l_{th} \ll L$.

Thus we set $\eta_{ne}(\omega_n) = \eta(\omega_n, T)$, where T is the tube temperature. We also set $\omega_{n,\min} \approx nc/R$ [32], where $c \sim 1.5 \times 10^4\, m/s$ is the in-plane speed of sound in graphite [33]. Since T_B is considerably less than $\Theta_D \sim 2500\,\mathrm{K}$, the graphene Debye temperature, we replace $\omega_{n,\max}$ by infinity. Finally, motivated by the observed $P \propto R^2$ relationship, we assume that the thermal current is carried by the different nanotube shells in parallel. Summing over the contribution from each shell in the MWNT spaced by a = 0.34 nm independently (justified by weak coupling between graphite sheets), the power dissipated by phonons exiting the nanotube is then

$$P_{ph} \approx 2\varsigma(3)(k_B T)^3 \frac{R^2}{\pi \hbar^2 ac} \tag{II-6}$$

taking into account the heat flow into both contacts and phonon mode degeneracy factor 2, with ς the Riemann zeta function. Note that this expression contains no free parameters. We rewrite eq. (II-6) as $P_{ph} \approx 2M\kappa_Q T$, analogous to the well-known Landauer formula for the ballistic conduction of electrons. Here $M \approx 1.5\pi k_B T R^2 / hac$, corresponding to the characteristic number of occupied phonon branches, and $\kappa_Q = p^2 k_B^2 T / 3h$ is the thermal conductance quantum [10, 11].

Plotting P versus M for samples shorter than ~ 0.5 μm should thus yield a straight line with a slope of $2T_B\kappa_Q$. Figure II-13 shows such a plot (M axis, upper scale) with $T = T_B$ = 900K for tubes with $L \le 0.5\,\mu\mathrm{m}$. The data closely follow a straight line with a fitted slope of 1.0 μW/branch. From this, we infer a value for the thermal conductance quantum of 6×10^{-10} W/K. This is the key experimental finding of this work. Although the accuracy of this measured value of κ_Q is somewhat limited by the uncertainty in T_B and the assumptions of our model, our experimental determination of κ_Q is nevertheless in good quantitative agreement to the theoretical value $\kappa_Q = 9 \times 10^{-10}$ W/K. This demonstrates that we readily reach quantum mechanical limits to thermal transport in our

nanotube devices that act as ballistic phonon waveguides. This is the first such observation for a nanostructure under ambient conditions, enabled by the unique thermal properties of carbon nanotubes.

II-10 Phonon Mean-Free Path

From our model and the data of Figure II-12, we also obtain an estimate for the phonon mean-free path, which was not determined in ref. [18]. Since the thermal conductance in the diffusive limit may be written as $K = \lambda M \kappa_Q / L$, where λ is the phonon mean-free path, we can obtain an interpolated expression for the power, appropriate to T = 900 K, that agrees with the asymptotic limits discussed earlier, $P_{\text{int}} = 2M\kappa_Q L^{-1} / (L^{-1} + 3/8\lambda)$. The dashed line is a fit of $P_{\text{int}} / 8\pi R^2$ to the data of Figure II-12 with λ = 220 nm, yielding a satisfactory fit to the data over the entire length range with only a single free parameter.

II-11 Electrical Breakdown Mechanism

Our data yields insight into the breakdown process. The well-defined breakdown temperature suggests it requires an initial defect-forming step with activation energy. The bond breaking process is very similar to the rate of diffusion in solids, which is mainly affected by the presence of defects. As an atom diffuses through a crystal, it must overcome a series of energy barriers presented by its neighbors as it moves from lattice site to lattice site or from interstitial position to interstitial position. In the electrical breakdown scenario, it involves a sequence of C-C bond breaking. Since the breakdown process is under an inert environment (such as Argon), extra bond-forming chemical reactions should not be involved. Let us consider interstitial diffusion of impurities. If this barrier height is Δ, then $\exp(-\Delta / k_B T)$ can be thought of as the fraction of time that vibrating bond will have an energy exceeding ε to disassociate. If ω_A is the characteristic attempt frequency then the probability per unit time that bond will be able to pass over the barrier is $p \sim \omega_A \, e^{-\Delta / k_B T}$. The defect formation rate is $\Gamma \sim$

$N\omega_A \exp(-\Delta / k_B T_B)$, where N is the number of atoms in the tube at temperature T_B ~ 900K. We find Δ ~ 3–4V with Γ ~1 s^{-1}, a range of ω_A ~ 10^8–10^{18} s^{-1} and N ~ 10^6, highly insensitivity to the choice of N and ω_A.

One possible origin for Δ is the formation of a Stone-Wales defect. This defect formation is about the rotation of a *C*-*C* bond in graphite. However, the estimated Δ from our data is considerably smaller than the theoretically determined barrier ~ 10 eV to from a Stone-Wales defect in graphite and MWNT [34], ruling out this possible mechanism.

Another, more likely, scenario follows from STM experiments where nanotubes were cut with voltage pulses, showing a well-defined cutting threshold voltage ~ 3.8 V [35]. This was interpreted as the signature of an electronic excitation from a σ to π^* state in the nanotube by the tunneling electrons [36]. Such transitions produce a local weakening of the carbon-carbon bonds in graphite, with a characteristic energy cost of $E_{\sigma-\pi^*}$ ~ 3.6 eV (see, e.g., ref. [33]), close to our estimated ~ 3–4 eV. This suggests that in our experiments the available thermal energy provides the energy $E_{\sigma-\pi^*}$. Combined with the electrical stress of carrying a current density > 10^{12} A/cm^2, which would readily break metal wire by electromigration, these σ to π^* transitions cause defect formation and a dissipation cascade that ablates the nanotube shell.

Finally, we are able to improve nanotube device conductance considerably using the electric current flow. Freestanding samples with initial low-bias resistance of 50 kΩ up to 10 MΩ typically show a rapid increase in conductance as the voltage across the sample is ramped, such as shown in Figure II-14. At higher voltages, a cascade of shell ablation begins and the current decreases in a stepwise fashion. The inset shows that the rise in conductance occurs in a smooth fashion. This behavior may be related to the structural annealing recently imaged by TEM [15].

Further experiments, however, are necessary to fully clarify the origins of this behavior, which is of practical value in addressing the challenge of obtaining a high yield of conductive nanotube devices.

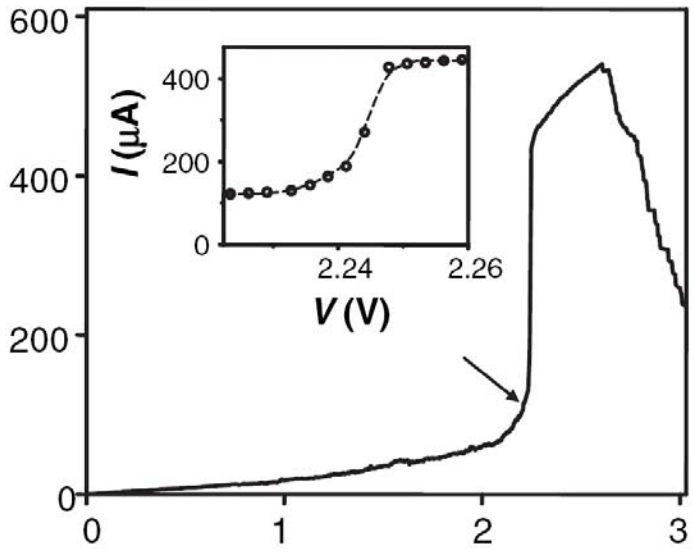

Figure II-14. I-V characteristic of a freestanding nanotube device with R = 14 nm. The arrow indicates a dramatic current increase. Inset: expanded view of data in the rapid-increase region

Chapter III

Atomic-Scale Mass Sensing Using Carbon Nanotube Resonators[37]

III-1 Abstract

Ultra-miniaturized mass spectrometers are highly sought-after tools, with numerous applications in areas such as environmental protection, exploration, and drug development. We have developed, in a nanoelectromechanical system (NEMS), the capability of weighing atoms by using doubly clamped suspended carbon nanotube electromechanical resonators, in which their single-electron transistor properties allow self-detection of the nanotube vibration. We also demonstrated that mass sensitivity has been greatly increased by two orders of magnitude over previous experiments based on the nanowire mass sensors [38]. As a consequence of the atomic-scale sensitivity, we were also able to observe atomic shot noise from the arriving atoms landing on random positions along the nanotubes, enabling us to quantitatively determine the mass of the nanotubes themselves as well as the atomic mass of adsorbing species.

Carbon nanotube mass sensors may have an advantage in detecting bio-materials, i.e. DNA or proteins, since this system is quite different from the traditional mass spectroscopy, which requires ionizing the neutral species and can potentially damage the samples. Furthermore, this highly sensitive mass detection capability may eventually enable applications such as on-chip detection, analysis, and identification of chemical compounds. There remains plenty of room for improvement, potentially enabling chemical or isotopic identification, and applications such as ultra-miniaturized mass spectrometry on a chip.

III-2 Introduction

Nanoelectromechanical systems (NEMS), which comprise of electromechanical devices, are designed to sense, process, or control the surrounding environment. The NEMS technology is the next step forward from the microelectromechanical systems (MEMS), which have been successfully applied in various contemporary technologies— e.g. airbag accelerometer sensors which are small integrated circuits with micromechanical components that respond to rapid deceleration. From an economic point of view, the nano-integrated systems can potentially achieve lower cost, lower power consumption, and greater miniaturization with better performance than their MEMS counterparts, because of improved sensing capabilities derived from nanoscale mechanical features.

In this chapter, we describe the operating principles, fabrication processes and low temperature measurement of our carbon nanotube mechanical resonators. Nanotube resonators draw mass sensing advantages from their remarkably high Young's modulus and light structure, coupled with their capability to act as single-electron transistors. The aforementioned properties help to increase the mass sensitivity by two orders of magnitude over the previously demonstrated mass sensors based on nanowires.

In addition, there are various other potential applications in NEMS. For example, they are one of the candidates to directly probe the fundamental quantum phenomena, such as zero-point quantum fluctuations in the displacement of a mesoscopic system [39]. Furthermore, the ultrahigh force sensitivity of NEMS devices has the potential to directly sense the Casimir force, which has recently become an important topic in NEMS-based devices [40]. Therefore, these electromechanical systems not only can lead to many prospective applications, but also provide the opportunity to bring a mesoscopic system into quantum regime, which might help us to bridge the conceptual gap between the probability wave description of microscopic objects and the apparent certainties of macroscopic world.

III-3 Device Fabrication

We adopt a doubly clamped suspended carbon nanotube structure as our mechanical resonator. Source and drain electrodes are attached to the nanotubes, and a third electrode is placed in close proximity to the suspended nanotube acting as a side gate. Note that the side gate provides the capability for tuning the nanotube electronic potential, as well as controlling the electrostatic force between nanotube and side gate.

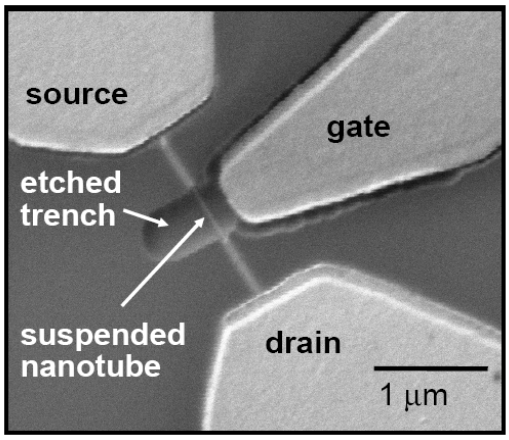

Figure III-1. SEM image of SWNT resonator. Device geometry of a representative suspended nanotube device with source, drain, and gate electrodes

The method of making a carbon nanotube resonator can be summarized in three steps. The first step is the chemical vapor deposition (CVD) growth of carbon nanotubes, the second step is the electrode contact fabrication, which involves electron-beam lithography and metal deposition, and the last step is the suspension of nanotubes by oxide etch. Each process still has room for improvement, and this section covers the best of our knowledge to date.

An SEM image of a typical carbon nanotube tri-electrode device is shown in Figure III-1. The central segment of the nanotube is suspended over the etched trench, and the supported sections of the nanotube are strongly anchored by the van der Waals force to the substrate with high binding energies [22, 41]. These carbon nanotube devices are

specially designed to meet the operational requirements at cryogenic temperatures and at very high frequencies, ranging from 100 MHz to several GHz. A metallic close-proximity side gate is made to improve the mobility of charge carriers driven at high frequencies and also to enhance the electrostatic coupling between the carbon nanotube and the side-gate electrode. Generally speaking at low-temperatures, the heavily doped silicon substrate that operated as the back gate is sufficient to couple to the device in the DC regime, but *not* in the high frequency regime. The distance between the metallic side gate and nanotube is typically kept around 100–150 nm for the strongest possible coupling without breaking the nanotube. If the side gate is too close to the nanotube, there is a higher chance that the nanotubes can stick to the side gate and cause a short circuit. Starting with light inertial mass and high resonant frequency necessitates as short a suspended nanotube segment as possible. The minimum length of the suspended nanotubes comes out to be about 400 nm, limited by that the etch process both affects the resist poly(methyl methacrylate) (PMMA) mask and silicon oxides.

III-3-1 SWNTs CVD Growth

In order to achieve a sufficiently large density of nanotube growth without forming carbon nanotube network which can produce short circuits or gate leakage, we adopted the method of catalyst islands [42] to define the coverage of catalysts. In addition, we made a major improvement by combining the alignment markers with catalyst islands. This simplification can avoid unnecessary contaminations during sample fabrication and results in good electrical contact.

Alignment markers are patterned by electron beam lithography (EBL) and formed by depositing about 15 nm of Cr followed by 180 nm of Au deposition. The exceptionally thick gold layer is to sustain the metal deformation during the nanotube growth at 900°C and to remain decipherable for the following EBLs of contact fabricating and PMMA etch-window patterning.

The following schematic diagrams show the step-by-step processes for the alignment markers fabrication and the catalyst islands deposition.

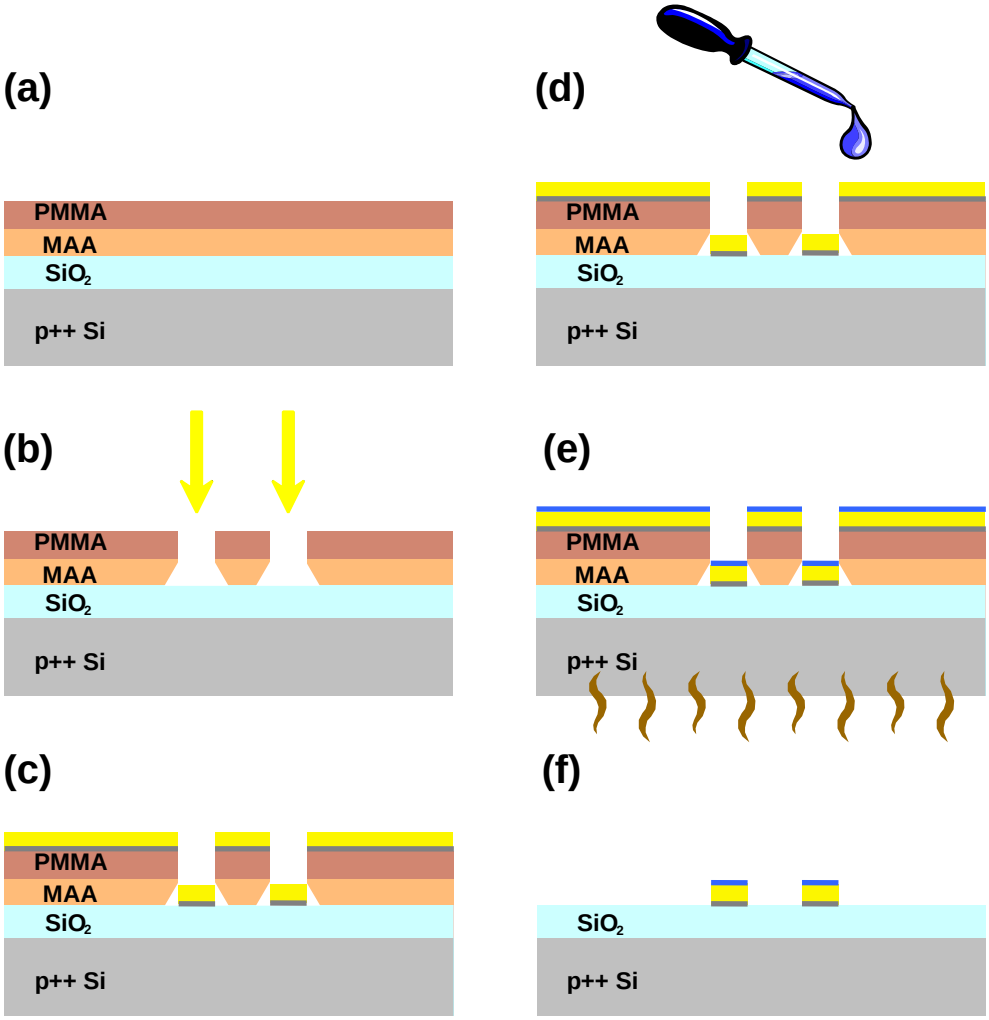

Figure III-2. Electron beam lithography for alignment markers and catalyst islands. (a) PMMA/MAA bi-layer of positive resist is spun on the substrate. (b) An electron beam exposes the defined area and the sample is developed to create a window. (The undercut of MAA layer will make the lift-off process (f) easier.) (c) Au/Cr metals are evaporated onto the surface of substrate through the windows. (d) Deposit catalyst solution everywhere. (e) A quick baking process. (f) Lift-off of the remaining resist and catalyst stay on the alignment markers

The nanotubes were first grown by CVD on degenerately p-doped boron silicon wafers capped with 300 nm or 1 μm thermally grown oxide.

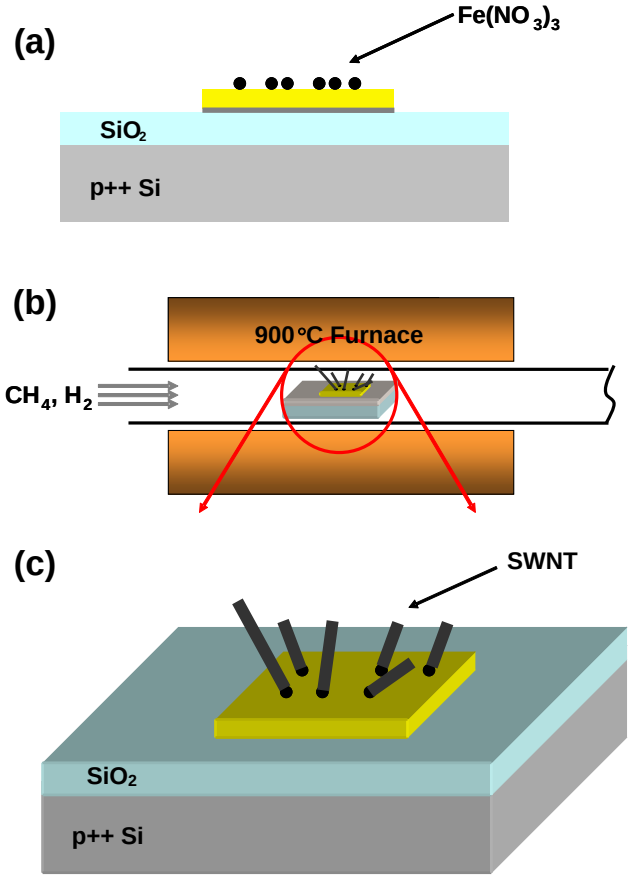

Figure III-3. Carbon nanotube CVD growth from catalyst islands. (a) Cross-section view of silicon wafer and predefined metal pattern with exaggerated catalyst particles on surface. (b) During a high temperature chemical reaction process. (c) A zoom-in image from (b), shows grown SWNTs only from the predefined metal pattern.

The catalyst solution consists of 40 mg of iron(III) nitrate nonahydrate $Fe(NO_3)_3 \cdot 9H_2O$ (Sigma-Aldrich), 2 mg of Molybdenum Acetate $MoO_2(acac)_2$ (Sigma-Aldrich), and 30 mg of alumina nanorods (Sigma-Aldrich) mixed in 30 ml of methanol. The size of the iron nanoparticles determines the diameters of the SWNTs. The advantage of using alumina nanorods is to prevent the iron nanoparticles from thermally drifting around during the high-temperature tube growth and to create more nanotube nucleation sites by having higher alumina surface area. The role of $MoO_2(acac)_2$ in nanotube growth is still not fully understood. However it has been suggested that the metal salt is

decomposed during heating in the CVD process to form Fe–Mo nanoparticles with diameters small enough to grow SWNTs [43].

After the catalyst solution is sonicated for an hour, a full drop of catalyst solution is deposited onto the prebaked silicon wafer with defined metal alignment marker openings in the PMMA resist and then dried on a hot plate. The remaining resist and metal are lifted off by immersing the sample in acetone for an hour without stirring. In addition we use a hot plate to maintain the temperature of acetone. This can help to maintain a constant nanotube growth density despite seasonal or daily temperature fluctuations.

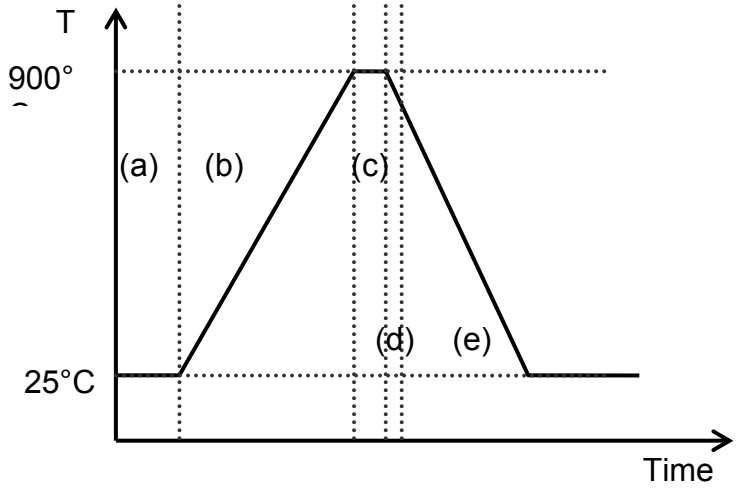

Figure III-4. The temporal diagram of nanotube growth processes. (a)–(e) are the processes in different composition of gas rates.

Step	Interval	Gas composition	
(a)	2 min	Ar	1000 sccm
(b)	25 min	Ar	250 sccm
		H_2	400 sccm
(c)	5 min	H_2	700 sccm
		CH_4	520 sccm
(d)	2 min	Ar	2000 sccm
(e)	15 min	Ar	400 sccm

Table III-1 Tube growth parameters corresponding to the processes in Figure III-4

After the lift-off, the sample with patterned catalyst islands (right on the metallized alignment markers) is placed in a 1 inch quartz tube furnace and the CVD is effectuated at 900°C with 700 sccm H_2, 520 sccm CH_4 for 5 min. Argon and hydrogen are flown during heating up and cooling down to prevent any chemical reactions during these phases. This recipe of methane and hydrogen flow rates has been optimized to obtain long and clean nanotubes (~ 10 μm) without amorphous carbon deposition [44].

There are five tube growth steps: (a) flush the quartz tube by large flowing argon rate, (b) ramp up to the desired tube growth temperature, (c) allow the actual tube growth process, and (d) terminate tube growth by running a huge amount of argon through to flush the remaining hydrogen and methane. In addition, this large flow rate of argon can align nanotubes right after growth. Finally, (e) is the cooling process; the presence of flowing argon prevents oxidation at high temperature.

III-3-2 Characterization of SWNT Diameters

A general question that arises when a tube growth recipe is altered or carbon nanotubes are provided from other sources is whether we have clean and single-walled nanotube samples. The most reliable way to examine the growth outcome is by taking transmission electron microscope (TEM) images. Figure III-5 is a TEM image that clearly shows one single-walled carbon nanotube among many grown nanotubes with very little amorphous carbon contamination. However, this procedure requires special sample preparation to grow the nanotube on an AFM tip, followed by a careful examination of protruded nanotubes from the edges of the tip.

An alternative method to examine this material is to use atomic force microscopy (AFM). However SWNT diameter is usually smaller than 3 nm, the measurement of nanotube diameter can vary with different AFM tips, due to the different sharpness of the tips. As a result, AFM can provide a general idea of nanotube diameter, but it cannot precisely determine the number of shells of nanotubes.

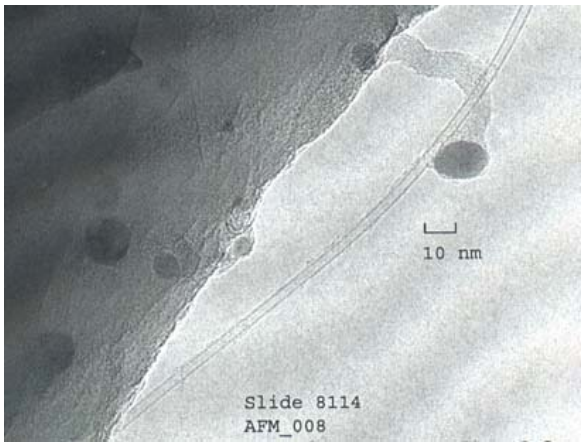

Figure III-5. Transmission Electron Microscope (TEM) image of our CVD-grown single-walled carbon nanotubes

There is yet another method to obtain the information of shell counts from electrical transport measurement. According to previous high-biased saturation and breakdown current studies [19, 24], measuring the breakdown current can accurately determine the numbers of shells of a MWNT nanotube. Literature shows that every single shell has a limited current capacity, limited by the optical phonon scattering to be ~25 μA, independent of the length of nanotubes. Additional discussion can be found in the Chapter II.

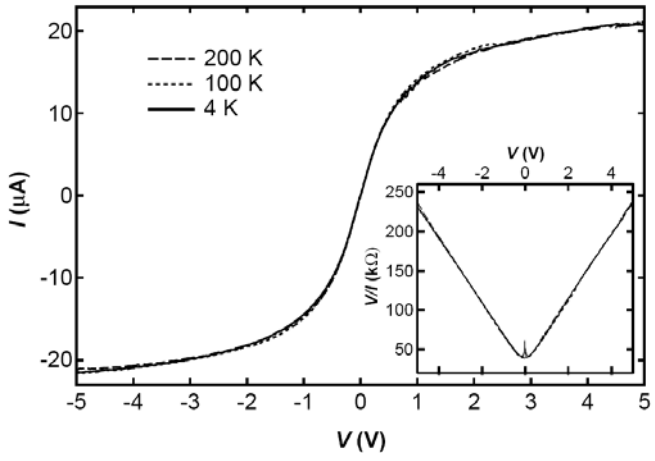

Figure III-6. HIgh-bias I-V characteristics of a substrate-supported SWNT. The saturation current is about 25 μA, independent of the length of nanotubes.

III-3-3 Electron Beam Lithography

After nanotube growth, an AFM or SEM image is necessary to locate the nanotube positions relative to the predefined alignment markers. A CAD layout is made accordingly for the electrodes to make contact to the two ends of nanotubes, and a metallic close-proximity side gate which is extended to the bonding pads. In order to have strong coupling between the nanotube and the side-gate electrode, the distance between them is designed to be ~ 120 nm. This gives a pronounced resonant response. We can then use either of the following methods to locate the nanotubes

1. Electrostatic Force Microscope (EFM)

Generally, nanotubes are located relative to the alignment marks using an atomic force microscope (AFM) and this is the most time-consuming step in fabricating SWNT devices. To obtain a good-quality image, AFM is practical only for a small scanned area (~ 10×10 μm^2). However, the total area of the alignment markers is large ($76\times76\,\mu m^2$), and the diameters of the SWNTs are very small (~ 1–3 nm). In order to locate SWNTs within the whole pattern of alignment markers, we need a better technique. We find electrostatic force microscopy (EFM) well suited for this application. During an EFM scan, a topographical line scan is acquired first, followed by a second pass at a constant height above the surface with a constant applied tip voltage. This technique can resolve SWNTs in a large region due to the long range nature of the electrostatic force (Coulomb interaction). Figure III-7 is a sample EFM image of SWNTs. On the whole, EFM scanning is still time consuming, and the electrostatic force may damage nanotubes. The resulting defects can be seen especially at low temperatures. In addition, the image quality of the alignment markers is generally poor, which limits the accuracy in the following sample fabrication process.

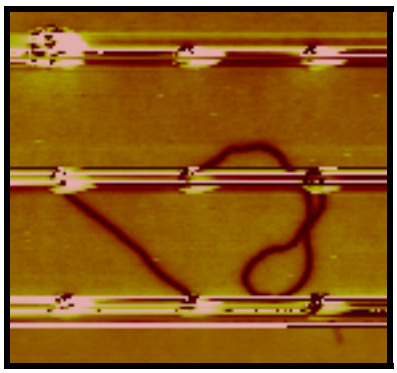

Figure III-7. EFM image of single-walled carbon nanotubes. The red lines are SWNT and the bumpy structures are the predefined alignment markers.

2. Scanning Electron Microscope (SEM)

Overall, we find that SEM is the most useful tool because it provides a quick and clear image process. To attain better image contrast of the SWNTs on silicon oxide (non-conducting substrate) requires critically low accelerating voltages of ~1 kV, for minimizing the negative charging of the substrate. Moreover, at higher accelerating voltages, the electron beam penetrates deeper into the oxide, producing fewer secondary electrons that sense the surface potential differences [45], which is undesirable.

A disadvantage of using SEM for imaging is that the specimen gets contaminated by amorphous carbon [46]. In order to keep the device clean from after imaging, baking the sample in a constant oxygen flow rate inside a furnace at 300°C for 30 min is recommended before the next fabrication step. We have examined the outcome by using AFM to compared the before and after images. This oxygen cleaning method is proven to remove organic residues. Nevertheless, we cannot rule out any soot grown along nanotubes because it is not observable by AFM,

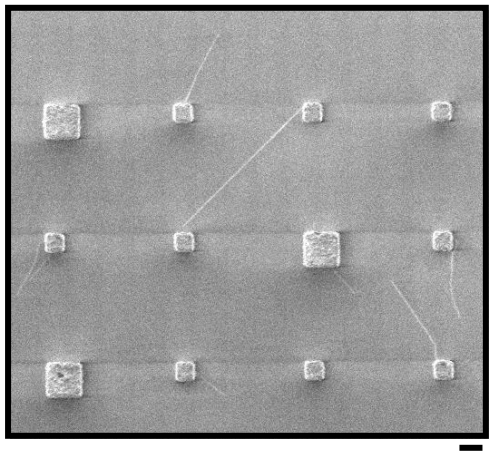

Figure III-8. A SEM image of pristine single-walled carbon nanotubes and alignment markers (only partial pattern shown). These supposed-to-be-square alignment markers are slightly deformed during tube growth. Scale bar indicates as 1 μm.

The following schematic diagram is the fabrication flow chart.

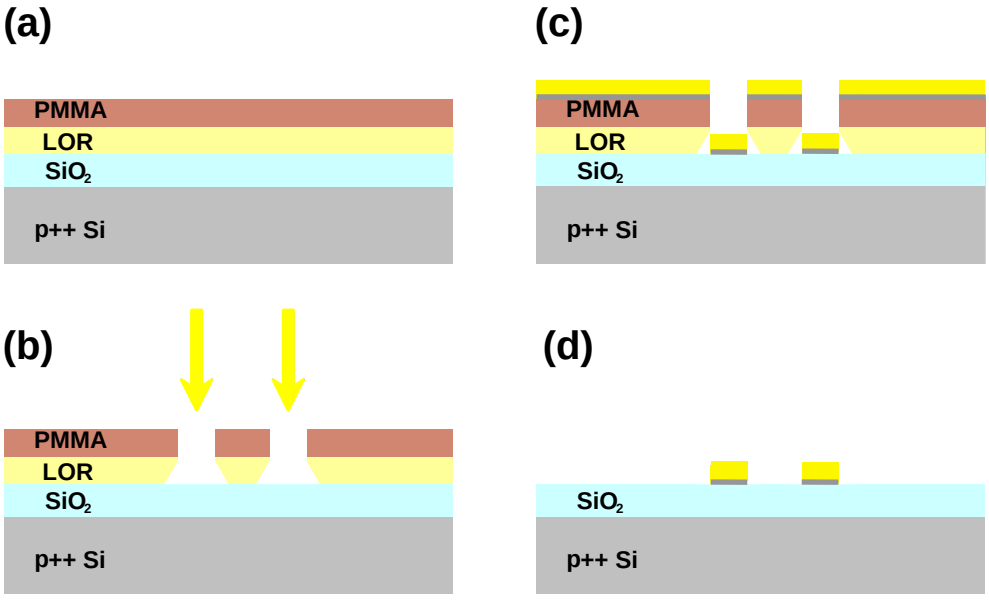

Figure III-9. Electron beam lithography for contact electrodes (a) PMMA/LOR bi-layer of resist is spun on the substrate. (b) An electron beam exposes the defined area and the sample is developed to make a window. (The LOR layer, is not affected by either electron beam or ultraviolet light, it has a large undercut, which makes lift-off process (d) easier.) (c) Au/Pd metals are evaporated onto the surface of substrate through the windows. (d) Lift-off of the remaining resist

In the second EBL process of patterning the electrode contacts, thin layers of palladium (15 nm) and gold (40 nm) metals are thermally deposited right after developing the PMMA and lift-off resist (LOR) layers. Palladium has been shown to be the best ohmic contact to carbon nanotubes [47]. Since palladium thin films are hydrophilic, once the thin film makes contact with any aqueous solution, the film would be stripped into small fragments immediately. Therefore, a gold layer is deposited on top of palladium to suppress this peeling behavior. Furthermore, we need a suitable resist and nonaqueous developer to work with the palladium contacts. The applicable chemical we found is MicroChem LOR 3B and PG-Remover (nonaqueous). The advantage of using LOR 3B resist is to greatly reduce the contact resistance because it leaves mush less residue than any other resists we've tested.

We examined the palladium contacts with sub-micron on-substrate SWNTs. The electrical conductance obtained in a two-point measurement at room temperature can sometimes be very close to the expected quantum conductance $G = 4e^2/h \approx (6.45\text{k}\Omega)^{-1}$ of a 1D quantum wire such as a SWNT. The factor 4 in the equation of conductance comes from two independent conducting spin-degenerate channels in SWNTs. For such nanotube devices, the low contact resistance gives them an open dot behavior, yielding Fabry-Perot interference in a nanotube electron waveguide. Detailed discussion concerning the quantum dot physics can be found in Section I-5.

III-3-4 Suspend Carbon Nanotubes

After contact fabrication, the final step is to suspend the carbon nanotubes using wet-etch. The major obstacle to overcome in this suspending process is the surface tension of the processing solutions. At the microscale or nanoscale, the ratio of surface to volume increases, inverse-proportional to the dimension of the device. Therefore, the surface tension dominates other forces when the scale is smaller than a few microns. Figure III-10 illustrates how surface tension affects the nanostructure during the evaporation of a liquid drop.

The wet etching is performed in buffered oxide etch (BOE, aqueous NH_4-HF etchant solutions) with gentle agitation followed by a rinse in solvents. We often chose isopropyl alcohol (IPA) or methanol as the final rinse solution because these solutions have smaller less surface tension than water (72.8 mN/m at 25°C).

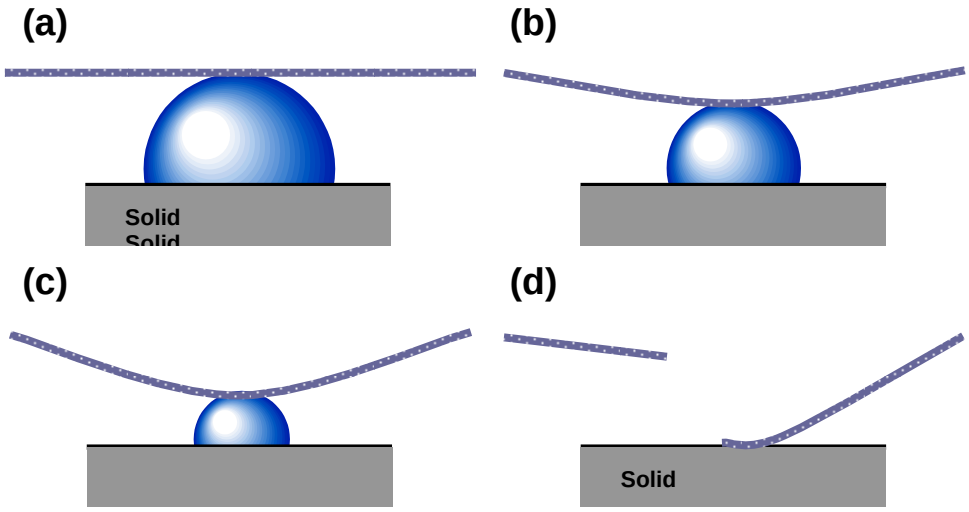

Figure III-10. Schematic diagram of surface tension in micron scale. (a) The diameter of droplet is right to match the height of the beam. (b) When the droplet gets smaller, the surface tension pulls the beam downwards. (c) The more the droplet shrinks the more the beam stretches and deforms. (d) The beam might break or go through plastic deformation, depending on the aspect ratio of the beam and the distance between beam and solid surface. In the diagram, a half beam adheres to the solid surface due to the van der Waals force.

The following are two schemes to produce the suspended segment of nanotubes:

1. Metal Electrodes as the Etch Mask

Using metal electrodes as the etch mask is the simplest choice to suspend CNTs: we can directly place the sample in BOE to etch away the substrate. If the suspended segment is less than 500 nm for a SWNTs device, or if the aspect ratio of MWNTs is small, there are two quick ways to dry the samples. First option: we take the sample out directly from isopropyl alcohol (IPA), the final rinse solution, and bake the sample on a preheated hotplate (~ 50°C), letting it naturally dry. Second option: we can heat up methanol with the sample inside and take the sample out from the beaker while the methanol is boiling.

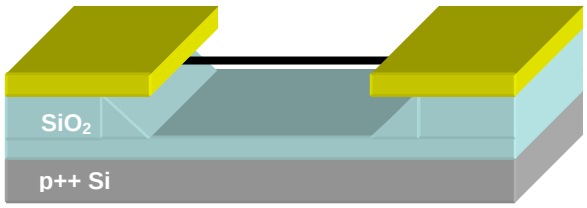

Figure III-11. Schematic diagram of metal electrodes as the etch mask. There is always an undercut after etching.

In order to create ~ 400 nm SWNT devices with a metallic close-proximity side gate, it is difficult to use the metal electrodes as the etch masks, especially considering the side gate has to be wide and close enough to the nanotube to enhance the electrostatic coupling effect. Therefore, the third EBL has been processed to make the etch window from PMMA.

2. PMMA as the Etch Mask

After appling a layer of PMMA, a third EBL is performed to open small windows in the middle of nanotubes. Here the separation of source and drain electrodes can be further apart (~ 1 μm), such that the side-gate electrode can be placed at a close distance yet with wide enough coverage to have strong electrostatic coupling. Following the etch process in BOE, we rinse the sample with DI water and lift off the PMMA resist in acetone. Afterward, care has to be taken to soak the sample in IPA and transfer the sample to a critical point dryer.

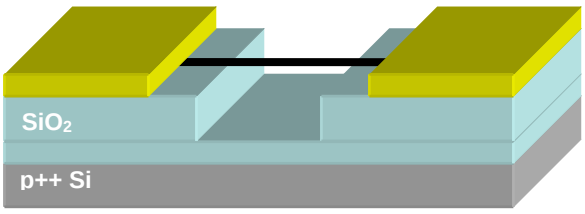

Figure III-12. Schematic diagram of suspended structure, etched through the PMMA window which is patterned by the third EBL

The minimum window width after etching is ~ 400 nm, although initially only a very small line width (~ 20 nm) of PMMA is exposed during EBL. This line width is limited by the resolution of the convertible e-beam writer (FEI Quanta 200 FESEM). During the

etch process, both the PMMA resist and silicon oxide are etched, producing a broadened trench.

A critical point drying (CPD) exploits the phenomenon known as the continuity of state, where there is no apparent difference between the liquid and gas states of a medium above its critical point, reducing the surface tension at this interface to zero. The most common and convenient transitional medium for critical point drying is carbon dioxide (CO_2), which has a critical point at 31°C and 73.0 atm. Although it might not be necessary to run a CPD process for a submicron-suspended device, it is essential for making a close-proximity side gate located ~100 nm from the suspended nanotube. The yield of CPD is much higher than other methods, and thus it provides significant improvement for our sample fabrication.

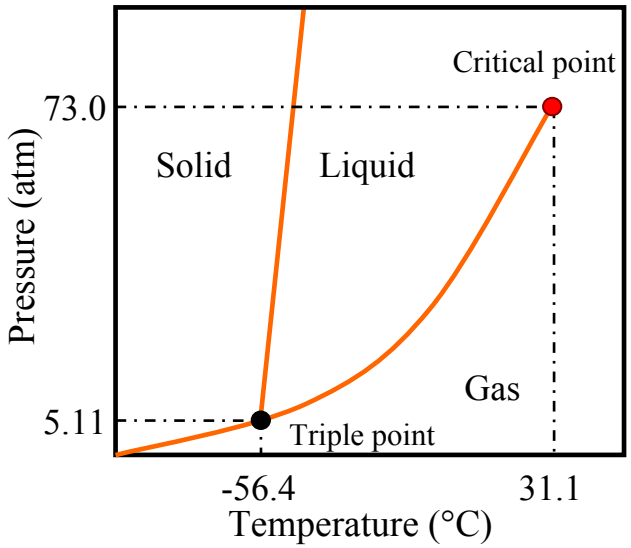

Figure III-13. The phase diagram of carbon dioxide

III-4 Basis of Elastic Beam Theory

For the purpose of understanding the range of expected resonant frequencies of carbon nanotube resonators (from fundamental mode to higher excited modes), it is necessary to examine a system at the physical level of device modeling and analysis. In this section we will start with a structural mechanics including elasticity and elementary structure, and

will subsequently elucidate an energy-based method to describe our SWNT resonator devices, which is a practical means to address our complicated system that involves both mechanical and electrostatic energy contributions.

However, before we proceed to the theoretical groundwork, we have to consider the factors that may arise in a realistic device. Our system is more complicated than a simple bending beam, since we apply a considerable amount of electrostatic force on nanotube by applying DC voltage through the side gate. There is typically some degree of slack (excess length between electrodes, e.g., Figure III-14 (a)) built in a suspended nanotube during the fabrication process, especially from the tube growth. The first factor hardens the resonant modes by increasing electrostatic force. However, the second factor softens the resonant mode and generates an additional dynamic motion, called the "jump-rope" mode shown in Figure III-14 (b). Beyond these two external factors, the aspect ratio of the beam is one intrinsic factor. We can discard this cause by reason of the fact that our nanotube aspect ratio is ≥ 200.

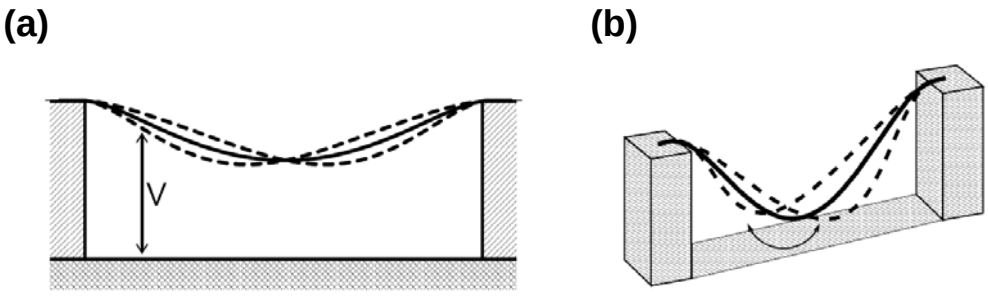

Figure III-14 A suspended nanotube with slack: (a) under the action of a gate voltage V, (b) the "jump-rope" mode [48]

In our case, the device lengths is about ~ 400–500 nm where the empirical slack is quite small. Particularly when a large DC side-gate voltage is present, the electrostatic force can reduce the effects of an initial slack. This is very different from those reported nanotube resonator devices from a few groups [49-51] having 1–2 μm of nanotubes with large slacks, which reduce the resonant frequencies significantly. Figure III-15 categorizes three regimes of nanotube behavior [48] based on the initial slack and gate voltage. These regimes are the buckled beam, hanging chain, and hanging spring. We

find our nanotube resonators typically falling into the hanging spring regime, hence we often take the stretched string (analogous to a guitar string) as the simplest model for analysis.

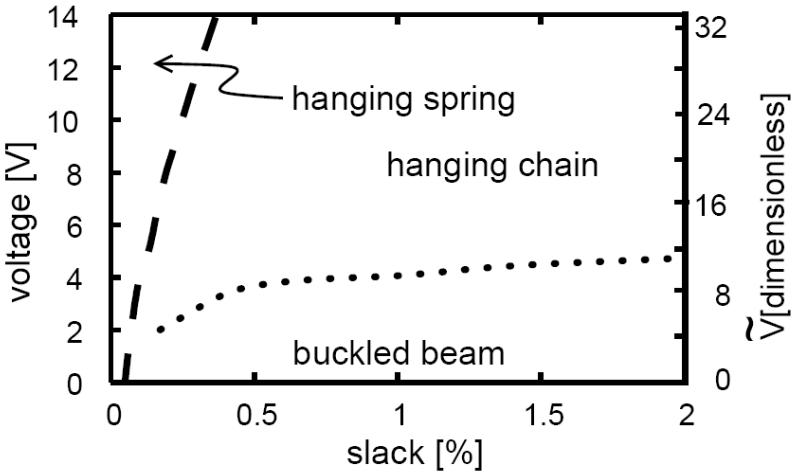

Figure III-15. The three regimes in which nanotube behavior simplifies, as a function of voltage and slack [48]

After understanding the issues of slack and the aspect ratio, we only consider the possible residual stress and the electrostatic force between nanotube and gate electrode in the subsequent discussions. Given that there are two chapters in this thesis covering two different nanoelectromechanical systems, it is worth to address the fundamental properties of related beam theory.

III-4-1 Bending of Beams

An overview of elastic beam theory in the differential element is adopted in this section. First, starting with the differential beam element of Figure III-16, we have three types of loads to consider: external transverse loads q (which conventionally denoted the force per unit length), shear forces V ($V+dV$) parallel to the lateral loading, and rotational moments M ($M+dM$).

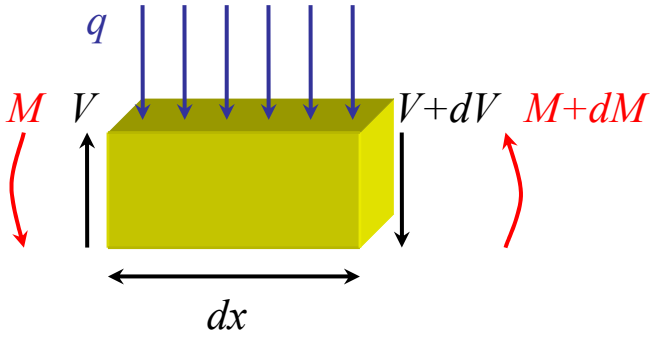

Figure III-16. A fully loaded differential beam element of length *dx* with moments and shear forces

Applying the constraint of total static equilibrium (zero force and zero rotational moment) to this differential element; we obtain the differential relations among the different loads. The total force F_{net} on the differential element is

$$F_{net} = q\,dx + (V + dV) - V\ .$$

Based on the constraint of the zero net force, we can get

$$\frac{dV}{dx} = -q\ . \tag{III-1}$$

The net rotational moment M_{net} acting on the differential element with respect to the left-hand edge is

$$M_{net} = (M + dM) - M - (V + dV)dx - \frac{q\,dx}{2}dx\ .$$

If we neglect this $(dx)^2$ term, it yields

$$\frac{dM}{dx} \cong V\ . \tag{III-2}$$

Combining eqs. (III-1) and (III-2), we can obtain

$$\frac{d^2M}{dx^2} = -q\,. \tag{III-3}$$

These relations are the keys for solving elastic systems, later we will use them to establish the differential equations governing the bending of beams.

Now we consider a bending-type deformation that results the transverse loading of beams. Figure III-17 shows the small section of a beam that has been bent in response to the application of transverse loads. The dashed arc in the middle of the beam is called the neutral axis, the entire length of which is unchanged during bending. The material above the neutral axis is in a state of tension, while the material below the neutral axis is in compression. The radius of the bending curvature is defined as ρ, and the *external* applied moment is denoted by M_0.

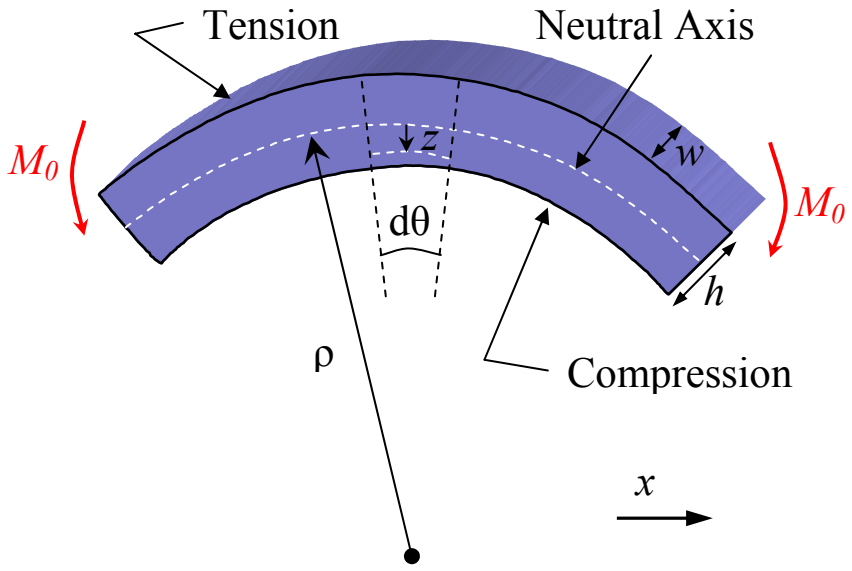

Figure III-17. A segment of a beam in pure bending; vertical displacements and angles are greatly exaggerated. Note the positive direction of z is downward in this figure.

The length of the dashed segment at position z is

$$dL = (\rho - z)d\theta \,. \tag{III-4}$$

At the position of neutral axis, the length of the corresponding segment is

$$dx = \rho \, d\theta \,. \tag{III-5}$$

From eqs. (III-4) and (III-5), an axial stress in the beam segment is

$$\sigma_x = E\varepsilon_x = E\frac{dL - dx}{dx} = -\frac{zE}{\rho} \,. \tag{III-6}$$

In eq. (III-6), we have assumed the beam is isotropic, that the normal stress in the x direction σ_x is linearly related to the uniaxial strain in the x direction ε_x, thus $\sigma_x = E\varepsilon_x$. The proportionality constant is called Young's modulus and it is denoted by E.

This structure has a distribution of internal stresses, we can find the total *internal* bending moment M by calculating the first moment of distributed internal stress.

$$M = \int_{-h/2}^{h/2} \overbrace{\underbrace{wz}_{area} \cdot \sigma_x}^{force} dz = -\left[\int_{-h/2}^{h/2} w\, z^2 dz\right]\frac{E}{\rho} = -I_x \frac{E}{\rho} \tag{III-7}$$

where w is the width, h is the height, I_x is the beam cross-section moment of inertia about the neutral axis x, and z is the perpendicular distance to the neutral axis.

$$\frac{1}{\rho} = -\frac{M}{EI_x} \tag{III-8}$$

Since equilibrium requires that the total moment to be zero, the *external* M_0 that created it in the first place must equal $-M$. So we could equally write

$$\frac{1}{\rho} = \frac{M_0}{EI_x}. \qquad \text{(III-9)}$$

Hence we have the relation of the radius of curvature of the beam in terms of the externally applied bending moment, eq. (III-8) or internal bending moment, eq. (III-9).

For a circular cross section with radius R, the center of mass is at the center of the circle, and the principal axes are arbitrary. The moment of inertia about any axis lying in the cross-section and passing through the center is

$$I_x = \frac{1}{4}\pi R^4. \qquad \text{(III-10)}$$

For a SWNT, if we consider it as a hollow structure, the momentum of the inertia can be written as $I_x = \frac{1}{4}\pi[R^4 - (R-a)^4]$, where a is regarded as the interlayer spacing of graphite.

III-4-2 The Euler-Bernoulli Beam Theory

We consider a carbon nanotube as an example of a continuous system; its mass is distributed and inseparable from the elasticity of the nanotube. If the deflection of the nanotube $u(x,t)$ is assumed due to the bending moment only, and the aspect ratio of our nanotube devices are generally large, we can simply apply the Euler-Bernoulli beam model to our systems. However, in the case of a shorter carbon nanotube with small aspect ratios whose higher-order resonant frequencies fall within terahertz range. Hence, these nanotubes should be modeled as Timoshenko beams instead of Euler-Bernoulli beams, because the rotary inertia and shear deformation are more significant for higher-order modes of shorter elastic beams.

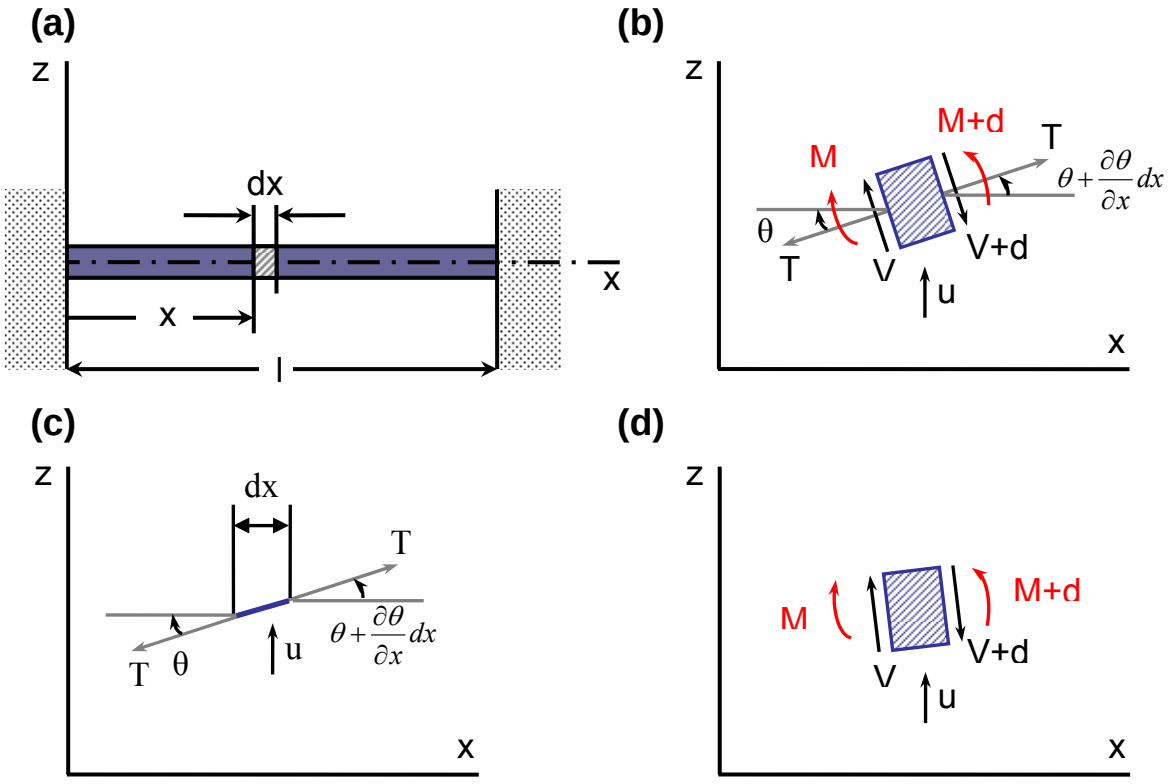

Figure III-18. Free-body sketches of an element of beam. (a) A schematic diagram of a doubly clamped beam. (b) A differential element *dx* with forces involved from (c) and (d). (c) The free-body sketch of an element *dx* of a string. (d) The free-body sketch of an element *dx* of a beam

Consider the free-body sketch of an element of beam (nanotube) shown in Figure III-18 (b). The tension is assumed constant for small deflections of the beam and the other effects are negligible. The forces involved are the spring problem in Figure III-18 (c) and the beam problem in Figure III-18(d). From Newton's second law, the dynamic force equation in the lateral direction is

$$\mu \frac{\partial^2 u}{\partial t^2} dx = -(V + \frac{\partial V}{\partial x} dx) + V + T(\theta + \frac{\partial \theta}{\partial x} dx) - T\theta$$

or

$$\mu \frac{\partial^2 u}{\partial t^2} = -\frac{\partial V}{\partial x} + T \frac{\partial^2 u}{\partial x^2} \qquad \text{(III-11)}$$

where μ is mass per unit length, $\theta = \partial u / \partial x$ = slope, and V the shear force. Summing the rotational moments (torques) of the differential element with respect to the right face yields

$$\frac{\partial M}{\partial x} dx - V dx \cong 0$$

or

$$\frac{\partial M}{\partial x} = V \,, \qquad \text{(III-12)}$$

and from the elementary strength of materials, the beam curvature and the moment M are related to

$$EI \frac{\partial^2 u}{\partial x^2} = M \qquad \text{(III-13)}$$

where EI_x is the flexural stiffness of the beam (nanotube). After substitutions, we obtain

$$\mu \frac{\partial^2 u}{\partial t^2} = -\frac{\partial^2}{\partial x^2}\left(EI \frac{\partial^2 u}{\partial x^2}\right) + T \frac{\partial^2 u}{\partial x^2} \qquad \text{(III-14)}$$

Eq. (III-14) is the equation including the effect of axial tension T. The sign of T is reversed if the beam is under compression.

Let us find the natural frequency of a uniform doubly clamped beam subjected to an axial tension T. Assume the existence of principal modes as $u(x,t) = \phi(x)\sin(\omega t + \psi)$.

Substituting $u(x,t)$ to (III-14) and simplifying, we get

$$EI\frac{\partial^4\phi}{\partial x^4} - T\frac{\partial^2\phi}{\partial x^2} - \mu\omega^2\phi = 0\,. \qquad \text{(III-15)}$$

Let the solution be $\phi = Ce^{sx}$, where C and s are constants. It can be shown the corresponding characteristic equation is

$$EIs^4 - Ts^2 - \mu\omega^2 = 0 \qquad \text{(III-16)}$$

or

$$s^4 - \xi^2 s^2 - \lambda^2 = 0 \qquad \text{(III-17)}$$

where $\lambda = \omega\sqrt{\frac{\mu}{EI_x}}$ and $\xi = \sqrt{\frac{T}{EI}}$.

The quadratic roots are

$$s_{1,2}^2 = \frac{1}{2}[\xi^2 \pm \sqrt{\xi^2 + 4\lambda^2}]\,. \qquad \text{(III-18)}$$

Which must be real and of opposite sign. Let $s_1^2 = a^2$ and $s_2^2 = -b^2$, or $s_2 = \pm ib$ where $i = \sqrt{-1}$. Hence the solution of the eq. (III-17) is

$$\phi(x) = C_1 \sinh ax + C_2 \cosh ax + C_3 \sin bx + C_4 \cos bx\,.$$

The boundary conditions of a fixed-fixed (doubly clamped) beam are

$$\phi\,|_{x=0} = \left.\frac{d\phi}{dx}\right|_{x=0} = \phi\,|_{x=L} = \left.\frac{d\phi}{dx}\right|_{x=L} = 0\,.$$

The above equation has a nonzero solution; this yields the following equation for the frequency ω:

$$\cosh(aL)\cos(bL) - \frac{1}{2}\frac{a^2 - b^2}{ab}\sinh(aL)\sin(bL) = 1$$

and the solution is the following with an arbitrary amplitude

$$\phi(x) = C_1[\sinh(ax) - \frac{a}{b}\sin(bx) + \frac{(\cos(bx) - \cosh(ax))(a\sin(bL) - b\sinh(aL))}{b(\cos(bL) - \cosh(aL))}].$$

In the following, we focus on the fundamental mode ω_0, in the limiting cases, the ω_0 are

$$\omega_0 = \sqrt{\frac{EI}{\mu}}\begin{cases} 22.38L^{-2} + 0.28\xi^2, & \xi L << 1 \\ \pi\xi L^{-1} + 2\pi L^{-2}, & \xi L >> 1. \end{cases} \qquad \text{(III-19)}$$

The frequency dependence $\omega_0 \propto L^{-2}$ is associated with a loose string, while $\omega_0 \propto L^{-1}$ means that the string is tied like a guitar.

When the axial tension is absent, $EIs^4 - \mu\omega^2 = 0$, we can find the displacement function is

$$\phi(x) = C_1[\sinh(\kappa x) - \sin(\kappa x) - \frac{(\cos(\kappa x) - \cosh(\kappa x))(\sin(\kappa L) - \sinh(\kappa L))}{\cos(\kappa L) - \cosh(\kappa L)}]$$

where $\kappa^2 = \lambda$, κL = 4.73004, 7.8532, 10.9956, 14.1372, which satisfy the condition

$$\cos(\kappa L)\cosh(\kappa L) = 1.$$

And the lowest natural frequency is $\omega_0 = \left(\frac{4.73004}{L}\right)^2\sqrt{\frac{EI}{\mu}}$.

For a SWNT with 1.3 nm in diameter and 500 nm in length, E = 1.2 TPa, $I = \frac{1}{64}\pi d^4$, and μ (mass per unit length) = $2.39204 \times d$ (nm) zg/nm.

We therefore obtain the resonant frequency $f_0 = \omega_0 / 2\pi \sim 100$ MHz in the pure bending and tension-free case.

The analysis of this section is based on the Euler-Bernoulli beam model with axial loading *T*, which works well for simple geometry and known tension. In fact, the tension in our system is not a directly measurable (controllable) quantity. Therefore, in the next section, we will go through the "Energy Methods", which can readily address a more complicated system involving multiple forces, i.e., the mechanical and electrostatic forces in our system. In other words, the resonant frequencies of our devices can be controlled by applying DC voltage through the side-gate electrode. Hence, we are able to link the actual gate voltage to tension in our system, and also the derivation shows that it is possible to observe the quantized frequency change in the quantum dot regime [52].

III-4-3 Energy Methods

The advantage of using the energy methods is that we can consider different types of energy stored in an energy-conserving system. The energy stored in a body (i.e., elastic material) due to the quasi-static action of surface and body forces is equal to the work done by these forces. We can formulate the stored energy as a function of the deformation of a mechanical object, then determine how an object responds to a force by determining the shape the object must take in order to minimize the difference *U* between the stored energy and the work done by the forces.

$$U = Stored\ \ Energy - Work\ \ done\ .$$

The carbon nanotube resonator system can be simplified as the following schematic diagram. A SWNT (modeled as a rod of length *L* along *x* axis) is freely suspended between source and drain electrodes, in the vicinity of a gate. The nanotube is attached to the electrodes via tunneling contacts and capacitances between nanotube and electrodes are denoted by C_L and C_R. An electrostatic force (gate voltage) bends the tube; the

deviation from a straight line is denoted by $z(x)$ with $0< x< L$. $c(z)$ is called the gate capacitance per unit length, which is varying along the nanotube.

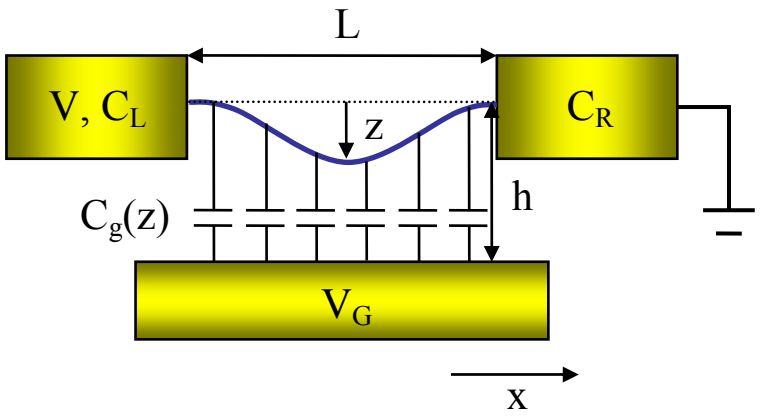

Figure III-19. A schematic diagram of a suspended nanotube capacitively coupled to a gate electrode

The entire energy stored in the above system is derived in the following discussions. As the nanotube is mechanically deformed by electrostatic forces, there are three types of energy contributions to consider: the elastic energy due to the bending (unstressed), the stress energy from stretching, and the electrostatic energy which is stored in the electrical capacitance between the nanotube and gate electrode.

Elastic Strain Energy

A beam made of an isotropic material is subjected to bending (refer to Figure III-18(a)). Consider a differential element of length *dx* and cross-section area *dS*.

Using the relations for bending from the previous section, we know the an axial stress from eq. (III-6) $\sigma_x = -zE/\rho$ and eq. (III-8) $1/\rho = -M/EI_x$

From eqs. (III-6) and (III-8), this element *dx* is subjected to a normal stress: $\sigma_x = Mz/I_x$.

The strain energy density on this element is $u = \frac{1}{2}\sigma_x \varepsilon_x$, for linear elastic material $u = \sigma_x^2 / 2E$, hence, the strain energy for a slice of the beam, of width *dx*, is

$$dU = \int_A u \cdot \underbrace{dxdS}_{\textbf{volume}} = \frac{M^2}{2EI_x^2} dx \underbrace{\left(\int_S z^2 dS\right)}_{I_x} = \frac{M^2}{2EI_x} dx .$$

Since the curvature $= \frac{1}{\rho} = \frac{\partial^2 z}{\partial x^2} = -\frac{M}{EI_x}$, the strain energy of a differential element is

$$dU = \frac{EI_x}{2}\left(\frac{\partial^2 z}{\partial x^2}\right)^2 dx = \frac{EI_x}{2} z''^2 dx .$$

Stress Energy

Consider the suspended nanotube system shown in Figure III-19 with the stress force $\widetilde{T} = T_0 + T$. Here, T_0 is the residual stress which is may result, e.g., from the fabrication, and induced stress T is due to the elongation of the tube caused by the gate voltage.

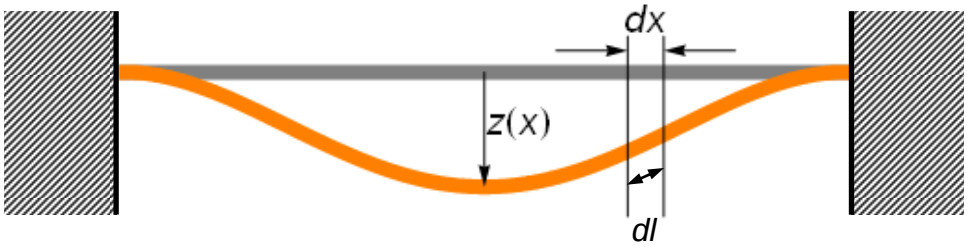

Figure III-20. A schematic diagram of a doubly clamped beam. A segment *dx* is defined along the original neutral axis and the segment of *dl* is used to show the deformation components.

To calculate the elongation component from the original natural segment,

$$dl = \sqrt{[z(x+dx)-z(x)]^2 + (dx)^2}$$
$$= dx\sqrt{1+[z'(x)\,dx]^2}$$
$$\approx dx + \frac{1}{2}dx[z'(x)\,dx]^2.$$

A Taylor expansion for small δ gives $\sqrt{1+\delta} \approx 1+\frac{1}{2}\delta$, so we can obtain the strain

$$\varepsilon_x = \frac{dl-dx}{dx} \approx \frac{z'(x)^2}{2}$$

$$\varepsilon_x = \frac{\sigma_x}{E} = \frac{T}{ES} \approx \frac{z'(x)^2}{2}$$

and integrating over the entire length of the nanotube,

$$\int_0^L \frac{T}{ES}dx \approx \int_0^L \frac{z'(x)^2}{2}dx$$

and the stress force T is

$$T \approx \frac{ES}{2L}\int_0^L z'(x)^2 dx.$$

Therefore, energy stored due to the external stress

$$dW = \frac{1}{2}T(dl-dx) \approx \frac{1}{4}T\,z'(x)^2\,dx.$$

The total energy stored including the external stress and residual stress

$$W \cong \int_0^L \left[\frac{T_0}{4} + \frac{ES}{8}\int_0^L z'(x)^2 dx\right] z'(x)^2 dx.$$

Elastic Energy + Stress Energy

Gathering the energy of an unstressed bend rod and the effect of the stress from $\widetilde{T} = T_0 + T$, we have

$$W_{el}[z(x)] = \int_0^L dx \left\{ \frac{EI_x}{2} z''^2 + [\frac{T_0}{4} + \frac{ES}{8L} \int_0^L z'^2 dx] z'^2 \right\}$$

where E is Young's modulus, I_x is the moment of cross-section area (in our system $I = \pi r^4 / 4$), and $S = \pi r^2$ is the cross-section area. Here, r is the (external) radius of the tube.

Electrostatic Energy

To write down the electrostatic energy for the nanotube system in Figure III-19, we denote the capacitances of barriers connecting the nanotube with the source and drain as C_L, C_R, respectively. The capacitance to the gate per unit length is $c(z)$. Approximating the gate by an infinite plane at distance h from the nanotube, we obtain

$$c(z) = \frac{1}{2\ln(\frac{2(h-z)}{r})} \approx \frac{1}{2\ln(\frac{2h}{r})} + \frac{z(x)}{2h\left[\ln(\frac{2h}{r})\right]^2} \qquad \text{(III-20)}$$

where the Taylor expansion restricts validity to $z << h$. In this limit, van der Waals forces between the nanotube and the side-gate electrode can be neglected. We have mentioned in the fabrication section that distances between nanotubes and side-gate electrodes usually range from 120–150 nm, and the maximal deflection of $z(x)$ is about 1 nm. Thus, $z >> h$ is indeed valid in our case.

To find the electrostatic energy of the system, we need to know the electrical potential ϕ in the nanotube. If there is n excess electrons yielding charge ne on the

nanotube, then the opposite charges induced in those surrounding capacitances should equal to *–ne* by charge neutrality. Hence, we have

$$(V_L - \varphi)C_L + (V_R - \varphi)\, C_R + (V_G - \varphi)C_G = -ne\,,$$

where $V_L = V$ and V_G are the potential of the source and the gate electrodes, while the drain potential is set to zero, $V_R = 0$. Note that the last term in eq. (III-20) depends on the tube displacement and thus on the number of electrons. Therefore, it can not be omitted, as in the standard Coulomb-blockade treatment that replaces this term by the constant, making W_{est} a periodic function of gate voltage.

For a uniform charge distribution, the capacitance to the gate equals

$$C_G = \int_0^L c[z(x)]dx\,.$$

Solving the charge neutrality equation, we find electrical potential on nanotube is

$$\varphi = \frac{n\,q + C_L V + C_G V_G}{C_G + C_L + C_R}\,.$$

The electrostatic energy is expressed by

$$W_{est}[z(x)] = \frac{1}{2}C_L(V-\varphi)^2 + \frac{1}{2}C_R(V_R-\varphi)^2 + \frac{1}{2}C_G(V_G-\varphi)^2 + ne(V_R-V_L)\frac{C_L}{C_\Sigma} + ne(V_R-V_G)\frac{C_G}{C_\Sigma}$$

,

substitute φ and let $V_R = 0$, and the total electrostatic energy is

$$\begin{aligned} W_{est}[z(x)] &= \sum \frac{1}{2}C_i(V_i-\phi)^2 + ne(V_R-V_L)\frac{C_L}{C_\Sigma} + ne(V_R-V_G)\frac{C_G}{C_\Sigma} \\ &= \frac{(ne)^2 - 2ne(C_L V + C_G V_G)}{2(C_L + C_R + C_G)} + \frac{C_L(C_R+C_G)V^2 + C_G(C_L+C_R){V_G}^2 - 2C_L C_G V V_G}{2(C_L + C_R + C_G)}\,. \end{aligned}$$

Minimizing the Entire Energy

Minimize the energy $W_n[z(x)] = W_{el}[z(x)] + W_{est}[z(x)]$ by

$$W_n[z(x)] = \int_0^L \left\{ \frac{EI}{2} z''^2 + \frac{T}{2} z'^2 - \frac{(ne)^2}{L^2 h} z(x) \right\} dx + \frac{(ne)^2 \ln \frac{2h}{r}}{L} - neV_G$$

Introducing the variational principle for this system and setting the residual stress $T_0 = 0$, after operating a few times using integration by parts with the appropriate boundary condition for the doubly clamped beam, $z(0) = z(L) = z'(0) = z'(L) = 0$, leads to the following detailed derivation:

$$\begin{aligned}
&\delta \int_0^L \left\{ \frac{EI}{2} z''^2 + \frac{T}{2} z'^2 - \frac{(ne)^2}{L^2 h} z(x) \right\} dx \\
&= \int_0^L EIz''\delta(z'')dx + \int_0^L Tz'\delta(z')dx - \int_0^L \frac{(ne)^2}{L^2 h}\delta z dx \\
&= \int_0^L EIz'' \frac{\partial^2 \delta z}{\partial x^2} dx + \int_0^L Tz' \frac{\partial \delta z}{\partial x} dx - \int_0^L \frac{(ne)^2}{L^2 h}\delta z dx \\
&= \underbrace{EI\, d(\frac{\partial \delta z}{\partial x}) z''\Big|_0^L}_{=0} - \int_0^L EIz''' \frac{\partial \delta z}{\partial x} dx + \underbrace{Td(\delta z)z'\Big|_0^L}_{=0} - \int_0^L Tz''\delta z dx - \int_0^L \frac{(ne)^2}{L^2 h}\delta z dx \\
&= \underbrace{-EI\, d(\delta z)z'''\Big|_0^L}_{=0} + \int_0^L EIz'''\delta z dx - \int_0^L Tz''\delta z dx - \int_0^L \frac{(ne)^2}{L^2 h}\delta z dx \\
&= \int_0^L \left(EIz'''' - Tz'' - \frac{(ne)^2}{L^2 h} \right) \delta z dx = 0.
\end{aligned}$$

After,

$$IEz'''' - Tz'' = K_0 \equiv \frac{(ne)^2}{L^2 h}$$

where K_0 is the electrostatic force per unit length, which we approximate by a constant. Higher-order terms are small for $z << h$

$$z_n(x) = \frac{K_0 L}{2T\xi}\left[\frac{\sinh \xi L}{\cosh \xi L - 1}(\cosh \xi x - 1) - \sinh \xi x + \xi x - \xi \frac{x^2}{L}\right],$$

where $\xi = \sqrt{\frac{T}{EI}}$.

In $T << EI/L^2$ cases, the tension is much smaller than the rigidity. On the other hand, $T >> EI/L^2$ cases, the tension is much stronger than rigidity, we can find

$$T = \begin{cases} K_0^2 L^6 S/60480EI^2 & T << EI/L^2 \\ (ES/24)^{1/3}(K_0 L)^{2/3} & T >> EI/L^2. \end{cases} \quad \text{(III-21)}$$

In the $T << EI/L^2$ case, the tension is much smaller than rigidity, which indicates a weak bending of the tube, and the tube displacement is small. On the other hand, in the $T >> EI/L^2$ case, the tension is much stronger than the rigidity, which describes the strong bending case, and the tube displacement is large

Discussion

If we take a closer look at eq. (III-21), the external stress force *T* is function of *E*, *I* , *S* , *L*, and K_0. *E* is the Young's modulus; *I*, *S*, and *L* are the geometric parameters. K_0 is the key to link the electrostatic energy to the stress force, since we perform this system in the single-electron transistor operation regime, such that counting the Coulomb blockade oscillations can provide us with the number of electrons in a nanotube. After we find the stress force *T*, we can use eq. (III-19) derived by Euler-Bernoulli beam theory. Find the $\xi = \sqrt{T/EI}$, then we can find the resonant frequency using the external *T*.

III-5 NEMS Actuation and Detection Techniques

For a movable component of an electromechanical system, approaches to actuation and detection are two major considerations of system design. The actuation approaches to a micro- or nano system can include electrostatic, electromagnetic, thermal, or piezoelectric methods and all have their advantages and drawbacks. For example, electrostatic actuation uses less current consumption but requires high operation voltage; on the other hand, the electromagnetic actuation has need of less voltage, but uses significantly higher current consumption. Once the system has been actuated, a detection technique is required to read out the mechanical positions. This can also be carried out by a variety of approaches, for example optical, magneto-motive, electrostatic, thermoelectric, electromagnetic, or piezoelectric techniques. This combination of actuation and detection techniques yields flexibility in customizing sensors for various practical applications.

After preliminary considerations in finding an appropriate technique to apply to our nanotube system, we choose an electrostatic method to actuate nanotubes as well as to detect the motion of nanotube. In addition, we exploit the field-effect transistor properties of a carbon nanotube, which not only performs as a mechanical vibrating element but also an electrical mixer. This mixing technique of readout is required to overcome the impedance mismatch of nanotube to measurement circuit, because while the impedances of nanotubes can vary with many factors—intrinsic properties (i.e., SET behavior, impedance is quite different in the valleys or the peaks of Coulomb oscillations) or extrinsic effects (i.e., the contact resistance due to the fabrication)—they are generally much larger than the typical transmission line impedance of 50 Ω.

III-5-1 Electrostatic Actuation Method

The general idea of the electrostatic actuation is the electromechanical energy conservation in MEMS or NEMS. A spring attached to a movable parallel-plate capacitor is an example of this scheme. The electrostatic and mechanical energy can be easily transformed into each other during pull-in and pull-out cycles.

However, our nanotube electromechanical system is operated as a SET; the mechanical properties coupled with a SET system will be addressed in this section. The conclusion of the following derivations are similar to the general expression of a field-effect transistor or semiconducting/small-band-gap nanotube at room temperature, which have been discussed in Sazonova's thesis [53]. Similar notations are used to make easy comparison, and the fundamental concept of SET can be found in Chapter I.

The carbon nanotube resonator system we work with is shown in Figure III-19. The SWNT acts as a quantum dot which connects source-drain electrodes through tunnel junctions. The gate electrode can tune the electrical potential of the nanotube. We start with n number of electron charges giving a total charge ne on a nanotube (or $-ne$ for holes), here we assume there is zero bias between source and drain voltages (V_L and V_R, respectively), with the drain contact grounded, yielding $V_L = V_R = 0$. From Section I-5, we can obtain the total equilibrium electrostatic energy as

$$E = \frac{1}{2C_\Sigma}(C_G V_G + ne)^2 + \frac{1}{2}C_G(1 - 2C_G/C_\Sigma)V_G^2 . \qquad \text{(III-23)}$$

Minimizing the energy with respect to n, we obtain $n = -C_G V_G / e$, corresponding to an induced charge $Q_0 = -C_G V_G$. As we discussed in Chapter I before, the charge Q_0 is a continuous variable and can be an arbitrarily small fraction of the charge e.

As described in Section I-5-4, when the energy is in minimum but Q_0 is not an integer (see Figure I-14), the maximum energy of the first term is $E_c/4$ and the second term is usually dominated. Thus, we can neglect the first term and obtain

$$E = \frac{1}{2} C_G (1 - 2C_G / C_\Sigma) V_G^2 .$$

Thus, the electrostatic force in the z direction is

$$\begin{aligned} F_{el} &= -\frac{dE}{dz} = -\frac{2(C_\Sigma - C_G)^2 - C_\Sigma^2}{2C_\Sigma^2} C_G' V_G^2 \\ &= \frac{1}{2} g\, C_G' V_G^2, \end{aligned}$$

where $C_G' = dC_G / dz = \frac{d}{dz} \int_0^L c[z(x)]dx$ and $g = -[2(C_\Sigma - C_G)^2 - C_\Sigma^2] / C_\Sigma^2$.

If there is a small AC voltage at frequency ω applied to the gate electrode, shown as

$$V_G = V_G^{DC} + \tilde{V}_G^{\omega},$$

where $\tilde{V}_G^{\omega} = \tilde{V}_G \cos(\omega t)$, the electrostatic force applied on the nanotube is

$$\begin{aligned} F_{el} &\cong \frac{1}{2} g\, C_G' (V_G^{DC^2} + 2V_G^{DC} \tilde{V}_G^{\omega}) \\ F_{el}^{DC} &= \frac{1}{2} g\, C_G' V_G^{DC^2} \\ \tilde{F}_{el}^{\omega} &= g\, C_G' V_G^{DC} \tilde{V}_G^{\omega}. \end{aligned} \qquad \text{(III-24)}$$

The above equations are the expressions for the actuation forces, where the DC term is used to control the axial tension along the nanotube while the AC term stimulates the nanotube into the motion.

III-5-2 Capacitive Sensing Technique

In this electromechanical system, we can write down the capacitance as a function of vertical distance along *x* direction $C_G = \int_0^L c[z(x)]dx$ (in Figure III-19). In order to couple the mechanical degree of freedom into the electronic quantity, i.e., current or conductance, at the certain source-drain voltage V_{sd}, we can assume the conductance *G* is a function of the applied gate voltage and gate capacitance as $G(V_G, C_G)$. Once the nanotube is in motion, we can denote the additional displacement by $\tilde{z}^{\omega}$ due to a small AC modulation of gate voltage $\tilde{V}_G^{\omega}$, and the total gate voltage as $V_G = V_G^{DC} + \tilde{V}_G^{\omega}$. Thus, the capacitance $\tilde{C}_G^{\omega}$ is modulated at the same harmonic vibration as $\tilde{z}^{\omega}$ and total gate capacitance can be expressed as $C_G[z_0 + \tilde{z}^{\omega}] \approx C_G^{DC} + C'\tilde{z}^{\omega}$, where $\tilde{C}_G^{\omega} \cong C'\tilde{z}^{\omega}$. To describe the conductance with this small AC modulation at ω, extract the lowest order of Taylor's expansion with small $\tilde{V}_G^{\omega}$ and $\tilde{C}_G^{\omega}$, and we obtain

$$G(V_G + \tilde{V}_G^{\omega}, C_G + \tilde{C}_G^{\omega}) \cong G(V_G, C_G) + \frac{dG}{dV_G}\tilde{V}_G^{\omega} + \frac{dG}{dC_G}\tilde{C}_G^{\omega} + \dots . \qquad \text{(III-25)}$$

In the above we assumed that the modulation is small and neglected the cross term.

In order to simplify the above equation into an expression dependent upon measurable quantities, we consider the excess static charge Q_0 induced by the applied gate voltage as $Q_o = -C_G V_G$. In the SET operating regime, we can tune the gate voltage and let the induced charge Q_0 be such that the operating point is very close to the shoulder of a Coulomb peak; the equilibrium number of electron on the shoulder of a peak is very close to the half integer $n + 1/2$, corresponding to the maximum of a Coulomb blockade peak.

Here we treat C_G and V_G as independent variables; $Q_o = -C_G V_G$ is a continuous variable without any constraint. Any charge difference can come from two terms $\delta Q_0 = -\delta C_G V_G - C_G \delta V_G$. Thus, using the chain rule

$$\frac{\partial G}{\partial C_G} = \frac{\partial G}{\partial Q}\frac{\partial Q}{\partial C_G} = -\frac{\partial G}{\partial Q} V_G . \tag{III-26}$$

And we can also obtain

$$\frac{\partial G}{\partial V_G} = \frac{\partial G}{\partial Q}\frac{\partial Q}{\partial V_g} = -\frac{\partial G}{\partial Q} C_G . \tag{III-27}$$

Thus from eq. (III-27) we can write down the relation

$$\frac{\partial G}{\partial Q} = -\frac{\partial G}{\partial V_G}\frac{1}{C_G} . \tag{III-28}$$

Substituting the eq. (III-28) into eq. (III-26)

$$\frac{\partial G}{\partial C_G} = \frac{\partial G}{\partial V_G}\frac{V_G}{C_G} . \tag{III-29}$$

Therefore, we can rewrite the conductance with this small AC modulation at ω,

$$G(V_G + \tilde{V}_G^{\omega}, C_G + \tilde{C}_G^{\omega}) \cong G(V_G, C_G) + \underbrace{\frac{dG}{dV_G}\tilde{V}_G^{\omega} + \frac{dG}{dC_G}\tilde{C}_G^{\omega}}_{\tilde{G}_G^{\omega}} + \ldots$$

$$\begin{aligned} \tilde{G}_G^{\omega} &\cong \frac{dG}{dV_G}\tilde{V}_G^{\omega} + \frac{dG}{dV_G}\frac{\tilde{C}_G^{\omega}}{C_G}V_G \\ &= \frac{dG}{dV_G}\left(\tilde{V}_G^{\omega} + \frac{\tilde{C}_G^{\omega}}{C_G}V_G\right). \end{aligned} \tag{III-30}$$

The above expression is the conductance coupled with the mechanical motion at the frequency ω.

III-5-3 Mixing Technique

To detect the motion of nanotube on resonance, we exploit its transport characteristic based on its single electron transistor behavior, the Coulomb blockade feature, which leads to much higher sensitivity of $\frac{dG}{dV_G}$ than in the previous experiments at room temperature. These previous works [49, 50] have been tested by using 1–2 μm semiconducting or small-band-gap carbon nanotubes at room temperature. We apply an AC source voltage at frequency $\omega + \Delta\omega$ and current can be expressed into two terms with different frequencies,

$$\begin{aligned} I = GV_{sd} &= (G^{DC} + \tilde{G}^{\omega}) \cdot \tilde{V}_{sd}^{\omega+\Delta\omega} \\ &= G^{DC} \cdot \tilde{V}_{sd}^{\omega+\Delta\omega} + \tilde{G}^{\omega} \cdot \tilde{V}_{sd}^{\omega+\Delta\omega}. \end{aligned}$$

The first term of the equation is at the original frequency $\omega + \Delta\omega$, and the second term is the mixing signal from

$$\begin{aligned} \tilde{G}^{\omega} \cdot \tilde{V}_{sd}^{\omega+\Delta\omega} &= \tilde{G}\cos(\omega t) \cdot \tilde{V}_{sd}\cos((\omega + \Delta\omega + \phi)t) \\ &= \frac{1}{2}\tilde{G} \cdot \tilde{V}_{sd}[\cos((2\omega + \Delta\omega)t + \phi) + \cos(\Delta\omega t + \phi)]. \end{aligned}$$

Taking the low frequency component $\Delta\omega$,

$$\begin{aligned} I^{\Delta\omega} &= \frac{1}{2}\tilde{G} \cdot \tilde{V}_{sd} \\ &= \frac{1}{2}\frac{dG}{dV_G}\left(\tilde{V}_G + \frac{\tilde{C}_G}{C_G}V_G^{DC}\right) \cdot \tilde{V}_{sd} \\ &= \underbrace{\frac{1}{2}\frac{dG}{dV_G}\tilde{V}_G \cdot \tilde{V}_{sd}}_{background} + \underbrace{\frac{1}{2}\frac{dG}{dV_G}\frac{\tilde{C}_G}{C_G}V_G^{DC} \cdot \tilde{V}_{sd}}_{mechanical}. \end{aligned} \tag{III-31}$$

The mixing signal equation reveals two origins of contributions, the first term is the background signal and the second term is due to the mechanical motion. Furthermore, both background and mechanical signals are proportional to a derivative of the

transconductance $\frac{dG}{dV_G}$, which can be greatly improved at low temperature in the Coulomb blockade regime. In this regime $\frac{dG}{dV_G}$ is proportional to the height of Coulomb peaks, and the background can always be subtracted.

III-5-4 Displacement of a Vibrating Nanotube

In this section, we would like estimate how much displacement is induced in this electromechanical system. If we take another look at eq. (III-31) and consider the rms current:

$$I_{rms} = \frac{1}{2\sqrt{2}} \frac{dG}{dV_G} \frac{\widetilde{C}_G}{C_G} V_G^{DC} \cdot \widetilde{V}_{sd},$$

where I_{rms} is the measureable quantity; $\frac{dG}{dV_G}$ can be found in a DC measurement. V_G^{DC} and $\widetilde{V}_{sd}$ are the known voltage sources. Therefore, the ratio of the capacitance change can be expressed as

$$\frac{\widetilde{C}_G}{C_G} = \frac{1}{\frac{dG}{dV_g}} \frac{2\sqrt{2}\ I_{rms}}{V_G^{DC} \cdot \widetilde{V}_{sd}}.$$

Hence, we can first get the estimation of $\widetilde{C}_G$ based on all known parameters and we assume this is a simple spring, such that we can find the effective spring constant k_{eff} and displacement δz. As an order-of-magnitude estimate, we consider only the bending stress in this system, and thus according to the eq. (III-14), we can write down the force per unit length as

$$f = -\frac{\partial^2}{\partial x^2}(EI_A \frac{\partial^2 u}{\partial x^2}) + T \frac{\partial^2 u}{\partial x^2}.$$

Here *f* is the electrostatic force on the nanotube, assuming uniform distribution along the tube axis. In this case, we ignore the axial tension *T* and the mass of nanotube itself. In

addition, the material is homogenous along the tube axis, which applies to the cross-section of tube the same in every position. We obtain

$$f = -EI_A \frac{\partial^4 u}{\partial x^4},$$

the solution is $u(x) = C_0 + C_1 x + C_2 x^2 + C_3 x^3 + C_4 x^4$ with the doubly clamped boundary

$$u(0) = u(L) = \left.\frac{\partial u}{\partial x}\right|_{x=0} = \left.\frac{\partial u}{\partial x}\right|_{x=L} = 0$$

and the equation itself $f = -EI_A \frac{\partial^4 u}{\partial x^4}$ at any point.

Thus, we yield the solution as

$$u(x) = \frac{f x^2 (L-x)^2}{24 EI_A},$$

and the maximum deflection at the center for a uniformly loaded beam is given

$$u\left(\tfrac{L}{2}\right) = \frac{f L^4}{384 EI_A}$$

where f is the loading force per unit length, E is the modulus of elasticity, and I_A is the area moment of inertia of the beam. Since the force F is fL, we find $k_{eff} = 384 EI_A / L^3$. On resonance the force is enhanced by the quality factor *Q*, so we have

$$\delta z = u\left(\tfrac{L}{2}\right) = QF / k_{eff} . \qquad \text{(III-32)}$$

Now we need to find *F*. This follows from electrostatics. The gate capacitance follows from that between a wire and a plane, with r the nanotube radius, z the height above the gate, and ε_0 the vacuum permittivity:

$$C_G \cong \frac{2\pi\varepsilon_0 L}{\ln(2z/r)}.$$

The force F from the previous section is then given by

$$\tilde{F}_{el}^{\omega} = g\, C_G' V_G^{DC} \tilde{V}_G^{\omega}$$

where $g = -[2(C_\Sigma - C_G)^2 - C_\Sigma^2]/C_\Sigma^2$, $g \cong -1$ when $C_G << C_L, C_R$.

For mixing, only the ω frequency component is relevant:

$$\tilde{F}_{el}^{\omega} = -\frac{2\pi\varepsilon_0 L}{z\left[\ln(2z/r)\right]^2} V_G^{DC} \tilde{V}_G^{\omega}. \qquad \text{(III-33)}$$

From eq. (III-32) and eq. (III-33), we can find δz:

$$\delta z = -\frac{2\pi\varepsilon_0 L}{z\left[\ln(2z/r)\right]^2} V_G^{DC} \tilde{V}_G^{\omega} \frac{QL^4}{384EI_A}.$$

Finally, from this we can find $\delta C = dC_G/dz\ \delta z$:

$$\delta C = \left\{\frac{2\pi\varepsilon_0 L}{z\left[\ln(2z/r)\right]^2}\right\}^2 V_G^{DC} \tilde{V}_G^{\omega} \frac{QL^4}{384EI_A}.$$

Looking at (III-31), we see that the current signal decreases as L^5, but is proportional to $\tilde{V}_{sd}\tilde{V}_G V_G^{DC\,2}$, and varies as a large power in the length. Thus, we expect a decrease in length must be compensated for by significantly increasing the various applied voltages in order to maintain the same signal level.

III-6 Experimental Setup

Our experimental setup consists of the following instruments: (1) two Agilent 8648D Synthesized RF Signal Generators for source and gate electrodes; (2) one Stanford

Research System Model SR830 DSP lock-in amplifier; (3) and one current pre-amplifier, DL instruments Model 1211. Moreover, we have a customized cryostat with a dry pump, Adixen - Drytel 1025. The whole setup for the mass sensing application is much simpler than an Oxford Helium-3 system.

III-6-1 Circuit Design

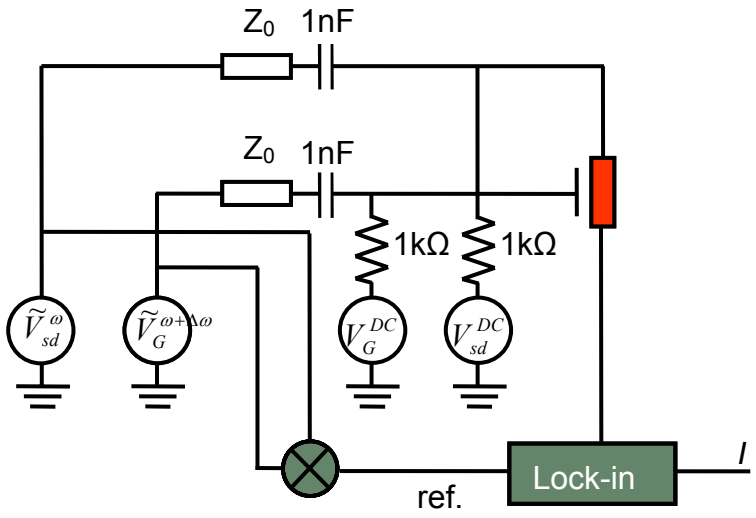

Figure III-21. Schematic diagram of the measurement circuit. The transmission lines with characteristic impedance Z_0 = 50 Ω are both terminated at each end with a 50 Ω resistor to ground. There are two RF voltages: $\tilde{V}_{sd}^{\omega}$ and $\tilde{V}_{G}^{\omega+\Delta\omega}$ are the AC source-drain and gate voltage, respectively. There are two DC voltages: V_{sd}^{DC} and V_G^{DC} are DC source-drain and gate voltage, respectively. The nanotube is shown in red.

The following schematic diagram is the circuit design for a two-source mixing technique. Since the operating frequency is normally below 1 GHz, and the wavelength of a 1 GHz signal in free space is about 30 cm, which is much longer than our device circuit in the sample holder (3 cm), the only challenge is to put all the connector and components into a compact circuit board. To this end we designed a 3D circuit board integrated with surface-mounted resistors and capacitors. We used the vector network analyzer to check the reflection coefficient, and this circuit has less than 10% reflection over a range of 10 MHz–1 GHz.

III-6-2 Customized Cryostat System Design—Cryotube

The advantage of running this experiment at low temperature, as mentioned before, is to achieve high $\frac{dG}{dV_G}$ from the Coulomb blockade features and also to enable adsorbates to stick on the nanotube without thermally driven desorption for the application of atomic-scale mass sensing.

Initially, in the interest of fundamental research, our devices were operated in Oxford Helium-3 insert incorporated with SMA cables and several modifications (i.e., a series of RF attenuators thermally anchored at different reservoirs to reduce the thermal noise). After the preliminary result from loading helium gas in the sample chamber, we became aware of the possibility of reaching atomic-scale mass sensing. By our estimate, it is possible to reach single proton mass sensitivity in the optimal case, which means it may eventually be possible to distinguish isotopes in this NEMs mass sensor. Thus, atomic-scale mass sensing is a milestone we were capable of reaching. However, our Oxford Helium-3 insert lacks a line of sight allowing atoms (except helium which does not condense on the cold surfaces) to arrive on the nanotube, thus we immediately designed and built a customized cryotube to achieve this atomic-scale mass sensing.

This customized cryotube is designed to meet several criteria: clear line of sight, liquid helium temperature, high vacuum, electrical feedthrough, and easy to operate. In the following, several major concepts of cryostat design will be introduced.

Baffles with the BeCu Fingers

For the application of mass sensing, the cryostat system must be operated at high vacuum ($< 10^{-7}$ torr) to allow the atomic/molecular beam to arrive ballistically on our devices. It would not be possible to maintain the system at liquid-helium temperature by exchange gas alone. Besides, there is always thermal radiation that can heat up the cold reservoir.

In the beginning of the cooling process, a few Torr of helium gas are added in the cryotube as exchange gas, which assists in cooling down the system quickly. After the

cryotube reaches liquid-helium temperature for 10 minutes, we pump out the exchange gas for a couple of hours, using built-in Allen-Bradley resistors to monitor the interior device temperature. In order to maintain the cryotube at liquid-helium temperature, the only means of cooling is via thermal conduction. Therefore, we designed a series of cooper baffles with the BeCu fingers, to perform as good thermal anchors and physical baffles/cold trap for gas that is not following the line of sight trajectory.

The BeCu fingers are flexible and can easily slide in and out of the can and make reasonable thermal contact to conduct heat. The baffles are placed below the liquid-helium level. These thermally anchored cold baffles not only can trap the atomic or molecular beam off the line of sight, but also block the radiation from the top at room temperature. We successfully operated this cryostat with high vacuum at around 5 K.

Electrical Feedthrough

Seven Manganin DC wires and two stainless steel SMA feedthroughs were placed inside the cryotube: five DC lines for devices and two for the Allen-Bradley thermal resistor. Note that the DC and RF wire materials are carefully chosen to prevent excessive heat from reaching the sample.

Nozzles

The nozzle is best maintained at room temperature, in order to prevent the aperture from being clogged by ice. We have three nozzle aperture sizes: 135 mm, 200 mm, and 300 mm. From the known geometry of the cryotube, we can estimate the atomic flux for the analyte gases. An appropriate atomic flux can lead us to observe one or two atoms arriving on nanotube resonator within a few seconds without building a mechanical shutter [38].

In order to calculate the atomic flux, we first consider the Knudsen number $Kn = \lambda / L$, the ratio of the molecular mean free path length λ to a representative physical length scale L, taken to be the diameter of the aperture. In our experiment for all kinds of gases,

the *Kn* is greater than 1, and therefore we can assume those gases are in thermal equilibrium in the reservoir and effuse into the sample space through the aperture. This enables the determination of the atomic flux φ_0 through the aperture, yielding $\varphi_0 = P/\sqrt{2\pi m k_B T}$, where *P* is the pressure in the reservoir, *m* is the atomic or molecular mass, k_B is Boltzmann's constant, and *T* is the temperature.

Thermal Interfacial Resistance

We can manage the thermal conduction in every piece of material by checking the thermal properties of the materials. Nevertheless, the thermal interfacial resistances are always not easy to deal with. They are different for different materials. The interfacial resistance is, to a good approximation, a function of the normal force between different surfaces. However, grease also helps, presumably because it increases the effective contact area between materials. Therefore, to connect two pieces of material, there are a few options to use: apply grease (thermally conductive but electrical insulating), use screws to increase the normal force between them, or use stiff spring. Gold-plated copper block with screws is also recommended. Detailed discussion can be found in ref. [54].

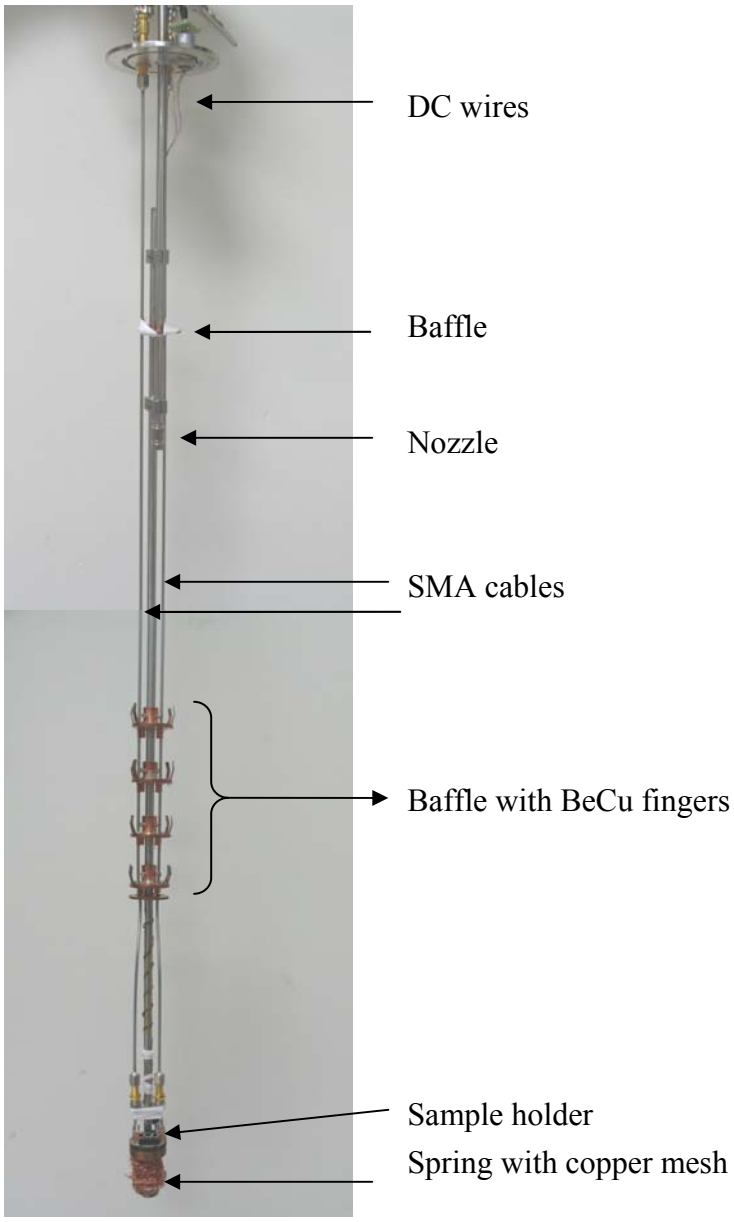

Figure III-22. The interior design of the customized cryotube. The total length of this tube is about 140 cm.

III-7 Mass Sensing

At the temperature $T \approx 6$ K of our experiment, the nanotubes act as single-electron transistors (SET) in which the charge on the nanotube is an integer multiple of the electron charge e [55]. As the gate voltage V_G is swept, electrons enter the SET one at a

time, with each transition between discrete charge states producing a Coulomb peak in the source-drain conductance (see, e.g., ref [56]). Figure III-23 shows this behavior. To measure the resonant vibrational amplitude of the carbon nanotubes, we drive their motion electrostatically and take advantage of these SET properties to sense the resulting displacement capacitively [57]. This approach is adapted from that described by Sazonova et al. [49] Figure III-21 shows a diagram of the experimental setup. A voltage $V_{sd} = V_{sd}^{DC} + \widetilde{V}_{sd}\cos(\omega t)$ is applied across the source and drain electrodes, where t is the time and ω is the frequency, while a voltage with a detuned AC component at frequency $\omega + \Delta\omega$ is applied to the gate so that $V_G = V_G^{DC} + \widetilde{V}_G \cos[(\omega + \Delta\omega)t]$. The nanotube transistor mixes the signals to yield a current I that is measured by a lock-in amplifier with a ~1 Hz bandwidth at the difference frequency $\Delta\omega$. Tuning ω to a nanomechanical resonance of the nanotube produces vibrations that modulate the tube-gate capacitance, changing the measured I in proportion to the vibration amplitude.

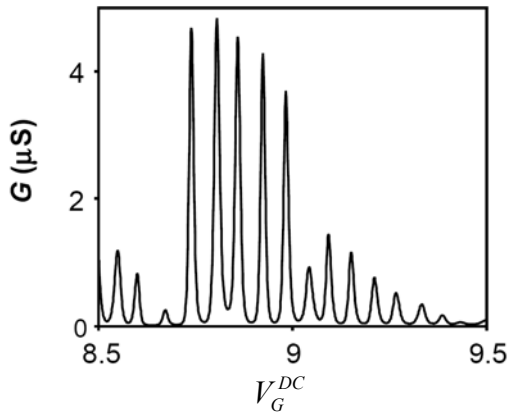

Figure III-23. Source-drain conductance versus gate voltage showing Coulomb peaks and single-electron transistor behavior at $T \approx 6$K.

Figure III-24 (a) shows a color-scale plot of I versus V_G^{DC} and $f = \omega/2\pi$ at $T \approx 6$ K for a suspended nanotube device. The tube diameter d is ~ 1 nm, as determined by atomic force microscopy on the substrate-supported segment. From d, we estimate the suspended tube mass $m_0 \sim 1000$ zg. Typical values for the applied voltages are $\widetilde{V}_{sd} \approx 0.8$ mV and

$\tilde{V}_G \approx$ 0.8 mV. The current signal measured at the lock-in amplifier is proportional to dG/dV_G [49, 50]. On the shoulders of the Coulomb peaks dG/dV_G becomes large, as high as ~ 380 μS/V, producing the vertical stripelike background in Figure III-24 (a).

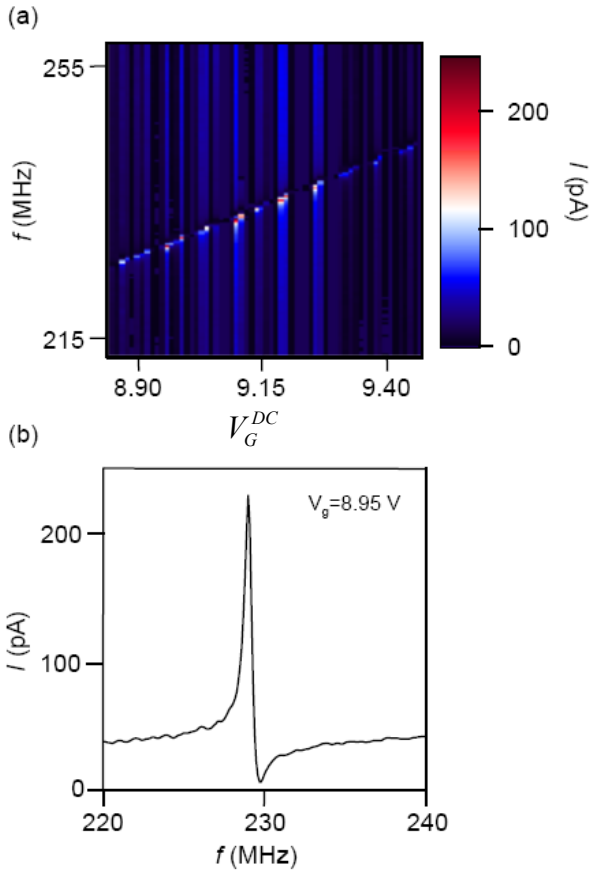

Figure III-24. Nanotube resonator vibration characteristics. (a) Color plot of the mixing current I detected by the lock-in amplifier at the difference frequency, as described in the text, versus DC gate voltage V_G^{DC} and drive frequency. (b) Line trace of the mixing current I versus the drive frequency f. A peak occurs when the frequency is tuned to a nanomechanical resonance of the nanotube device. Achieving such large peak heights and resulting signal-to noise ratio required the side gate to be in close proximity to the nanotube, typically 150 nm or less.

The approximately horizontal feature corresponds to a nanomechanical resonance. Increasing V_G^{DC} increases the tension in the nanotube, raising its resonance frequency[49].

This produces a finite-slope feature [49, 50]. From the small slack we observe in our SEM images, we expect that the nanotube in our device behaves as a stretched string [48, 49]. Following a similar analysis as given in ref. [49], we find the characteristic vibration amplitude for our system with the given $\widetilde{V}_{sd}$ and $\widetilde{V}_G$ is ~ 1 nm. A line trace of I versus f is shown in Figure III-24 (b), showing that the resonance has a quality factor Q ~ 200. The characteristic fundamental-mode resonance frequencies f_0 = 100−300 MHz are consistent with those expected for single-walled nanotubes with the ~ 400−500 nm length and nanometer-scale diameters under study [49, 58]. Note that the line shape is asymmetric, which may indicate the onset of nonlinearity[49, 59]. At sufficiently large drives, such nonlinearity may produce an upper bound on the signal-to-noise ratio for frequency measurements [59], although this is not a limitation of our present experiment.

III-7-1 Xenon Mass Loading at T ~5-6K

After identifying a promising resonance peak (typically > 100 pA for the given $\widetilde{V}_{sd}$ and $\widetilde{V}_G$), we expose the device to an atomic or molecular beam. Figure III-22 shows the experimental setup, which is similar to that employed by Yang et al. [38] to mass load top-down fabricated nanowire mass sensors. A reservoir maintained near room temperature connects to the sample space through a small aperture (≈ 135 μm in diameter) and is filled with the analyte gas. Baffles maintained near liquid helium temperature are interposed between the aperture and sample and serve to block any atoms that are not on a ballistic trajectory from the inlet. Assuming that the gas effuses into the sample space through the aperture enables the determination of the atomic flux φ_0 through the aperture, yielding $\varphi_0 = P/\sqrt{2\pi m k_B T}$, where P is the pressure in the reservoir, m is the atomic or molecular mass, k_B is Boltzmann's constant, and T is the temperature. From φ_0 and the distance between the aperture and the sample $h \cong 0.9\,m$, we determine the atomic flux arriving at the nanotube, $\varphi_n = A_0 \varphi_0 / 2\pi h^2$, where $A \cong 1.4 \times 10^{-8}\, m^2$ is the area of the aperture used in our experiments.

We first fill the reservoir with Xe. The main panel of Figure III-25 shows that the resonance traces shift and broaden as the atoms land on the nanotube and adsorb on the surface. The amplitude also decreases slightly. The broadening and amplitude decrease indicate a reduction in the effective quality factor of the nanotube resonator, although further experiments are required to address the origin of this behavior. The black trace shows the initial resonance, while the red and blue traces show the resonance after ≈ 600 s and ≈ 1600 s, respectively. Based on the resonance frequency shift $\Delta f_0 \approx 3\,\mathrm{MHz}$, which in a harmonic oscillator picture for the vibrating nanotube should follow $\Delta f_0 / f_0 = m_A / 2m_0$, where m_A is the adsorbed mass, we deduce that the m_A corresponds to approximately 100–200 Xe atoms. At the low temperature of our experiment, desorption does not readily occur and the resonance frequency remains stable once the reservoir is pumped out. Finally, we note that in an independent trial we mass loaded the resonator with a constant background pressure of Helium and found that the frequency increased with the gate voltage magnitude, with a similar slope as in vacuum.

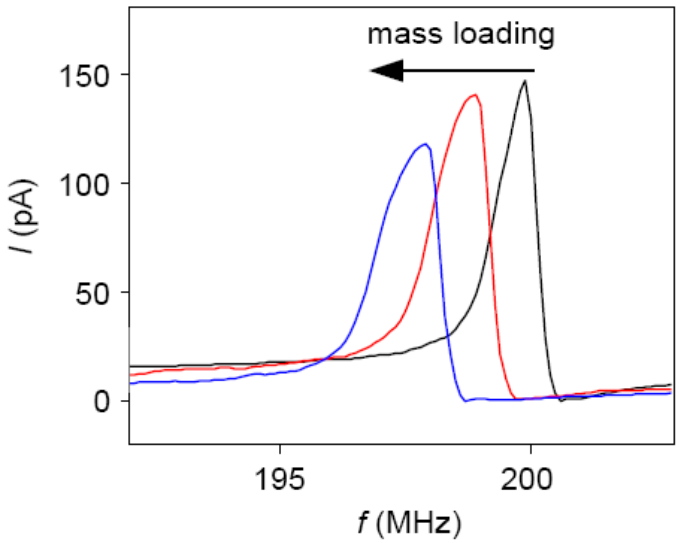

Figure III-25. Response of nanomechanical resonance under mass loading and experimental setup. Mixing current I versus drive frequency f for a resonator device during mass loading by Xe. The black curve shows the initial resonance, the red curve after mass loading for ≈ 600 s, and the blue curve after mass loading for ≈ 1600 s.

III-7-2 Atomic-Scale Mass Sensing

The large observed shifts for the small adsorbed mass suggests our devices could be sensitive to the arrival of individual atoms. To explore this, we fixed the drive frequency to the side of the resonance peak and then monitored the lock-in current as a function of time. Changes in the resonance frequency thereby produced changes in the lock-in current. We then exposed the nanotube to an atomic arrival rate of ~ 3 atoms/s by filling the reservoir to a pressure of ~ 1 Torr. Before the mass loading begins by filling the reservoir, I is roughly constant, demonstrating the stability of our device. Once the Xe fills the reservoir, at the time indicated by the arrow, I begins to increase as the resonance peak shifts downward in frequency due to the mass loading. Remarkably, I shows a series of steplike features with the largest ~ 10 pA as the Xe flux is maintained. After ~ 600 s, the reservoir is emptied and the current rise stops.

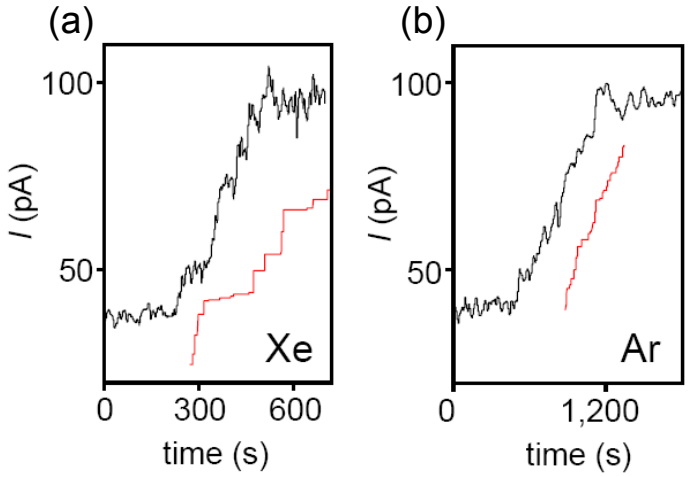

Figure III-26. (a) Black curve: mixing current I versus time as the nanotube resonator is mass loaded with Xe. The mass loading begins at the time indicated by the black arrow and ends at the blue arrow. Red curve: a simulated data trace with the parameters given in the text. Inset: time derivative of the current smoothed with a 50 s window averaging. The black arrow indicates the start of the mass loading, and the blue arrow the end. (b) Similar data as in (a), but for Ar.

To understand the origin of these features, we note that the expected shift in frequency Δf_0 depends on the location at which the atom adsorbs, with the maximum effect

occurring for adsorption in the center of the nanotube. Modeling the nanotube as a stretched string and using the result for the frequency shift due to an attached point mass (e.g., ref. [60]), we find that for $m << m_0$, where m is the atomic mass

$$\frac{\Delta f_0}{f_0} \cong -\frac{m}{m_0}\sin(\pi a / L)\sin[\pi(L-a)/L] \qquad \text{(III-34)}$$

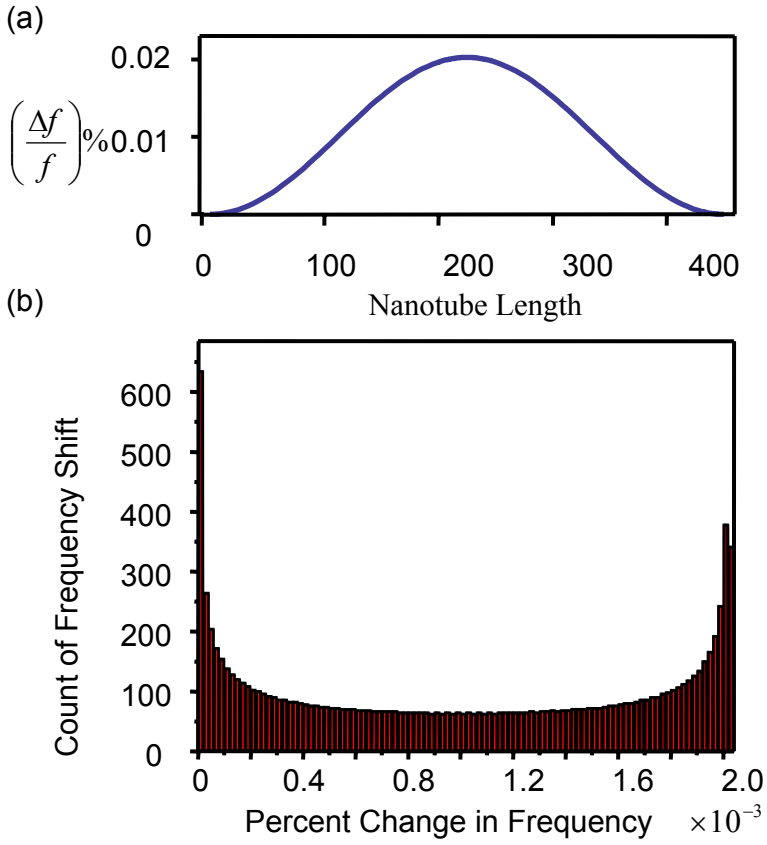

Figure III-27 Simulation of a point mass attached on the different position of nanotube. (a) The simulated distribution of frequency change by a single atom landing on the nanotube. (b) A simulated distribution of count of frequency shifts corresponding to (a). Both simulations are based on the following device parameters: length is 450 nm, diameter is 1 nm, resonant frequency is 223 MHz, nanotube mass = 1076 zg, adsorbate: Xenon (0.218 zg).

where a is the position along the nanotube at which the atom absorbs, and L is the suspended length. Assuming the atoms land anywhere along the nanotube with equal

probability, the mean of $\Delta f_0 / f_0$ is $\langle \Delta f_0 / f_0 \rangle = m / 2m_0$, and the mean square value is $\left\langle (\Delta f_0 / f_0)^2 \right\rangle = \frac{3}{8}(m/m_0)^2$. A simulation of a point mass attached on a different position of nanotube is shown in Figure III-27 (a), we can easily tell the largest frequency change happened in the center of the nanotube. Here we assume that we are exciting the fundamental mode, although relaxing that assumption yields the same results. The general description for any higher modes is that the largest frequency changes happen in the antinodes. There is another simulation of numbers of counts for getting the large frequency changes for the fundamental mode as well in Figure III-27 (b). Two piles of counts fall into the extreme cases indicating the contributions from the antinodes, where the frequency shift is stationary with respect to position variations.

The red trace in Figure III-26 (a) shows a simulated time trace of the current based on eq. (III-34), using the parameters $m_0 \sim 1000$ zg, $m = m_{Xe} = 0.218$ zg, and an adsorption rate of 0.07 atoms/s, determined from m_0 and the slope of the frequency versus time curve. The trace, plotted without free parameters, shows a series of steps each corresponding to the adsorption of an atom. The largest single steps occur when the atoms land near or at the center of the tube and are of magnitude 5.8 pA. In comparison, the root-mean-square noise level we observe is ~ 1.4 pA. This calculation suggests that our measurement is sensitive to the added mass of individual Xe atoms, provided they land near the tube center. Steps of this order of magnitude are apparent in Figure III-26(a), although we cannot exclude the possibility of several atoms adsorbing on the nanotube within the 1 s measurement time constant. On the basis of $\langle \Delta f_0 / f_0 \rangle$ given above and the total $\Delta f_0 / f_0 \sim 3600$ ppm for the entire mass loading period, we estimate the nanotube captured ~ 30 Xe atoms during the mass loading process. This indicates that only about 3% of the incident Xe atoms stick to the surface upon colliding with the nanotube, consistent with molecular dynamic calculations of Xe collisions with nanotubes [61, 62], which predict that nanotubes will capture and adsorb only a small fraction of incident atoms. Note that, compared to graphene, the highly curved geometry of a nanotube produces a range of effective incident angles to the normal and is expected to somewhat

lower the binding potential energy. In addition, the sticking coefficient may be further reduced by the presence of surface impurities [63], e.g., processing residue.

Figure III-26(b) shows similar data taken by mass loading the nanotube with Ar. The reservoir is loaded at the time indicated by the arrow and emptied after about ~ 1200 s. The mean mass accumulation rate is ~ 2 times smaller than for the data shown in Figure III-26(a), although the reservoir pressure was larger, suggesting that the sticking coefficient for Ar on the nanotube is smaller than that for Xe. The red curve below the data shows a simulated trace with m_0 = 1000 zg, $m = m_{\mathrm{Ar}}$ = 0.066 zg, and an adsorption rate of ~ 0.09 atoms/s, which appears similar to the data. Compared to the data for Xe, the Ar data has narrower plateaus and shorter steps.

III-7-3 Atomic Shot Noise Analysis

To use nanotubes as an atomic scale mass sensor, we require a measurement of m_0. To achieve this, we note that these frequency shifts during the adsorption could be viewed as arising from shot noise due to the arriving atoms, similar to the adsorption-desorption noise expected for a resonator immersed in a gas [64-66]. Studying the shot noise enables the statistical fluctuations in mass changes due to atomic arrival to be analyzed even when the smallest individual steps may be obscured by the noise floor present in the measurement. We now compute the expected magnitude of the shot noise. Shot noise produces fluctuations in the mass arrival current dm_A/dt. The mean value of $dm_A/dt = \Gamma m$, where Γ is the mean atomic adsorption rate. This is related to the mean rate of increase $H = dI/dt$ in the current by $\langle H \rangle = \Gamma \langle \Delta f_0 / f_0 \rangle f_0 \, dI/df = \frac{1}{2} \Gamma \, m/m_0 f_0 \, dI/df$, where dI/df is the slope of the resonance curve at the operating point, taken to be roughly constant over a significant portion of the side of a resonance. The shot noise power S of H is $S = 2\Gamma \langle \Delta I_0^2 \rangle$, where $\langle \Delta I_0^2 \rangle$ is the mean-square current increase from a single atom adsorption event. From this we find $t_0 \sigma^2 = \frac{3}{4} m/m_0 \, dI/df \, f_0 \langle H \rangle$, where t_0 is an averaging time window ($1/t_0$ is the effective measurement bandwidth) and σ is the

standard deviation of the window-averaged H. This expression can be rearranged to express the mass ratio m/m_0 in terms of only known or measurable parameter:

$$\frac{m}{m_0} = \frac{4}{3}\frac{t_0\sigma^2}{\langle H\rangle f_0\, dI/df} \tag{III-35}$$

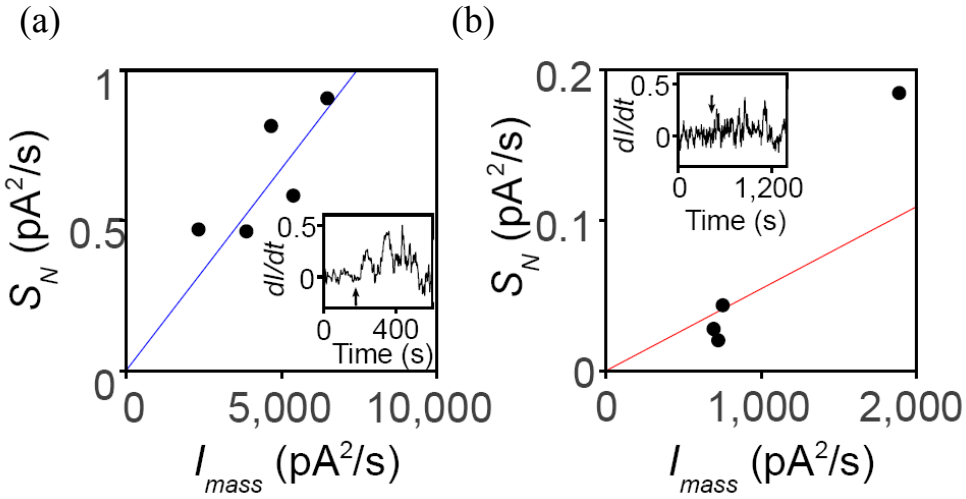

Figure III-28. The effective shot noise power versus effective mass current for a number of different data runs (a) for Xe and (b) for Ar. In measuring the shot noise, care was taken to select only those data sets in which the current was generally monotonically increasing. Some data sets, particularly after the nanotubes had a significant amount of accumulated mass, showed large up and down current fluctuations relative to the initially measured background noise, which we attribute to the surface diffusion of adsorbed atoms, possibly driven by the impinging atoms. Data sets with such fluctuations did not generally yield consistent results for the shot noise versus the adsorbate atomic mass.

We now use this result to determine m_0 from the experimental data. The inset to Figure III-28(a) shows a plot of H with $t_0 \sim 50$ s for the data shown in the main panel. Inspecting eq. (III-35) indicates that if we plot an effective noise power $S_N = \frac{4}{3}t_0\sigma^2$ versus an effective mass current $I_{mass} = \langle H\rangle f_0\, dI/df$, we expect the data to fall on a straight line with a slope equal to m/m_0. The solid circles in Figure III-28(a) show S_N versus I_{mass} taken from five different data sets. In each data set, to account for excess fluctuations due to the background noise, we subtract the variance taken from before

mass loading from the variance taken during mass loading. Fitting a straight line that goes through the origin using statistical weighting (blue line) yields a slope 1.4×10^{-4}. Using the known mass of Xe of 0.218 zg yields a nanotube mass $m_0 \sim 1600$ zg, consistent with the expected value based on the nanotube diameter and length. We have therefore used Xe to weigh the suspended nanotube segment.

With the measured mass of the nanotube, the atomic mass of Ar can then be determined from our data, such as shown in the inset to Figure III-28(b). Figure III-28(b) shows S_N versus I_{mass} data taken from four different data sets. Fitting a straight line through the origin to these points using statistical weighting (red line) yields a slope of 5.5×10^{-5}. Using the measured value for m_0 yields an Ar atomic mass of 0.085 zg, in agreement with the expected mass of 0.066 zg. We have therefore weighed the potentially unknown atomic species of Ar using the mass-calibrated nanotube, demonstrating the potential of using nanotubes to perform ultraminiaturized mass spectrometry on a chip.

III-7-4 Origin of the Noise

Before any mass loading, there are fluctuations in current shown both in Figure III-26 (a) and (b), the root-mean-square noise level we observe is ~ 1.4 pA with the lock-in time constant ~ 1 s. Based on the relations found in ref. [64] and the physical parameters of our devices, the noise is too large to be accounted for by thermomechanical or temperature fluctuation noise. We therefore attribute this background noise to environmental charge fluctuations, which would yield a charge noise of ~ 10^{-4} e/Hz$^{1/2}$, similar to that found in previous experiments on nanotube SETs (e.g., ref. [67]).

To characterize the performance of a single-electron transistor, we determine how accurately charge on the gate can be measured $\delta Q/e$. In order to calculate the charge fluctuations δQ, we start with the measurable current fluctuation,

$$\delta I = \left(\frac{dG}{dV_G} \tilde{V}_{sd} \right) \delta V_G^{DC} = \frac{dG}{dV_G} \tilde{V}_{sd} \frac{\delta Q}{C_G}. \qquad \text{(III-36)}$$

The voltage difference required to add an electron in nanotube is $e = \Delta V_G C_G$. Thus we can write down,

$$\frac{\delta Q}{C_G} = \frac{\delta Q}{C_G} \frac{\Delta V_G}{\Delta V_G} = \frac{\delta Q}{e} \Delta V_G. \qquad \text{(III-37)}$$

And substituting eq. (III-37) for eq. (III-36), we have

$$\delta I = \frac{dG}{dV_G} \frac{\delta Q}{e} \Delta V_G$$

then

$$\frac{\delta Q}{e} = \frac{\delta I}{\frac{dG}{dV_G} \Delta V_G}$$

where in this data set the current noise is $\delta I = 1.4\,\text{pA}/\sqrt{\text{Hz}}$, and estimate the $\frac{dG}{dV_G} \sim 300\,\mu\text{S}/\text{V}$, $\Delta V_G = 0.0625\,\text{V}$ from data in Figure III-23. $\delta Q \sim 10^{-4} \frac{e}{\sqrt{\text{Hz}}}$, which is similar to the value obtained from the SET at 60K in the ref. [67].

III-8 Summary

The atomic-scale mass resolution we observe here has significant scope for further improvement, for example, by using shorter nanotubes to reduce the nanotube mass, achieving better contacts, lowering the temperature to increase dG/dV_G, and maintaining the drive frequency near resonance using feedback to improve the dynamic range of mass sensitivity. Such further improvement may conceivably permit a resolution on the order of the proton mass ~1 yg, which could enable isotopic or chemical identification. Finally, for sufficiently short nanotubes, room temperature operation of the nanotubes as single-

electron transistors [67] may also yield highly sensitive detecting and weighing of adsorbates. Finally, we note that similar results came out independently from the Zettl group in Berkeley in 2008 [68].

Appendix

In this section, some preliminary experiments were not completed during my graduate study. A few initial results and observations will be discussed.

A-1 Argon Desorption at T ~ 20K

Carbon nanotube resonators provide an opportunity to study the interaction between adsorbates and nanotube cylindrical surface. We found that the estimated binding energy of argon on carbon nanotubes is less than on graphite at $T \sim 20$ K, this result might be attributed to the curved surface lowering the binding energy.

This experiment is performed at $T \sim 20$ K; we found that Argon desorbs readily at this temperature. In order to measure the desorption rate, argon gas is effused into the sample space, following which the nanotube is mass loaded. We then turn on the pump to break the equilibrium, then monitor the favored desorption process. We record both amplitude (R) and phase (θ) evolving over a time period.

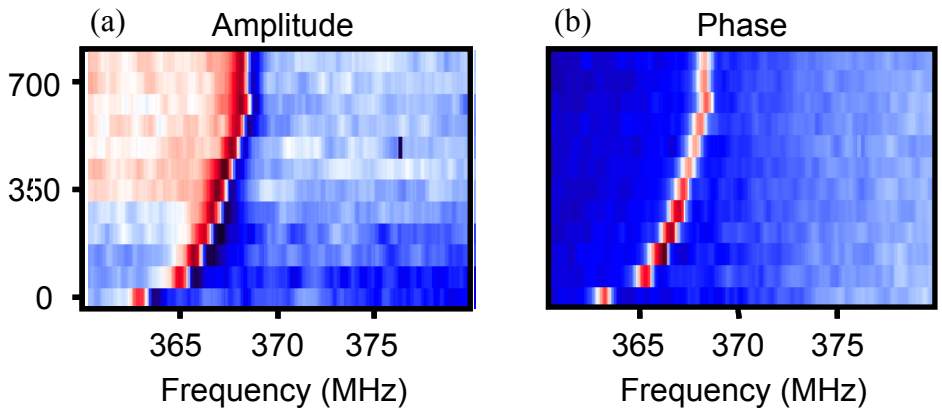

Figure III-29. Ar mass loading at $T \sim 20$ K. The resonant frequency up-shifted over a time period. (a) Shows the amplitude part of peak versus time. (b) Shows the phase part of the peak versus time

We can see two obvious curves from both signals, and then we carefully identified peaks in every line trace from phase signals, and plotted all the frequencies versus time in Figure III-30.

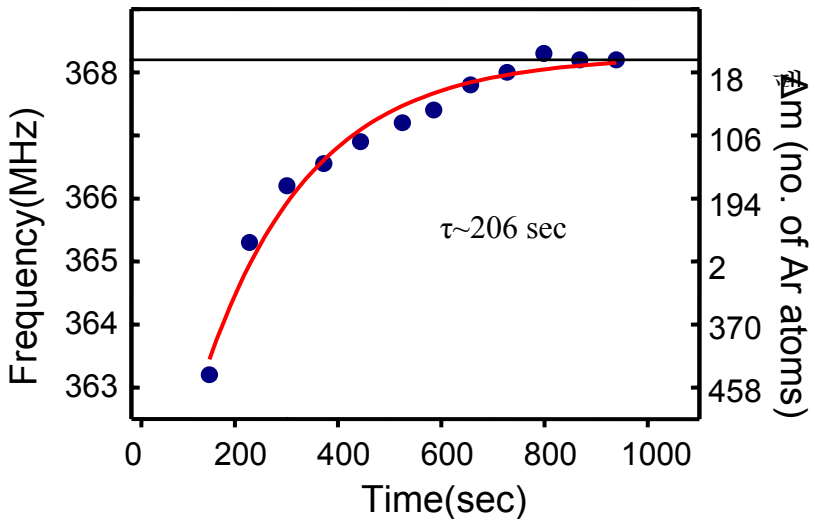

Figure III-30. The desorption curve with a fit parameter $\tau \sim 200$ sec. The left-frame scale is frequency and the right-frame scale is in the number of desorption argon atoms relative to steady state.

The associated microscopic thermal dynamical desorption rate $\frac{d[N]}{dt} = -k[N]$, where $[N]$ is the number of argon atoms that stick to the nanotubes and k is the rate constant. However, the rate equation can be rewritten in macroscopic phenomenological expression as

$$N = N_0\left[1 - \exp(-\frac{t}{\tau})\right], \qquad \text{(III.A-1)}$$

where τ is the macroscopic time constant and N_0 is the total amount of the adhered atoms having escaped from the surface. Also, the reaction rate coefficient k has a temperature dependence, which typically is given by the Arrhenius equation.

$$k = k(T) = A\exp(-\frac{E_a}{k_B T}) \qquad \text{(III.A-2)}$$

where E_a is an activation energy and $k_B T$ is the thermal energy. At temperature T the molecules have energies given by a Boltzmann distribution; one can expect the number of collisions with energy greater than E_a to be proportional to $\exp(-\frac{E_a}{k_B T})$. A is an attempt frequency factor. In the desorption case, E_a is equivalent to Δ, the binding energy, and A is equivalent to ω_A, the characteristic of the vibrational frequency of the bond holding adsorbates to surfaces, typically $\omega_A \sim 10^{-13} s^{-1}$.

For the total amount of adhered atoms N_0 to escape from the surface, we can write down the rate equation; to integrate this equation, we can find where τ is the macroscopic time constant $1/\tau = k(T) = \omega_A \exp(-E_a / k_B T)$. From the data, we found the fitting parameter τ ~206 sec, therefore, the estimated binding energy E_a ~ 60 meV, which is somewhat smaller than the previous binding energy obtained for argon on graphite ~ 1113K (95.9 meV) [69, 70]. This discrepancy might be attributable to nanotube curvature, and having only a wrapped single sheet, in contrast to the flat multilayer structure of graphite.

Carbon nanotube resonators are an important breakthrough in NEMS not only because they enable high sensitivity of force or mass sensing, but also because they provides a unique platform for exploring the surface properties from a nearly atomically perfect surface, such as the above case in which we studied the binding energy between inert gases and carbon nanotubes.

A-2 Nonlinearity and Duffing Oscillator

In all the previous sections we only considered the linear response of mechanical oscillators. However, when the drive becomes sufficiently large, a mechanical system can be driven into a nonlinear regime. Figure III-31 shows the nonlinear behavior of a

platinum nanowire resonator 43 nm in diameter and 1.3 μm in length [71]. The main panel shows the drastic change in shape via a strain hardening effect while the driving amplitude increases; the inset shows the development of hysteresis or jump phenomenon for a nonlinear oscillator. Our carbon nanotube resonator has shown similar results, the asymmetric lineshapes can be found in Figure III-24 (b) and Figure III-25.

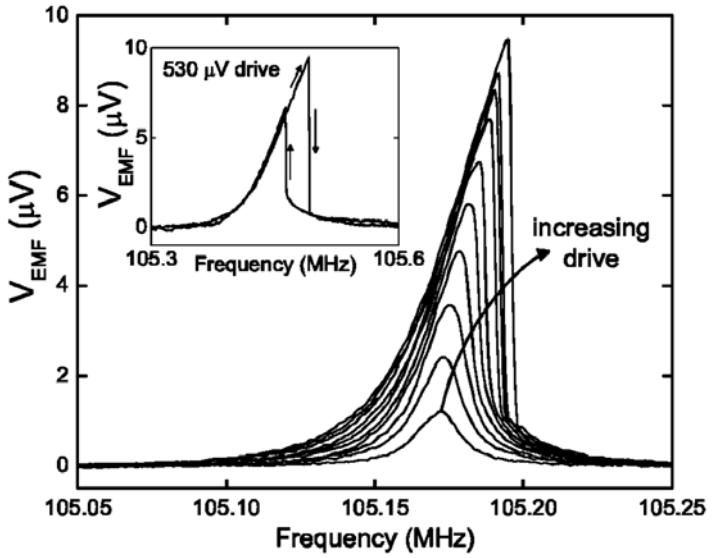

Figure III-31. The nonlinear oscillator made from Pt nanowire device [71].

Here we introduce the Duffing oscillator [72] to model this nonlinear system. Based on the formulation of the Duffing oscillator, the dominant nonlinearity in the restoring force is cubic which provides a mode–mode coupling, analogous to photon–photon coupling in nonlinear dielectrics, and drives instabilities. The equation is expressed as

$$\ddot{z}(t) + \frac{\omega_0}{Q}\dot{z}(t) + \omega_0^2 z(t) + \alpha z^3(t) = \frac{F_0}{m}\cos(\omega t) \qquad \text{(III-A.3)}$$

where $\omega_0 = \frac{4\pi^2}{L^2}\sqrt{\frac{EI}{3\mu S}(1+\frac{L^2 T_0}{4\pi^2 EI})}$ and $\alpha = \frac{E}{18\mu}\left(\frac{2\pi}{L}\right)^4$ [73], where S is the cross-sectional area, E is Young's modulus, μ is the density, I is the moment of inertia about the longitudinal axis of the beam, and Q is the mechanical quality factor as obtained in the linear regime.

Figure III-32 shows a typical response of a Duffing oscillator while the amplitude of vibration is increased. Usually the vibration amplitudes are small, the lineshape of the response is Lorentzian. However, above the critical amplitude a_c, the peak is pulled over toward higher frequencies due to the strain hardening effect. At this point, there are three solutions to III-A.3: two stable solutions and one unstable. The onset of nonlinearity due to elongation of the beam is expected at [72]

$$a_c = \omega_0 \frac{L}{\pi^2}\sqrt{\frac{\rho\sqrt{3}}{EQ}}\,.$$

Then the critical amplitude for the onset of nonlinearity of carbon nanotube is expressed

$$a_c = \frac{2}{\sqrt[4]{3}}\sqrt{\frac{1}{Q}\left(\frac{d^2}{4}+\frac{4T_0}{\pi^3 E}\frac{L^2}{d^2}\right)}\,.$$

The dynamic range is shown in Figure III-32.

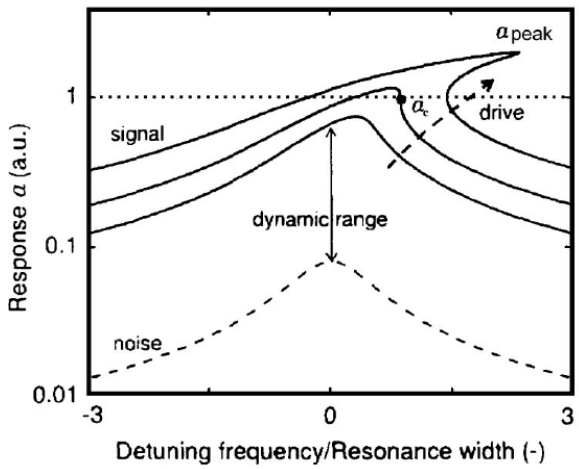

Figure III-32. Nonlinear resonator response. Resonator response versus driving frequency for increasing vibration amplitude[73]

A-3 Quality Factor

The quality factor is a dimensionless parameter which is the ratio of the time constant for decay of an oscillating physical system's amplitude to its oscillation period. Equivalently, it compares the frequency at which a system oscillates to the rate at which it dissipates its energy. A higher Q indicates a lower rate of energy dissipation relative to the oscillation frequency, so the oscillations decay more slowly.

Generally speaking, nanotube resonators in our system are easily driven into the nonlinear regime, which leads to the prediction that the dynamic range of a nanotube is small [73]. Even the AC drive amplitudes in our case are ~ 0.8 mV at ~ 6K; the resonator responds in an asymmetric shape shown in Figure III-24(b) and Figure III-25—it is hard to obtain the quality factor precisely from a non-Lorentzian lineshape. A coarse estimation of the quality factor in our nanotube resonator is ~200–2000. However, to study the cause of quality factor in the bottom-up fabrication system is hard to examine systematically, especially for our nanotube devices (which are made by random tube growth involving different type of nanotubes). Also the contact resistance varies from tube to tube and each fabrication.

Here we only address the possible dissipation mechanisms of a carbon nanotube resonator, we can rule out the cause of air damping in high-vacuum operation requirement, the clamping loss due to the small aspect ratio of beams, and the surface roughness.

Chapter IV

Carbon-Nanotube Linear-Bearing Nanoswitches[74]

IV-1 Abstract

We exploit the remarkable low-friction bearing capabilities of multiwalled carbon nanotubes (MWNTs) to realize nanoelectromechanical switches. Our switches consist of two open-ended MWNT segments separated by a nanometer-scale gap. Switching occurs through electrostatically actuated sliding of the inner nanotube shells to close the gap, producing a conducting ON state. For double-walled nanotubes in particular, a gate voltage can restore the insulating OFF state. Acting as a nonvolatile memory element capable of several switching cycles, our devices are straightforward to implement, self-aligned, and do not require complex fabrication or geometries, allowing for convenient scalability.

IV-2 Introduction

Microelectromechanical structures have produced a wealth of novel devices for sensing, actuation, and lab-on-a-chip applications. Making smaller nanomechanical systems promises faster and more compact versions of their larger counterparts, and it opens up the possibility of highly integrated nanoscale machines and logic circuits [75, 76]. However, challenges such as friction and precise control of device geometry remain important obstacles to the miniaturization of mechanical systems. Carbon nanotubes promise to address many of these challenges because of their intrinsic nanoscale dimensions, mechanical stiffness, structural perfection, and low intershell friction. Here we exploit the remarkable low-friction bearing capabilities [77-79] of multi- and double-walled carbon nanotubes (MWNTs and DWNTs) to realize a nanoelectromechanical switch that operates on an entirely different principle than previous efforts exploiting nanotube bending [80-84].

Our nanotube bearing devices are fabricated in high yield by using electric breakdown [19] to create gaps in a free-standing multiwall nanotube device producing an insulating OFF state. The devices are actuated with electrostatic forces and undergo linear bearing motion that telescopes the inner shells in the two MWNT or DWNT segments [85] so that they bridge the gap. This restores electrical contact and produces an ON state. Adhesion forces between the nanotube ends maintain the conductive state. For double-walled nanotube devices in particular, the insulating state is controllably restored using a gate voltage, enabling several repeated ON/OFF cycles. We thereby create three-terminal nonvolatile memory devices. We model the device behavior by considering the balance of electrostatic forces tending to close the device and restore the conductance and the retraction force from the intertube van der Waals forces. A fit of our model to data yields an estimate for the inner shell retraction force, which agrees with theoretical calculations as well as the results from atomic force microscopy (AFM) measurements [86]. Our results suggest that the intratube electrostatic repulsion makes a significant contribution to actuating the bearing motion. Finally, we estimate the switching speed of our devices, and find subnanosecond switching times for the typical nanoscale device geometries employed in our experiment, with considerable scope for further optimization of switching speed by using shorter and thinner nanotubes.

IV-3 Sample Fabrication

Samples are fabricated by one of two methods on top of heavily doped Si wafers capped by 300 nm or 1 μm of SiO_2. The first method is to evaporate Cr/Au contacts on arc-discharge synthesized MWNTs (dispersed in 1,2-dichloroethane) deposited on the substrate, and then use 10:1 buffered HF to etch the oxide and suspend the tubes, which is completely described in Section II-3. The second method is by forming the electrical leads, etching the oxide with 10:1 buffered HF, and then depositing MWNTs on top. A device schematic diagram with the nanotubes on top of the leads is shown in Figure IV-1.

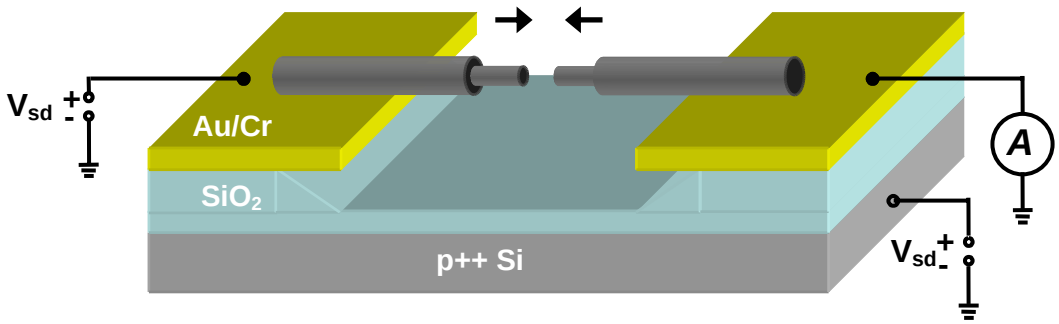

Figure IV-1. MWNT device geometry with attached electrodes and back gate

Once the device is fabricated, we perform the electrical breakdown on MWNT devices to create a gap. The details of the electrical breakdown mechanism are discussed in Chapter II.

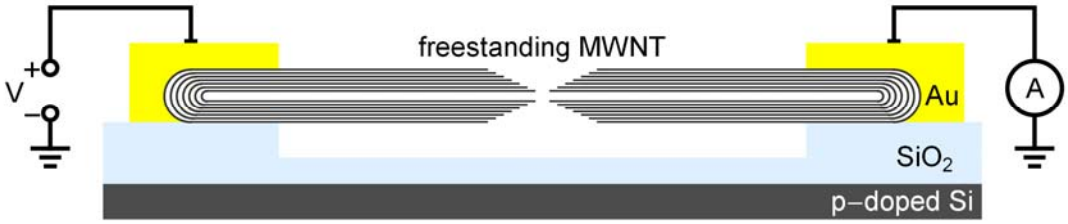

Figure IV-2. Schematic diagram of a MWNT device tailored by electrical breakdown

IV-4 Experimental Approach

IV-4-1 Initial OFF State Preparation

Our ~ 40 MWNT samples studied typically had an initial resistance ranging from ~10 kΩ to a few megaohms. A sufficiently high voltage, V, across the higher-resistance samples usually resulted in a rapid drop in resistance [87, 88]. This phenomenon enabled us to obtain low-resistance nanotube devices with resistance ~ 10−20 kΩ from nearly all contacted nanotubes. Figure IV-3 shows an I-V curve taken in an argon atmosphere from a device that was preannealed (device D1). The current rises approximately linearly until $V \approx 4.45$ V, at which point I drops to zero and V is quickly ramped down. This

observation is consistent with previous work in which heating and electrical stress result in the successive breakdown of the nanotube shells [19]. Indeed, SEM examination of devices after breakdown typically shows two segments with tapered ends, with each segment consisting of 10−30 shells, separated by a gap $d \approx 5-20$ nm. Figure IV-3 shows an SEM image from a representative device D2 with such a gap. After the gaps are formed, the devices are in an insulating OFF state, consistent with expected negligible tunnel current for electrode separation exceeding ~ 1−2 nm.

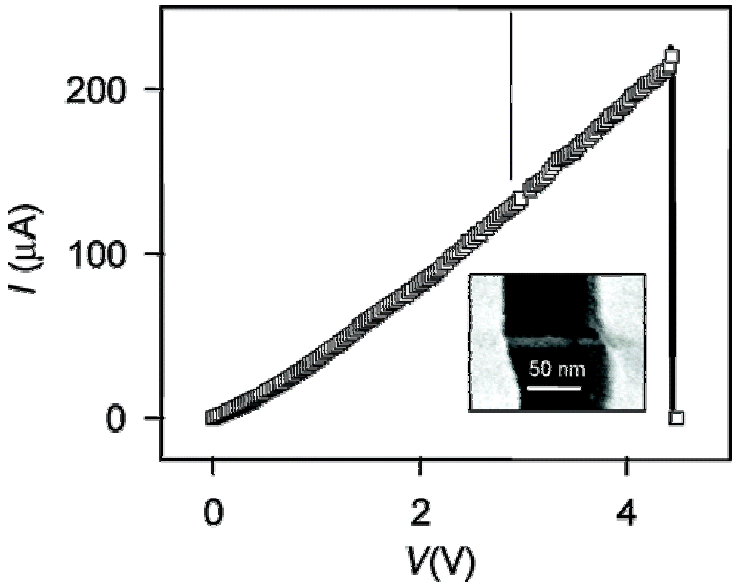

Figure IV-3. Relay device from free-standing MWNT. Main panel: *IV* characteristics of device D1 leading to electrical breakdown. Inset: MWNT D2 with a nanometer-size gap after electrical breakdown

IV-4-2 Switching to the ON State

On application of a higher bias (typically in the range of ~ 5−10 V) to D1 in the OFF state, at a voltage $V = 4.53$ V as shown in Figure IV-4, the current increases abruptly, leading to a conductive ON state (open squares). Once the bias was reduced to 0 V, the device remains latched in this ON state, showing a finite zero-bias resistance (filled squares). In the latched ON state, subsequent SEM imaging of the devices shows that the gap vanishes, indicating nanomechanical motion of the nanotube shells to physically rejoin the two nanotube segments and complete the electrical circuit. The Figure IV-4

lower-right inset shows this closure for device D2. Our devices thus act as an electrostatically actuated nanomechanical switch. Approximately 1/3 of MWNT devices switched to the ON state with $V \leq 10$ V.

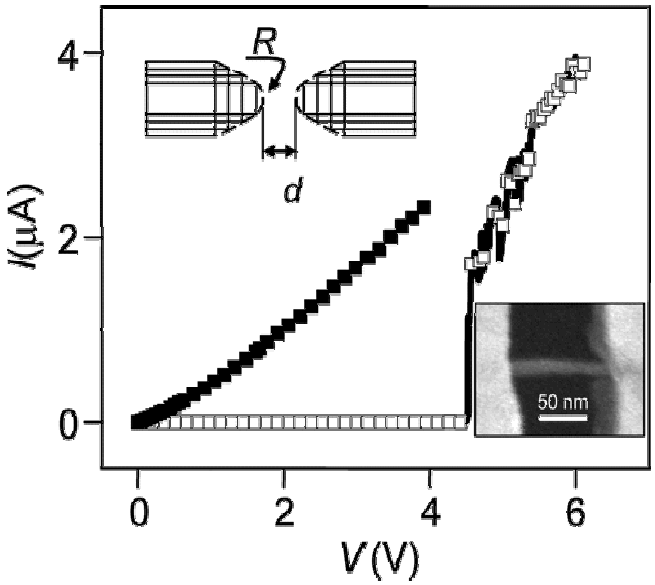

Figure IV-4. Relay device ON characteristics. Main panel: abrupt rise in conductance of device D1 on sweeping of voltage V_{sd} (open squares) and subsequent latching in the ON state (filled squares). Lower right inset: SEM image of D2 after latching shows that gap has closed. Upper right inset: schematic cup and cone model of the tube ends used for analysis.

IV-5 Analysis

Careful examination of the MWNT positions in a number of representative samples before and after joining showed that the outer shell remains pinned to the contact even when gaps as large as ~ 20 nm have been closed. Furthermore, SEM examination of our devices rarely shows any observable slack, consistent with the high mechanical stiffness of the ~ 10−20 nm diameter MWNTs. Thus, actuation is unlikely to occur in general by nanotube bending. Having ruled out these possibilities, we then consider telescoping of inner shells from their outer casing as the actuation mechanism [77]. We use the linear bearing model of Cumings and Zettl [77] to model the van der Waals force between shells within the MWNT. The bearing is expected to act as a constant-force spring, that

is, the force is independent of the extended length, with the expected retraction force $F_R = \alpha R$, with R the extended core radius and $\alpha \approx 1$ N/m a constant. To close the circuit, F_R must be overcome by the electrostatic force due to the applied voltage. To model the electrostatic force, we approximate the MWNT segments with a cone for the tapered part, and a spherical cap at the tip (Figure IV-4, upper-left inset) [89]. The geometric parameters for this model (cap radius R, gap d, cone-half-angle θ) are carefully extracted from the SEM images using a MATLAB image-processing program. Note that we calibrated the SEM radius measurements carefully by comparing SEM images to AFM images on the same nanotube for a selected subset of the nanotubes. The estimated radius measurement error is ±1 nm, as indicated in Figure IV-5.

The two main force contributions arise from electrostatic attraction between the segments and intrashell electrostatic repulsion within a segment. Both of these forces tend to slide one or more shells out to close the gap. It is most straightforward to estimate these for the case where the two segments are far apart ($d >> R$). In this case, the attractive force between segments (considered to be point charges for this evaluation) is $\pi\varepsilon_0 V^2 R^2 / (d+2R)^2$ while the repulsive force within a segment (modeled as force between two halves of a charged sphere) is $\pi\varepsilon_0 V^2$. The force balance gives

$$\alpha R = \pi\varepsilon_0 V^2 [\frac{R^2}{(d+2R)^2} + 1].$$

Plotting V^2 versus R for data points with $d/R >> 1$ should thus yield a straight line with a slope $\alpha/\pi\varepsilon_0$ where α ≈ 1 N/m, obtained from previous AFM measurements [86]. Scaling data points as d/R in Figure IV-5, indeed we find that data points with the largest d/R (corresponding to the bigger squares) lie closest to α = 1 N/m.

This demonstrates that for d/R in this range the dominant actuation force comes from the intratube repulsive forces rather than the intertube attractive forces. For data with $d \approx R$ (corresponding to the smaller squares) the data falls below the line, signifying a smaller voltage to overcome the van der Waals forces for a given R. Although accurate modeling

of the electrostatics for $d \approx R$ is challenging because of a lack of charge distribution information on individual shells, we expect that in this regime both the electrostatic intratube repulsion and intertube attraction are $\sim \pi\varepsilon_0 V^2$, leading to a smaller closing voltage than in the $d \gg R$ regime, in qualitative agreement with our observations.

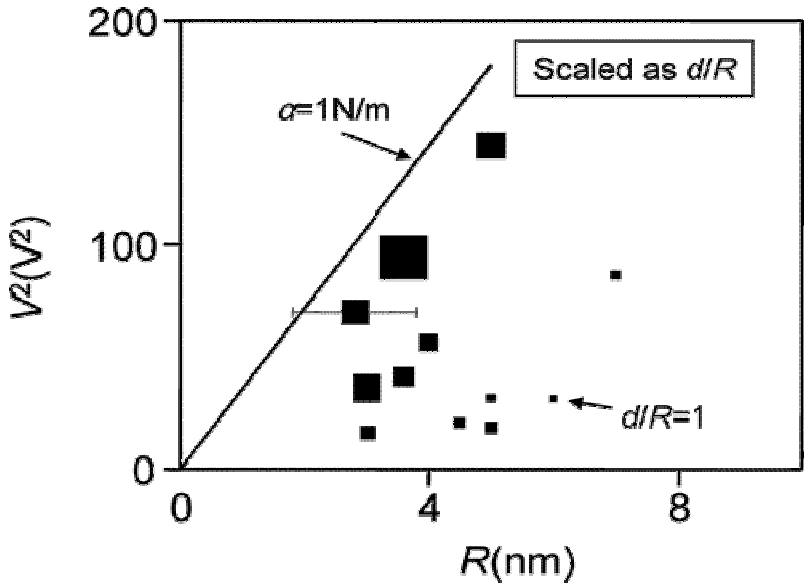

Figure IV-5. Plot of V^2 versus R. Data points' sizes are proportional to d/R. Plot shows that data matches the parameter-free model (as indicated by the force constant of 1 N/m) closely for large d/R, where it is expected to have the greatest validity. The plot also reveals that samples with nanotube segments close in ($R \approx d$) are actuated at lower V than those well separated ($d >> R$).

IV-6 DWNT Cycling Operation

The above procedure of electrical breakdown and closing of gap with bias voltage has been applied to DWNTs as well. DWNTs were obtained commercially from NanoLab, Inc., and had a typical diameter $D \approx 3-6$ nm. Using the p-doped silicon wafer as a back gate in these samples, we find that for high-enough gate voltage, devices switch back to the OFF state, thus enabling repeated ON−OFF cycles. Figure IV-6 shows the time-trace plot of DWNT device D3 (with a pre-breakdown resistance of 100 kΩ) for two cycles in Ar environment.

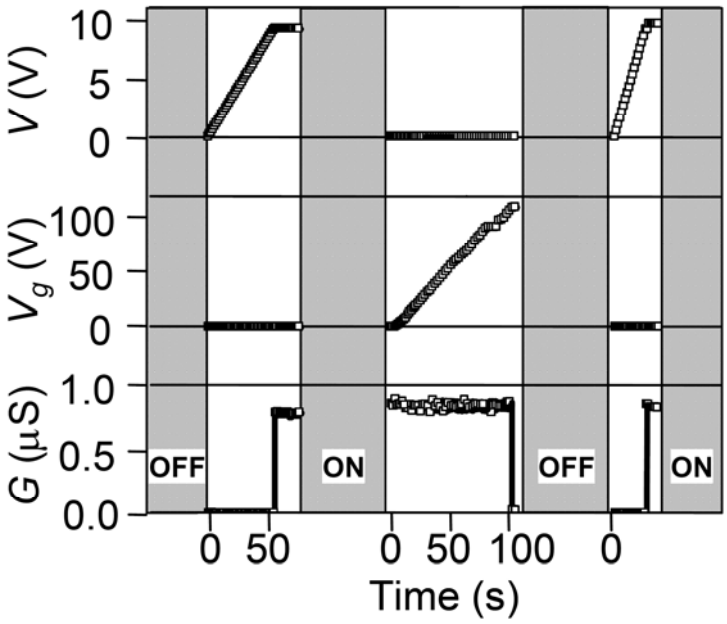

Figure IV-6 Three-terminal relay switching and operation. Plot shows the time trace of bias voltage (V), gate voltage (V_g), and conductance (G) for DWNT device D3 for two cycles. The device initially in the OFF state turns ON, OFF, and ON again, as seen in the plot of G. Transport data was obtained from D3 in series with a 1 MΩ protection resistor.

In the OFF state, on applying a bias voltage, the conductance increases abruptly at V_{sd} = 9 V leading to the ON state. With V_{sd} = 10 mV, at V_{gate} = 110 V the device snaps back to the zero conductance (OFF) state. On application of bias voltage, at V_{sd} = 9 V the device turns ON again. Nearly all of the 10 DWNT devices tested successfully switched back to the ON state after electrical breakdown and either became insulating or remained latched in the ON state within 3−4 switching cycles.

We consider the possible explanations for this reversible gate-switching. Previously, a gate voltage has been used to induce the same sign charge and create repulsive electrostatic forces between nanotubes in lateral contact, [90] thereby breaking the contact between two nanotubes. However, in our devices this mechanism is unlikely, because with the tapered geometry the electrostatic forces are unlikely to have any tensile component.

Another possibility is that the gate voltage places a bending stress on the nanotube that acts to break the connection. After setting the gate voltage back to zero, the nanotube segments elastically return to their original OFF state positions. Consider the conductor-to-plane capacitance C_{cp} between a cylindrical conductor of radius R and a conducting plane a distance h from the cylinder, as shown in Figure IV-7, where

$$C_{cp} = \frac{2\pi\varepsilon l}{\cosh^{-1}(h/R)} \approx \frac{2\pi\varepsilon l}{\ln(2h/R)}.$$

Thus we can obtain the electrostatic force (per unit length) on the nanotube due to V_g,

$$F_{el} = \frac{\pi\varepsilon V_g^2}{h[\ln(2h/R)]^2}.$$

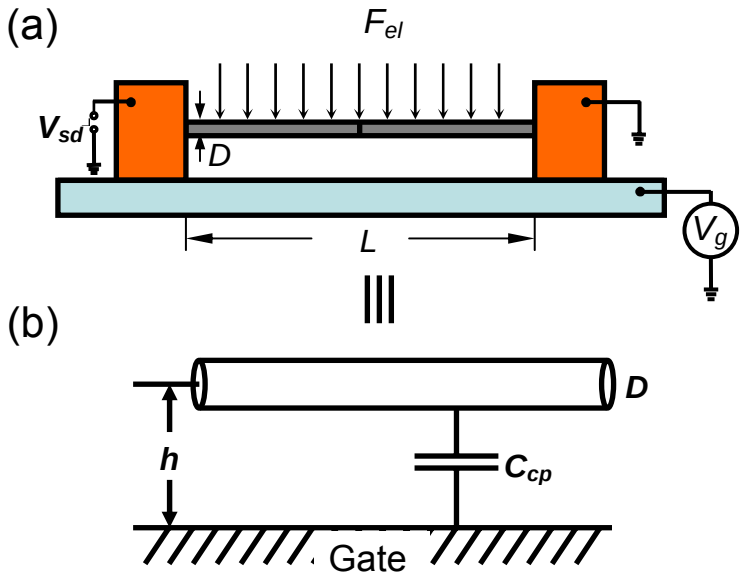

Figure IV-7. (a) Schematic diagram of device configuration with electrostatic force present. (b) Simplified diagram of (a), representing an infinite conducting wire a distance h above an infinite conducting plane

On the basis of elementary beam mechanics, the maximum bending stress corresponding to F_{el}, (occurring at the midpoint of the nanotube) is $\sigma = 4F_{el}L^2/3\pi D^3$.

To determine the bending stress, we can continue the derivation in Section III-6-4, which has considered a doubly clamped nanotube and the maximum displacement

$$u\left(\tfrac{L}{2}\right) = \frac{f L^4}{384 EI}.$$

From the relations of a bending element, the curvature $\frac{1}{\rho} = \frac{\partial^2 u}{\partial x^2} = \frac{M_0}{E I_x}$ and the bending stress $\sigma_x = M y / I_x$. (A reminder: M_0 is the external moment and M is internal, $M_0 = -M$.) We have $M_0 = (L^2 - 6Lx + 6x^2) EI_x f / 12$ with the maximum moment occurring at the center of the beam. Thus, $M_0\left(\tfrac{L}{2}\right) = -f L^2 / 24 = -M$ with the maximum stress occurring at the outmost surface, $y = D/2$, and since we know the area moment of inertia of the beam moment $I_x = \pi R^4 / 64$, we obtain

$$\sigma_x = \frac{4 f L^2}{3\pi D^3} = \frac{4 F_{el} L^2}{3\pi D^3}.$$

This is ~ 10^{11} Pa for V = 110 V and typical values of d, L, and h (D = 5 nm, L = 500 nm, h = 350 nm). We note that this force greatly exceeds the van der Waals forces between tube ends, which correspond to a binding stress of ~ 10^7 Pa, using the value for the interlayer adhesion in graphite. Further evidence for this mechanical switching action comes from the fact that we do not see gate-voltage switching with MWNTs, which have much larger diameters and greatly reduced bending stress.

Also, the gap-closing OFF−ON transition is not as stable as that seen in Figure IV-6, if the device is imaged in the SEM in the intermediate stage or even just exposed to the ambient atmosphere, indicating that the cleanliness of the tube ends is important for stable adhesion. This and the large-magnitude gate-induced bending stress suggest that the nanotube adhesion results from the formation of one or more covalent bonds between the atoms in the tube ends. However, further experiments are necessary to fully elucidate the adhesion mechanism: for example, high-temperature vacuum annealing of the device

post-breakdown, to close and cap the ends of the inner nanotube shells [91]. It is expected that the tube ends would then adhere with the smaller van der Waals bonds, and may permit, for example, the realization of microwave-frequency oscillators [92, 93] or charge shuttles.

We also note that the observed switching voltage can likely be reduced by optimization of the geometry such as using thinner nanotubes and decreasing the distance between the nanotube and the back gate. Using a core mass $m \approx 2 \times 10^{-19}$ kg corresponding to a nanotube of length 500 nm and core radius ~ 5 nm, an accelerating force ~ 5 nN, and a gap distance ~ 5 nm, we estimate using Newton's laws a switching speed ~ 400 ps, comparable to silicon-based transistor technology. This could be reduced substantially in principle by using shorter core lengths and smaller diameter to decrease m. The time to turn the device off should be much faster, comparable to the femto- or picosecond characteristic time scale for chemical bond breaking. These intrinsic nanomechanical time scales represent a lower bound for the switching speed approachable in practice only by carefully reducing the stray device capacitances and hence the characteristic RC charging times.

IV-7 Summary

In sum, we report nanoelectromechanical nonvolatile memory devices that operate by using multiwalled nanotubes as low-friction bearings. The devices are straightforward to fabricate in high yield and go through reversible ON−OFF conductance cycles with extremely high estimated switching speeds and high ON/OFF ratios. Aside from their use as nanoscale memory elements, their unique closing motion can be exploited: for example, as adjustable-gap probes to make electrical contact to other nanostructures that are attached using the flexible chemistry of the open nanotube ends.

Conclusions

In the thermal transport subject in Chapter II we discussed our experiments to probe the thermal properties of individual carbon nanotubes. We demonstrated heat conduction via ballistic phonon propagation in nanotubes, and determined the thermal conductance quantum, which is the ultimate limit to thermal conductance for a single phonon channel, at $T \sim 900$K. In addition, we suggested the breakdown mechanism of thermally activated C-C bond breaking coupled with the electrical stress of carrying 10^{12} A/m^2. In this project, we also demonstrated a current-driven self-heating technique to improve the conductance of nanotube devices dramatically.

In the electromechanical systems based on nanotubes discussed in chapter III, we provided the first reported carbon nanotube resonators at cryogenic temperatures, using their single-electron transistor properties to enable self-detection of the nanotube vibrations. We also observed nonlinear oscillator phenomena and provided a preliminary study of the binding energy between inert gases and carbon nanotube curved surface. The main achievement is the weighing of atomic inertial mass by carbon nanotube resonators; an atomic shot noise measurement was used to first calibrate the mass of the nanotube and then to determine those of unknown atoms/molecules.

In another electromechanical system of nanotubes in Chapter VI, we exploited the remarkable low-friction bearing capabilities of MWNTs to realize nanoelectromechanical switches. Our switches consisted of two open-ended MWNT segments separated by a nanometer-scale gap. Switching occurs through electrostatically actuated sliding of the inner nanotube shells to close the gap, producing a conducting ON state; for double-walled nanotubes in particular, a gate voltage can restore the insulating OFF state. These devices thus act as nonvolatile, switchable memory elements, with the added advantage that they are straightforward to implement, self-aligned, and do not require complex fabrication or geometries, allowing for convenient scalability.

Bibliography

1. Tans, S.J., et al., Individual single-wall carbon nanotubes as quantum wires. Nature, 1997. 386(6624): 474
2. Bockrath, M., et al., Luttinger-liquid behaviour in carbon nanotubes. Nature, 1999. 397(6720): 598
3. Deshpande, V.V. and M. Bockrath, The one-dimensional Wigner crystal in carbon nanotubes. Nature Physics, 2008. 4(4):314
4. R. Saito, G.D., M. S. Dresselhaus, Physical Properties of Carbon Nanotubes. 1st ed. World Scientific Publishing Company, 1998
5. Gulseren, O., T. Yildirim, and S. Ciraci, Systematic ab initio study of curvature effects in carbon nanotubes. Physical Review B, 2002. 65(15): 153405
6. Blase, X., et al., Hybridization effects and metallicity in small radius carbon nanotubes. Physical Review Letters, 1994. 72(12): 1878
7. Deshpande, V.V., et al., Mott Insulating State in Ultraclean Carbon Nanotubes. Science, 2009. 323(5910): 106
8. Liang, W.J., et al., Fabry-Perot interference in a nanotube electron waveguide. Nature, 2001. 411(6838): 665
9. Chiu, H.Y., et al., Ballistic phonon thermal transport in multiwalled carbon nanotubes. Physical Review Letters, 2005. 95(22): 226101
10. Pendry, J.B., Quantum Limits to the Flow of Information and Entropy. J. Phys. A, 1983. 16(10): 2161
11. Maynard, R. and E. Akkermans, Thermal Conductance and Giant Fluctuations in One-Dimensional Disordered-Systems. Physical Review B, 1985. 32(8): 5440
12. Schwab, K., et al., Measurement of the quantum of thermal conductance. Nature, 2000. 404(6781): 974
13. Hone, J., et al., Thermal conductivity of single-walled carbon nanotubes. Physical Review B, 1999. 59(4): R2514
14. Hone, J., et al., Quantized phonon spectrum of single-wall carbon nanotubes. Science, 2000. 289(5485): 1730

15. Llaguno, M.C., et al., Observation of thermopower oscillations in the Coulomb blockade regime in a semiconducting carbon nanotube. Nano Letters, 2004. 4(1): 45
16. Small, J.P., K.M. Perez, and P. Kim, Modulation of thermoelectric power of individual carbon nanotubes. Physical Review Letters, 2003. 91(25): 256801
17. Kim, P., et al., Thermal transport measurements of individual multiwalled nanotubes. Physical Review Letters, 2001. 87(21): 215502
18. Brown, E., et al., Ballistic thermal and electrical conductance measurements on individual multiwall carbon nanotubes. Applied Physical Letters, 2005. 87(2): 023107
19. Collins, P.G., et al., Current saturation and electrical breakdown in multiwalled carbon nanotubes. Physical Review Letters, 2001. 86(14): 3128
20. Bourlon, B., et al., Geometrical dependence of high-bias current in multiwalled carbon nanotubes. Physical Review Letters, 2004. 92(2): 026804
21. Yamamoto, T., S. Watanabe, and K. Watanabe, Universal features of quantized thermal conductance of carbon nanotubes. Physical Review Letters, 2004. 92(7): 075502
22. Whittaker, J.D., et al., Measurement of the adhesion force between carbon nanotubes and a silicon dioxide substrate. Nano Letters, 2006. 6(5): 953
23. Hertel, T., R. Martel, and P. Avouris, Manipulation of individual carbon nanotubes and their interaction with surfaces. Journal of Physical Chemistry B, 1998. 102(6): 910
24. Yao, Z., C.L. Kane, and C. Dekker, High-field electrical transport in single-wall carbon nanotubes. Physical Review Letters, 2000. 84(13): 2941
25. Huang, J.Y., et al., Atomic-scale imaging of wall-by-wall breakdown and concurrent transport measurements in multiwall carbon nanotubes. Physical Review Letters, 2005. 94(23): 236802
26. Cumings, J., P.G. Collins, and A. Zettl, Peeling and sharpening multiwall nanotubes. Nature, 2000. 406(6796): 586

27. Frank, S., et al., Carbon nanotube quantum resistors. Science, 1998. 280(5370): 1744
28. Park, J.Y., et al., Electron-phonon scattering in metallic single-walled carbon nanotubes. Nano Letters, 2004. 4(3): 517
29. Cahill, D.G., et al., Nanoscale thermal transport. Journal of Applied Physics, 2003. 93(2): 793
30. Schwab, K., et al., Measurement of the quantum of thermal conductance. Nature, 2000. 404(6781): 974
31. Rego, L.G.C. and G. Kirczenow, Quantized thermal conductance of dielectric quantum wires. Physical Review Letters, 1998. 81(1): 232
32. Benedict, L.X., S.G. Louie, and M.L. Cohen, Heat capacity of carbon nanotubes. Solid State Communications, 1996. 100(3): 177
33. Dresselhaus, M.S., G. Dresselhaus, and P.C. Eklund, Science of Fullerenes and Carbon Nanotubes. New York: Academic Press,1996
34. Kaxiras, E. and K.C. Pandey, Energetics of defects and diffusion mechanisms in graphite. Physical Review Letters, 1988. 61(23): 2693
35. Venema, L.C., et al., Length control of individual carbon nanotubes by nanostructuring with a scanning tunneling microscope. Applied Physics Letters, 1997. 71(18): 2629
36. Rubio, A., et al., A mechanism for cutting carbon nanotubes with a scanning tunneling microscope. European Physical Journal B, 2000. 17(2): 301
37. Chiu, H.Y., et al., Atomic-Scale mass sensing using carbon nanotube resonators. Nano Letters, 2008. 8(12): 4342
38. Yang, Y.T., et al., Zeptogram-scale nanomechanical mass sensing. Nano Letters, 2006. 6(4): 583
39. Schwab, K.C. and M.L. Roukes, Putting mechanics into quantum mechanics. Physics Today, 2005. 58(7): 36
40. Lamoreaux, S.K., Demonstration of the casimir force in the 0.6 to 6 μm range. Physical Review Letters, 1997. 78(1): 5

41. Hertel, T., R.E. Walkup, and P. Avouris, Deformation of carbon nanotubes by surface van der Waals forces. Physical Review B, 1998. 58: 13870

42. Kong, J., et al., Synthesis of individual single-walled carbon nanotubes on patterned silicon wafers. Nature, 1998. 395: 878

43. Ago, H., et al., Synthesis of horizontally-aligned single-walled carbon nanotubes with controllable density on sapphire surface and polarized Raman spectroscopy. Chemical Physics Letters, 2006. 421(4-6): 399

44. Jarillo-Herrero, P., et al., Orbital Kondo effect in carbon nanotubes. Nature, 2005. 434(7032): 484

45. Brintlinger, T., et al., Rapid imaging of nanotubes on insulating substrates. Applied Physics Letters, 2002. 81(13): 2454

46. Antognozzi, M., A. Sentimenti, and U. Valdre, Fabrication of nano-tips by carbon contamination in a scanning electron microscope for use in scanning probe microscopy and field emission. Microscopy Microanalysis Microstructures, 1997. 8(6): 355

47. Mann, D., et al., Ballistic transport in metallic nanotubes with reliable Pd ohmic contacts. Nano Letters, 2003. 3(11): 1541

48. Ustunel, H., D. Roundy, and T.A. Arias, Modeling a suspended nanotube oscillator. Nano Letters, 2005. 5(3): 523

49. Sazonova, V., et al., A tunable carbon nanotube electromechanical oscillator. Nature, 2004. 431(7006): 284

50. Witkamp, B., M. Poot, and H.S.J. van der Zant, Bending-mode vibration of a suspended nanotube resonator. Nano Letters, 2006. 6(12): 2904

51. Lassagne, B., et al., Ultrasensitive mass sensing with a nanotube electromechanical resonator. Nano Letters, 2008. 8(11): 3735

52. Sapmaz, S., et al., Carbon nanotubes as nanoelectromechanical systems. Physical Review B, 2003. 67(23): 235414

53. Sazonova, V., A Tunable Carbon Nanotube Resonator. Doctoral thesis, Cornell University, 2006

54. Ekin, J., Experimental Techniques for Low Temperature Measurements: Cryostat Design, Material Properties and Superconductor Critical-Current Testing. Oxford University Press, 2006
55. Dekker, C., Carbon nanotubes as molecular quantum wires. Physics Today, 1999. 52(5): 22
56. P., K.L., et al., Electron Transport in Quantum Dots. NATO ASI Conf. Proc. 1997
57. Knobel, R.G. and A.N. Cleland, Nanometre-scale displacement sensing using a single electron transistor. Nature, 2003. 424(6946): 291
58. Garcia-Sanchez, D., et al., Mechanical detection of carbon nanotube resonator vibrations. Physical Review Letters, 2007. 99(8): 085501
59. Postma, H.W.C., et al., Dynamic range of nanotube- and nanowire-based electromechanical systems. Applied Physics Letters, 2005. 86(22): 223105
60. Rayleigh, J.W.S., The Theory of Sound. 2nd ed. Vol. 1. Dover Publications, 1976
61. Bolton, K. and A. Rosen, Computational studies of gas-carbon nanotube collision dynamics. Physical Chemistry Chemical Physics, 2002. 4(18): 4481
62. Romero, H.E., et al., Atom collision-induced resistivity of carbon nanotubes. Science, 2005. 307(5706): 89
63. Kuznetsova, A., et al., Physical adsorption of xenon in open single walled carbon nanotubes: Observation of a quasi-one-dimensional confined Xe phase. Journal of Chemical Physics, 2000. 112(21): 9590
64. Ekinci, K.L., Y.T. Yang, and M.L. Roukes, Ultimate limits to inertial mass sensing based upon nanoelectromechanical systems. Journal of Applied Physics, 2004. 95(5): 2682
65. Cleland, A.N. and M.L. Roukes, Noise Processes in Nanomechanical Resonators. Journal of Applied Physics, 2002. 92(5): 2758
66. Yong, Y.K. and J.R. Vig, Resonator Surface Contamination - a Cause of Frequency Fluctuations. IEEE Transactions on Ultrasonics Ferroelectrics and Frequency Control, 1989. 36(4): 452
67. Postma, H.W.C., et al., Carbon nanotube single-electron transistors at room temperature. Science, 2001. 293(5527): 76

68. Jensen, K., K. Kim, and A. Zettl, An atomic-resolution nanomechanical mass sensor. Nature Nanotechnology, 2008. 3(9): 533

69. Rybolt, T.R. and R.A. Pierotti, Rare gas-graphite interaction potentials. Journal of Chemical Physics, 1979. 70(9): 4413

70. Steele, W.A., The interaction of rare gas atoms with graphitized carbon black. Journal of Physical Chemistry, 1978. 82(7): 817

71. Husain, A., et al., Nanowire-based very-high-frequency electromechanical resonator. Applied Physics Letters, 2003. 83(6): 1240

72. Ali H. Nayfeh, D.T.M., Nonlinear Oscillations. Wiley, 1979

73. Postma, H.W.C., et al., Dynamic range of nanotube- and nanowire-based electromechanical systems. Applied Physics Letters, 2005. 86(22). 223105

74. Deshpande, V.V., et al., Carbon nanotube linear bearing nanoswitches. Nano Letters, 2006. 6(6): 1092

75. Roukes, M., Nanoelectromechanical systems face the future. Physics World, 2001. 14(2): 25

76. Rueckes, T., et al., Carbon nanotube-based nonvolatile random access memory for molecular computing. Science, 2000. 289(5476): 94

77. Cumings, J. and A. Zettl, Low-friction nanoscale linear bearing realized from multiwall carbon nanotubes. Science, 2000. 289(5479): 602

78. Fennimore, A.M., et al., Rotational actuators based on carbon nanotubes. Nature, 2003. 424(6947): 408

79. Bourlon, B., et al., Carbon nanotube based bearing for rotational motions. Nano Letters, 2004. 4(4): 709

80. Kinaret, J.M., T. Nord, and S. Viefers, A carbon-nanotube-based nanorelay. Applied Physics Letters, 2003. 82(8): 1287

81. Cha, S.N., et al., Fabrication of a nanoelectromechanical switch using a suspended carbon nanotube. Applied Physics Letters, 2005. 86(8): 083105

82. Jang, J.E., et al., Nanoelectromechanical switches with vertically aligned carbon nanotubes. Applied Physics Letters, 2005. 87(16): 163114

83. Dujardin, E., et al., Self-assembled switches based on electroactuated multiwalled nanotubes. Applied Physics Letters, 2005. 87(19): 193107

84. Lee, S.W., et al., A three-terminal carbon nanorelay. Nano Letters, 2004. 4(10): 2027

85. Forro, L., Nanotechnology–Beyond Gedanken experiments. Science, 2000. 289(5479): 560

86. Akita, S. and Y. Nakayama, Interlayer sliding force of individual multiwall carbon nanotubes. Japanese Journal of Applied Physics, 2003. 42(7B): 4830

87. Chiu, H.Y., et al., Ballistic Phonon Thermal Transport in Multiwalled Carbon Nanotubes. Physical Review Letters, 2005. 95: 226101

88. Huang, J.Y., et al., Atomic-scale imaging of wall-by-wall breakdown and concurrent transport measurements in multiwall carbon nanotubes. Physical Review Letters, 2005. 94(23): 236802

89. Hudlet, S., et al., Evaluation of the capacitive force between an atomic force microscopy tip and a metallic surface. The European Physical Journal B, 1998. 2(1): 5

90. Kim, P. and C.M. Lieber, Nanotube nanotweezers. Science, 1999. 286: 2148

91. Geng, H.Z., et al., Opening and closing of single-wall carbon nanotubes. Chemical Physics Letters, 2004. 399(1-3): 109

92. Zheng, Q.S. and Q. Jiang, Multiwalled carbon nanotubes as gigahertz oscillators. Physical Review Letters, 2002. 88(4): 045503.

93. Legoas, S.B., et al., Molecular-dynamics simulations of carbon nanotubes as gigahertz oscillators. Physical Review Letters, 2003. 90(5): 055504